ABSTRACT

Title of dissertation:	PLANAR ELECTROMAGNETIC BANDGAP STRUCTURE FOR WIDEBAND SWITCHING NOISE MITIGATION IN HIGH SPEED CIRCUITS
	Jie Qin, Doctor of Philosophy, 2006
Dissertation directed by:	Professor Omar M. Ramahi Department of Electrical and Computer Engineering University of Waterloo, Canada Professor Victor Granatstein Department of Electrical and Computer Engineering University of Maryland, College Park

With the increasing demand for modern digital circuit with fast edge rates and high clock frequencies, simultaneous switching noise has become a major concern. When many active devices switch at the same time, the switching noise generated can cause fluctuations or disturbances in the power distribution system (PDS) which, in turn, leads to a degradation of the signal integrity (SI). When this noise propagates along the waveguide like multi-layer printed circuit boards (PCBs), it will be coupled with other vias to affect the functionality of other circuits.

This research work is focus on how to mitigate the noise propagation. The problem of SSN has been discussed intensively over the last decade and different approaches have been taken to mitigate it. Typical used methods include the

placement of decoupling capacitors, the use of embedded capacitance, via stitching, or a combination of any of these techniques. The most common drawback of previous methods is the limited frequency bandwidth that they can cover (usually below 1GHz). In this study, I proposed using novel planar electromagnetic bandgap (EBG) structure for noise mitigation. I developed novel designs of meander lines EBG structure in combination of super cell concept, and wideband noise mitigation from 250MHz to 12GHz is achieved.

Leakage radiation effects from this EBG-patterned surface are also investigated numerically and experimentally. By characterize the radiation effects, especially its near field property, this EBG structures is shown to be a very effective tool for suppressing electromagnetic interference (EMI) from PCBs. A novel concept of using EBG structures as an enhancing shielding technology is introduced.

Finally, the effect of these EBG structures on signal integrity (SI) of multi-layer PCBs is characterized using eye diagram. Some potential methods to improve the signal quality of power plane are introduced. Also the potential effect of EBG structure itself on the local switching noise generation is investigated.

In summary, this thesis developed a new effective design of planar EBG structure to mitigate noise propagation in power distributed system (PDS). By carefully characterize its EMI and SI performance, we show this planar EBG structure has a potential to be used in next generation IC packaging technology.

PLANAR ELECTROMAGNETIC BANDGAP STRUCTURE FOR WIDEBAND SWITCHING NOISE MITIGATION IN HIGH SPEED CIRCUITS

By

Jie Qin

Dissertation submitted to the Faculty of the Graduate School of the
University of Maryland, College Park, in partial fulfillment
of the requirements for the degree of
Doctor of Philosophy
2006

Advisory Committee:

Professor Victor Granatstein, Chair
Professor Omar M. Ramahi, Co-Chair
Professor Peter Sandborn
Professor Thomas M. Antonsen
Professor John Melngailis

Dedication

"To my dear Mom and Dad, my lovely wife, and my little angel: Annie

for your love and encouragement through all these years …"

ACKNOWLEDGEMENTS

I owe my gratitude to all the people who have made this thesis possible and because of whom my graduate experience has been and will always be invaluable to my whole life.

My first acknowledgement goes to my previous advisor, Professor Omar Ramahi, who opened the door for me to this challenging and extremely interesting project. I could not make so much progress in so little time without his sharp insight and invaluable guidance. It is indeed a great pleasure to work with him and learn from him. Unfortunately he left this school during the midway of my work. While he still gave me his endless support. I would like to express my sincere gratitude to him.

I am also very grateful to my current advisor, Professor Victor Granatstein, who gave me great help during my later phase of my Ph.D. study. His unwavering support and constant encouragement made me continue to finish this research. He is one of the most gracious and knowledgeable professors I ever met in my life.

I would like to thank Professor Thomas M. Antonsen, Professor Peter Sandborn, and Professor John Melngailis for their time and support to serve on my dissertation committee.

I would like to acknowledge Dr. Dan Balon, Maria Hoo, Zhen Wu, Jay Pyle, Dr. John Rogers, Shyam Mehrotra, and Jay Renner, the staff at ECE and ME department at the University of Maryland for their help during my study. A special “thank you” goes to Dr. Dan Balon, who gave me his earnest support during my trouble time.

I want to thank all my fellows at ECE Department of University of Maryland. Specifically, I would like to thank Kai Tian, Lin Li, He Huang, Todd Firestone, Gang Bai, Mohammad Kermani, Jake Yang, just name a few, for being there for me during the time that I was most in need. I thank many Chinese friends that I made at UMCP. They help me enjoying my life here.

Finally, I am deeply indebted to my whole family for supporting me every step along this long journey. I especially thank my parents in law, Huizhen Li and Wanfa Liu, even they are over 60s and not in good health for themselves, while they came here to take care of my newborn daughter and put great efforts to make my research as smooth as possible. I thank my sister, Ting Qin, and sister's husband, Yanpin Tan, for taking care of my parents and for encouraging me to pursue this doctorate degree. Thank my daughter, Annie, who grows together every step with my thesis. She is the source of my joy. She makes me to be always refreshed no matter how I feel depressed and exhausted during my work. Her smile makes my life so much nicer. To the most important person in my life, my wife Yiting Liu, thank you for your love. We have been walking through some of the hardest time together. Your love, encouragement and care make this dissertation as much yours as it is mine. Without you, I could not have gone through all the difficulties and completed my study. The last but not the least, I want to express my deepest gratitude to my mother, Junlin Niu, and my father, Xiongfu Qin, thank you for providing me with all of your love and support, without which I never would have achieved so much. You have breathlessly awaited this dissertation, and you deserve every single credit of any of my achievements. Thank you, Mom and Dad!

Table of Contents

Dedication II

ACKNOWLEDGEMENTS III

Table of Contents V

List of Figures VIII

CHAPTER 1 Introduction, Background, and Objective of the Dissertation 1

1.1 Motivation of the Work 1

1.2 Dissertation Organization 5

1.3 Simultaneous Switching Noise 6

1.4 Electromagnetic Bandgap Structure 9

1.5 Parallel Plate Waveguide 13

CHAPTER 2 Planar EBG Structure Design and Wideband Mitigation of Simultaneous Switching Noise 18

2.1 Simultaneous Switching Noise Frequency Limitation 18

2.1.1 Introduction 18

2.1.2 Upper frequency edge of SSN 19

2.2 Characterization of EBG Structures 25

2.2.1 Introduction 25

2.2.2 Full wave complete space analysis 25

2.2.3 Symmetry boundary method 28

2.3 Planar EBG Structures 31

2.3.1 Structure design 31

2.3.2 Fabrication 33

2.3.3 Simulation and experimental result 35

2.3.4 Super cell EBG structure 37

2.3.5 Miniaturization of EBG structure 42

2.3.6 Summary 44

CHAPTER 3 Compact Circuit Modeling of
Electromagnetic Bandgap Structures 45

3.1 Introduction 45
3.2 Lumped Element Model Development 47
3.2.1 Model form definition 47
3.2.2 Lumped parameters extraction 49
3.2.3 Meander line EBG 2D model 54
3.2.4 Simulation and discussion of results 56
3.2.5 Super cell EBG model 59
3.3 Bloch-Floquet Theorem 62
3.4 Dispersion Diagram 65
3.4.1 Meander-L EBG structure 65
3.4.2 Super cell EBG structure 68

CHAPTER 4 Leakage Radiation and EMI Reduction
of Electromagnetic Bandgap Structures 73

4.1 Introduction 73
4.2 Leakage Radiation through EBG Patterned PCBs 74
4.3 Near Field Characterization 79
4.4 EMI Shielding Using EBG Patterned Surface 85
4.5 Antenna Normalization 89
4.6 Summary 92

CHAPTER 5 Signal Integrity of Power Plane with
Electromagnetic Bandgap Structures 93

5.1 Introduction 93
5.2 Eye Diagram Characterization 94
5.3 Eye Diagram of Power Plane with EBG Structures 97
5.3.1 Test vehicle description 97

5.3.2 Eye diagram of meander-L EBG structure.. 99
5.3.3 Differential pair scheme.. 104
5.3.4 5-layer structure scheme 107
5.3.5 Eye diagram of super-cell EBG structure 109
5.4 Voltage Drop of Power Plane with EBG Structure 111
5.4.1 Circuit schematics...111
5.4.2 Simulation results and discussion 113

CHAPTER 6 Conclusions and Future Work 117
6.1 Conclusions.. 117
6.2 Future Work 119

Bibliography 121

List of Figures

Figure 1-1: General configuration of a simultaneous switching noise environment for a multilayer board. 9

Figure 1-2: Illustration of 3D electromagnetic bandgap structure with vertical post (a) top view (b) side view 11

Figure 1-3: Boundary conditions for PMC and PEC 11

Figure 1-4: Three layer EBG structure with inductance enhanced vias (a) single-loop inductive element (b) cross section of structure [15] 12

Figure 1-5: Planar EBG structure (a) top view (b) side view [20] 13

Figure 1-6: Diagram for an ideal parallel plate waveguide as a model for the power planes of a PCB 17

Figure 2- 1: Periodic trapezoidal pulse train representing (a) the clock or data signals of digital system. (b) SSN waveform due to the charging/discharging current 20

Figure 2- 2: Typical CMOS output driver switching characteristics 21

Figure 2- 3: Bounds on magnitude spectrum of a trapezoidal pulse train 22

Figure 2- 4: Effect of duty cycle on the spectral bounds of trapezoidal pulse train ... 24

Figure 2- 5: EBG structure with different spacing (3cm, 10cm) from radiation boundary (a) simulation structure geometry (b) S-parameter simulation result 27

Figure 2- 6: Diagram showing the symmetric boundary for perfect E and H 28

Figure 2- 7: Diagram representing the symmetric boundary model used to derive the bandgap of EBG structure 30

Figure 2- 8: Comparison of S parameter simulation using two different methods: one is full wave complete space method (solid line); the other is symmetry boundary method (dotted line). 30

Figure 2- 9: (a) Planar EBG structure with Meander-L bridge showing the location of the ports used for S21 parameter measurements. (b) Unit cell showing the Meander Line bridge and dimensions. (c) Qualitative equivalent circuit model for unit cell of the Meander-L EBG structure 32

Figure 2- 10: LPKF ProtoMat C100/HF circuit plotter used for our prototype.......... 33

Figure 2- 11: Photo of top view of meander line EBG structure, two soldering points showing the two test ports.. 34

Figure 2- 12: Numerical simulation and measurement result for magnitude of S_{21} between two ports across EBG patches having Meander line bridge (Meander-L). Comparison is made with a two layer power plane (Reference) 36

Figure 2- 13: (a) Schematic top view of a super cell with dimensions....................... 38

Figure 2- 14: Numerical simulation and measurement of the magnitude of S_{21} between for the novel structure proposed in this work (super cell) and for the two layer power plane (reference.) 39

Figure 2- 15: Comparison between the lower frequency edge of the bandgap for the Meander Line and Super-cell structures. 40

Figure 2- 16: Comparison of magnitude of S21 between 60mm Meander-L patch (solid line) and 30mm super cell patch (dotted line) 41

Figure 2- 17: Numerical simulation of the magnitude of S_{21} for high K thin film EBG structures (a) comparison between solid reference and EBG patterned plane (b)

comparison between different thickness: 1.54mm (dot line), 0.4mm (dash line) and 20um (solid line) 43

Figure 3- 1: Unit cell of meander-L EBG structure (a) top view (b) side view 47

Figure 3- 2: (a) Equivalent circuit model for the unit cell of Meander-L EBG structure, where top part representing the metal patch effect, bottom part representing bridge effect (b) Circuit model for the cascaded periodic Meander-L EBG structure 49

Figure 3- 3: Flow diagram of lumped elements extraction 51

Figure 3- 5: Modeled vs. simulated S-parameters of EBG structure 53

Figure 3- 6: equivalent circuit model of meander-L EBG unit cell for two-dimensional wave propagation with ports 1-5 indicated 54

Figure 3- 7: Illustration of meander-L EBG structure based on cascading of several unit cell models 55

Figure 3- 8: Modeled vs. simulated S-parameters of 2D EBG structure 55

Figure 3- 9: Dependence of the bandgap center frequency on the product of bridge inductance L_b and gap capacitance C_g. 57

Figure 3- 10: Dependence of the bandwidth on the ratio of bridge parameters L_b/C_g.58

Figure 3- 11: Dependence of the upper corner frequency of stopband on the product of patch parameters L_pC_p. 58

Figure 3- 12: unit cell for circuit simulation of super cell EBG structure 59

Figure 3- 13: Decomposition of unit cell for super cell EBG structure (a) metallic patch (b) meander-L bridge (c) short-L bridge 60

Figure 3- 14: The equivalent circuit for unit cell of super cell EBG structure 60

Figure 3- 15: Modeled vs. simulated S-parameters of super cell EBG structure 61

Figure 3- 16: transmission line with infinite periodic structures 64

Figure 3- 17: equivalent circuit model for periodic meander-L EBG structure.......... 65

Figure 3- 18: Dispersion diagram for Meander-L EBG structure obtained using the Bloch-Floquet Analysis using lumped circuit elements.. 68

Figure 3- 19: Equivalent circuit model for the periodic super cell EBG structure..... 69

Figure 3- 20: Dispersion diagram for super cell EBG structure 72

Figure 4- 1: Radiation loss for different structures.. 76

Figure 4- 2: Simulated port input impedance for different structures........................ 78

Figure 4- 3: Simulated port input impedance for on-center and off-center excitation 78

Figure 4- 4: (a) Near-field measurement setup 82

Figure 4- 5: Near field radiation intensity measured 1 cm above the board over the test line shown in Figure 4-4. Measurements performed for three different frequencies: (a) 480MHz, (b) 2.6GHz, and (c) 4.7GHz. 84

Figure 4- 6: Experimental setup for S_{21} Measurement for testing EMI shielding...... 86

Figure 4- 7(a)-(d): S_{21} parameter measured at different test point represented by normalized distance (with respect to the size of the board): (a) 0.15 (coinciding with the source location), (b) 0.44, (c) 0.75, and (d) 1. 88

Figure 4- 8: radiation resistance, input resistance, and directivity of a thin dipole with sinusoidal current distribution ($0 \le l \le 3\lambda$) [57] 90

Figure 4- 9: S_{11} measurement of monopole antenna.. 91

Figure 5- 1: Typical eye diagram generated with three data bits, showing the threshold level of logic “0” and “1”.. 95

Figure 5- 2: 4-layer PCBs with signal layer referring to solid power plane........... 97

Figure 5- 3: (a) 4-layer PCBs with signal layer referring to the Meander-L EBG patterned power plane (structure B) (b) Side-view. 98

Figure 5- 4: Comparison of S parameter for structure A (dotted line)........................ 99

Figure 5- 5: Comparison of input (original 2^7-1 PRBs) and output at time domain (a) and frequency domain (b) (note for each graph, the original signal is shown at top half, the output signal is shown at bottom half) ------- Structure A 101

Figure 5- 6: Comparison of input (original 2^7-1 PRBs) and output at time domain (a) and frequency domain (b) (note for each graph, the original signal is shown at top half, the output signal is shown at bottom half)------ Structure B.................................... 102

Figure 5- 7: Eye diagram for input (2^7-1 PRBs) and output of structure A (b) and structure B (c) 103

Figure 5- 8: Test geometry for Meander-L EBG patterned structure for differential pair configuration... 105

Figure 5- 9: Comparison of input (original 2^7-1 PRBs) and output (after passing structure B) with differential pair configuration at time domain (a) and frequency domain (b) respectively.. 106

Figure 5- 10: Eye diagram for Meander-L EBG patterned structure with differential pair configuration... .107

Figure 5- 11: 5-layer PCBs with Meander-L EBG structure sandwiched between two solid ground planes (a) 3D view (b) Side-view. 108

Figure 5- 12: Simulated eye diagram for single-ended trace of meander-L EBG structure with 5 layer PCBs configuration. 109

Figure 5- 13: (a) Test geometry for super cell EBG patterned structure for single-ended signal configuration (b) Corresponding eye diagram 110

Figure 5- 14: General configuration of EBG structure with driver to study the switching noise 112

Figure 5- 15: Simulation block diagram studying the voltage drop (Agilent ADS) represented by V_{out2} 113

Figure 5- 16: simulated voltage fluctuation (V_{out2}) on meander-line EBG patterned power/ground plane, where V_{in}: input voltage, V_{out}: output voltage 115

Figure 5- 17: Simulated voltage drop of meander line EBG patterned power plane compared with that of solid power plane 115

Figure 5- 18: Simulated voltage drop in power/ground power plane with decoupling capacitor (here the decap is chosen as 5pF) compared with the case without decap.116

CHAPTER 1

Introduction, Background, and Objective of the Dissertation

1.1 Motivation of the Work

Ideal power distributed system (PDS) requires power plane to provide clean power to integrated circuits. However, electromagnetic noise in power/ground planes can cause fluctuation or disturbance on the power supply voltage, which in turn leads to false switching in digital circuit or malfunctioning in analog circuit. This would eventually render the system inoperable. With the increasing of clock frequency and pulse edge rate, the decreasing of power supply voltage and noise margin, the anomalies created by the power/ground noises creates new challenges for electromagnetic interference/electromagnetic compatibility (EMI/EMC), signal integrity (SI) and packaging engineers [1, 2]. Simultaneous switching noise (SSN) has become one of major concerns. This noise also known as delta-I noise or power/ground plane bounce, has been discussed intensively over the last decade and different approaches have been taken to mitigate it [3, 4]. These methods consist of using discrete decoupling capacitors around sensitive integrated circuits to disrupt high-frequency fluctuations on the power planes by creating a low-impedance path between the planes at these frequencies [5, 6], the use of embedded capacitance where two conductor parallel planes with dielectric material in between them configured as a distributed capacitor [7, 8], the placement of resistive terminations on the board edges [9, 10], and via stitching [11], etc. The most common drawback of these methods is the limited frequency bandwidth that they can cover. In fact, except for embedded capacitance, none of the methods is able to go beyond few hundred megahertz and even embedded capacitance is not able to go much beyond the one gigahertz barrier and does not eliminate the propagation of higher-order modes. Embedded capacitance, on the other hand, is an expensive solution and reliability considerations limit its practical use. The question that remains unanswered is if there is alternative or complementary solution to the above methods to mitigate noise in power planes over wide frequency range, especially at higher frequency?

Electromagnetic Bandgap (EBG) structures, proposed in recent years, have proven effective for noise suppression at frequencies above 1GHz. EBG structure is a type of periodic metallic patterns which can form high impedance surface (HIS) to prevent propagation of electromagnetic wave over some frequency range. It was first proposed by Sievenpiper for antenna application to enhance the radiation efficiency by suppressing the surface wave [12, 13]. Later this concept of using EBG to suppress surface wave has inspired other authors to use it for suppressing noise in power plane [14-19]. The earlier structures proposed used three layers where the EBG pattern layer with specially designed via is inserted between the power plane and the ground plane, which make the fabrication more expensive. Recently, new planar EBG structures were reported for switching noise mitigation [20] [21], and for isolation in mixed signal boards [22]. These new structures consist of a two-layer power distribution system with one of the layers patterned in a periodic fashion, effectively creating a frequency filtering or EBG effect. These novel structures, in sharp contrast to previous multi-layer EBG structures, do not have vias. These features make such structures very attractive from the manufacturing and cost perspectives.

In this work, we investigate planar EBG patterned two-layer printed circuit boards (PCBs) used for noise mitigation. The primary thrust behind the conception of these new structures is increasing the noise suppression bandwidth (bandgap) in comparison to earlier structures. In the previous structure [21], L-shaped bridges were used between neighboring pads acting as inductance to form an LC electrical filter. The drawback of previous work is narrowness of the bandgap. So effect use of EBG structure in the parallel plate power plane for SSN suppression would require total bandwidth of EBG would cover up that of SSN need to be concerned, in addition to suppress the dominant peaks of the parallel plate resonance modes. So, the main objective of this research is to present a practical and very effective design to widen the EBG bandgap for mitigating the propagation of wideband simultaneous switching noise in high speed circuits.

While planar EBG structures offer clear advantages in comparison to multi-layer structures with or without vias, it is important to pay careful attention to the possibility of electromagnetic leakage through the perforated layer. In fact, in practical scenarios, as recent studies have demonstrated [23]-[26], the perforated power plane can lead to increased radiation from the PCB. These earlier works analyzing the field leakage from planar EBGs focused on the far field radiation [23]. However the far field does not give an indication of the near field radiation which is highly critical affecting radiated coupling to adjacent boards or devices that do not fall in the typical far field zone definition. Therefore, to obtain a comprehensive assessment of the EBG planar structures, near field properties have to be investigated to help us gain full knowledge of the radiation effects, which will facilitate the design of package. In this thesis we investigate the radiation effect of planar EBG structures on the near field in order to understand the potential for EMI within the PCB itself. Moreover, this dissertation introduces the novel concept of applying the planar EBG patterned power plane as an enhancing shield to reduce EMI coming from PCB power busses.

There is another important issue need to be addressed when considering the practical applications of the EBG patterned power plane in high speed system. As EBG structure, used as one of power planes, is embedded in multi-layer PCBs, signal traces referring to this imperfect power plane may degrade the signal quality for the high speed signal [21,27,28]. The reason is the discontinuity arising from this imperfect reference plane can induce strong reflection. The waveform of interest signal begins to change shape. For example for a digital signal a gate switching from logic “0” to logic “1” could be read as “0”, or a gate switching from logic “1” to logic “0” could be read incorrectly if there is a strong positive surge in the voltage. This will bring malfunction to the system. Therefore, in this thesis, we analyze the effect of using EBG planar structures on the signal integrity by studying what is referred to in the literature as the eye diagram.

1.2 Dissertation Organization

This thesis is organized as follows: the rest of this chapter covers some basic concepts often used throughout this thesis, which include simultaneous switching noise (SSN), electromagnetic bandgap (EBG) structures, and wave propagation in parallel plate waveguides (PPW).

In Chapter 2, simultaneous switching noise frequency range limitation is first discussed, and the typical simulation methods used to characterize the performance of EBG structures are reviewed. The concept of power planes with meander-line and super-cell EBG structures is introduced and investigated in detail.

Chapter 3 covers the development of lumped-element circuit modeling for the EBG structures. Here, both one dimensional and two dimensional model derivations are given. The physical mechanism behind these EBG structures is also briefly discussed. At the end, the dispersion diagram of EBG structures is calculated with periodic wave equation analysis.

Radiation from planar EBG patterned PCBs caused by switching noise is studied in chapter 4, and a novel concept of using these EBG structures for electromagnetic interference (EMI) reduction is presented. These concepts are verified using experimental measurements.

Chapter 5 is devoted to signal integrity. Potential methods to improve the signal quality of power plane with EBG patterned multi-layer printed circuit boards are introduced.

Finally, the conclusions and future work are given at the end of this thesis.

1.3 Simultaneous Switching Noise

Today's electronic packaging has progressed to packages that have power and ground planes. Computer systems and microprocessors utilize multi-layer printed circuit boards (PCBs) inside. These PCBs, which are made out of multiple metal layers separated by dielectric substrate, provide both a packaging functionality and a power distribution network for the components. The power distribution network is usually distributed on several metal layers, whereby the minimum requirement is to have at least two layers: one for the supply voltage V_{DD} and the other for the reference voltage V_{SS} or ground. These power supply layers usually extend over the entire width and length of the PCB and are often referred to as power planes. Typically the microprocessor or high-speed integrated circuit (IC) are mounted on the surface of the PCBs and are connected to the different layers using wire bonds, bond pads and vias. The typical configuration of a simultaneous switching noise environment for a multiplayer board is shown in Figure 1-1.

Simultaneous Switching Noise (SSN) is a voltage glitch induced at the chip/package power distribution system [3, 4, 29, 30]. When multiple internal gates and/or output drivers switch simultaneously, they induce a voltage drop in the chip/package power distribution. The simultaneous switching momentarily raises the ground voltage within the device relative to the system ground. This apparent shift in the ground potential to a non-zero value is known as simultaneous switching noise. It has always been present in digital circuits. In the past, simultaneous switching noise was not always noticeable because of slow edge rates and low pin count. As signal speed and number of pins increase in the modern IC, any designer working with high edge rate devices must be aware of these noise issues.

Simultaneous switching noise has traditionally been thought of as an inductance problem. In reality, the output current driving capability is much greater than the internal gates, this results in the rate of change in output driver switching current is much greater than that of internal gates. So the voltage magnitude of SSN is actually related to the inductance present between the device ground and the system ground, and the amount of current sunk by each output driver (neglecting the internal gates effects). It is given by equation (1.1):

$$V_{SSN} = L_{eff} \times \frac{di}{dt} \tag{1.1}$$

where the effective inductance comes from the via, chip interconnect (wire bonds and bond pads), and the board inductance.

$$L_{eff} = L_{via} + L_{board} + L_{\text{int}\,er} \tag{1.2}$$

In equation (1.1), V_{SSN} can be either positive or negative. It is often referred to as delta-I noise because of its direct dependence on the rate of change in current or more commonly, as ground bounce because the voltage glitch corresponds to an effective change of the supply voltage and can therefore be seen as a displacement of the ground level.

Initial work on the estimation of simultaneous switching noise was carried out in [29] and suggested that at a given time the maximum simultaneous switching noise can be obtained by multiplying (1.1) by the number of gates switching at the same time with the rate of current change *di/dt*:

$$V_n = nL_{eff} \frac{di}{dt} \tag{1.3}$$

where n is the number of outputs switch simultaneously. Equation 1.3 represents the worst case scenario when all devices switch at the same time. In [4] it was shown, however, that the total simultaneous switching noise saturates with the number of gates and that an accurate determination of the board effective inductance was critical in modeling the SSN.

In summary, the higher effective inductance and the higher the rate of change of driving current, the higher magnitude of ground bounce would be. This could in turn lead to a false logic or signal integrity issue: For example a gate switching from a logic “0” to a logic “1” could be read as “0” when there is a strong negative surge in the voltage or vice versa.

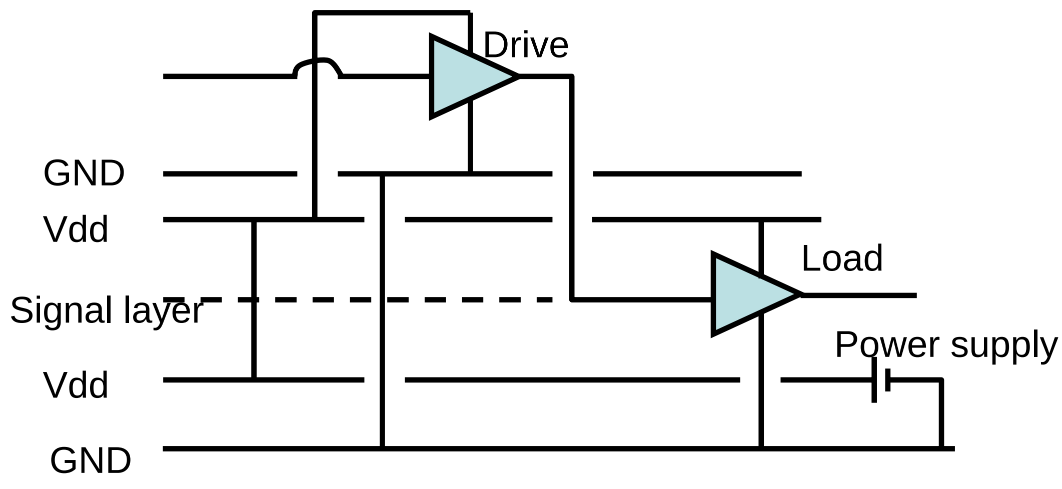

Figure 1-1: General configuration of a simultaneous switching noise environment for a multilayer board.

1.4 Electromagnetic Bandgap Structure

Electromagnetic bandgap (EBG) structures have generated considerable interest in recent years, mostly because of their ability to mitigate electromagnetic wave propagation at microwave frequencies. It is an array of metallic periodic pattern placed in a waveguide structure which can form high impedance surface (HIS). The concept of EBG structure was first introduced by Sievenpiper for antenna application in order to suppress surface wave [12], [13]. The top and side views of a typical HIS structure is shown in Figure 1-2. The HIS structure consists of an array of metal protrusions on a flat metal sheet. They are arranged in a two-dimensional lattice, and are usually formed as metal plates, connected to the continuous lower conductor by vertical posts. They can be visualized as mushrooms or thumbtacks protruding from the surface. The space between the two layers is typically filled with a dielectric. The spacing between the patch centers defines the array period. This structure has high surface impedance. Therefore, it rejects surface currents and it prevents (stop-band) or permits (pass-band) propagation of surface waves. The waves are attenuated as evanescent modes in a manner similar to what happens in waveguide below their cutoff frequency. The stop and pass-band range is determined by the patch dimensions.

Because of this special property, electromagnetic bandgap structure is in some sense named as perfect magnetic conductor (PMC). A perfect magnetic conductor does not exist in nature, but is instead a mathematical model that does not support electric surface currents. More precisely, the boundary condition of a PMC states that any tangential magnetic field (H_{tan}) vanishes on its surface. However, there may be a nonzero tangential electric field (E_{tan}) on the surface of the PMC. The PMC is the electromagnetic dual, or in layman's terms the opposite of a perfect electric conductor (PEC). Metals are essentially PECs. In the case of the PECs, E_{tan} is zero on the boundary and H_{tan} is nonzero. Since the electric surface current density is given by $\vec{J} = \hat{n} \times \vec{H}$ where n is the unit vector normal to the surface, it is obvious that a PEC supports electric surface currents while a PMC does not. The boundary conditions for PEC and PMC are shown in Figure 1-3 respectively. The ability of EBG or PMC to cut off surface currents is what makes it very effective at improving isolation between antennas. Other applications range from antennas to filters, to high power components, and magnetic conductor surfaces.

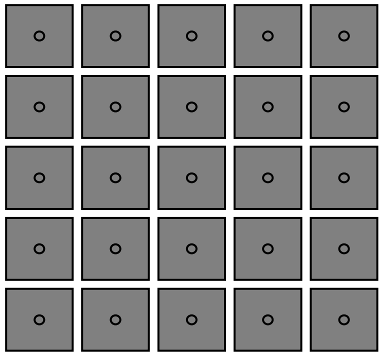

(a)

(b)

Figure 1-2: Illustration of 3D electromagnetic bandgap structure with vertical post (a) top view (b) side view

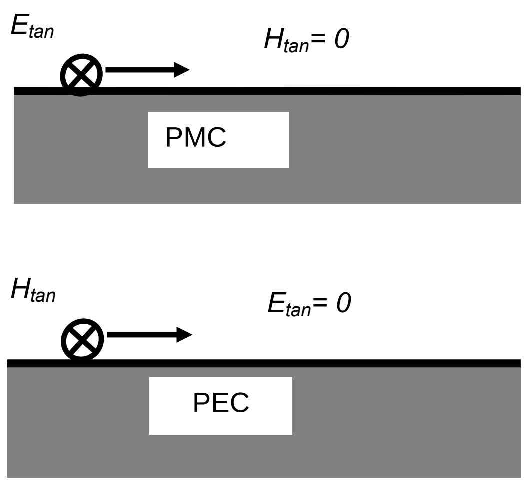

Figure 1-3: Boundary conditions for PMC and PEC

Recently, EBG structure has been implemented in power distributed system to mitigate noise in power planes [14-19]. The earlier structure proposed used three layers and a complex via design. The top and bottom plane are typical solid power planes used to supply DC voltage. The EBG patterned layer is inserted between them. An example of this three layer structure is shown in Figure 1-4.

In subsequent works, EBG structures developed to a planar architecture of uniform substrate material patterned with periodic metallic patches. One of the structures is shown in Figure 1-5 [20]. This structure does not have vias, so it is a two-dimensional, or planar structure. It only uses patterned metallic patches to replace one of the traditional power planes. This feature makes such planar EBG structure very attractive from manufacturing and cost perspectives. Our research is focused on this type of planar EBG structures.

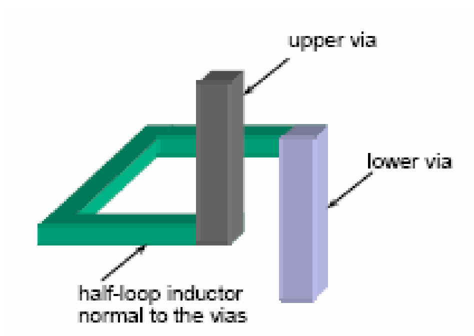

(a)

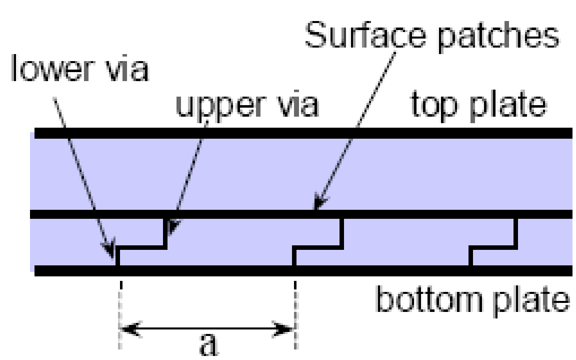

(b)

Figure 1-4: Three layer EBG structure with inductance enhanced vias (a) single-loop inductive element (b) cross section of structure [15]

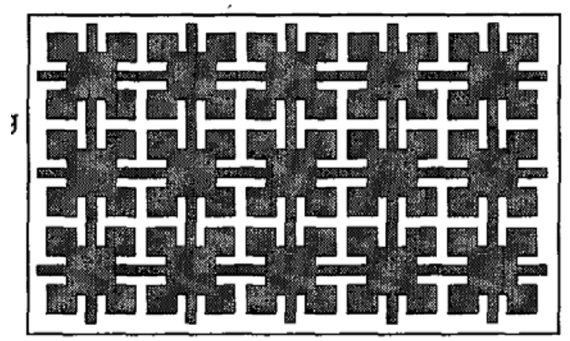

(a)

(b)

Figure 1-5: Planar EBG structure (a) top view (b) side view [20]

1.5 Parallel Plate Waveguide

The parallel plate waveguide (PPW) is the simplest structure consisting of two parallel perfect electrical conductor plates. It provides ground and supply voltage of the power distribution network. This type of structures can therefore support TE, TM and TEM modes. In the idealization of the parallel plate waveguide illustrated in Figure 1-6, the dimension in the y direction, the thickness d of the waveguide, is assumed much smaller than that in the z (direction of wave propagation) and x directions such that all fringing fields and any variation in the x direction can be neglected.

The TEM waves correspond to the case where there are no electric or magnetic fields in the direction of propagation. TE and TM modes correspond to cases in which the fields have no electric or magnetic field in the direction of propagation, respectively.

For detail derivation of the field solution in a parallel plate waveguide, the reader is referred to [31] and [32]. Here only the main steps and final results are given.

For TEM wave, the solution can be solved by Laplace's equations for the scalar electrostatic potential $\Phi(x,y)$:

$$\nabla^2 \Phi(x, y) = 0 \tag{1.4}$$

with boundary condition:

$$\Phi(x,0) = 0 \tag{1.5}$$

and

$$\Phi(x, d) = V_{dd} \tag{1.6}$$

The final field can be calculated as:

$$\vec{E}(x, y, z) = -\hat{y}\frac{V_{dd}}{d}e^{-jkz} \tag{1.7}$$

$$\vec{H}(x, y, z) = -\hat{x}\frac{V_{dd}}{\eta d}e^{-jkz} \tag{1.8}$$

where

$$k = \omega\sqrt{\mu\varepsilon} \tag{1.9}$$

and

$$\eta = \sqrt{\frac{\mu}{\varepsilon}} \tag{1.10}$$

Here it is important to note that the TEM waves are excited and supported by the parallel-plate waveguides at all frequencies.

For TM wave, from Helmholtz wave equation:

$$\left(\frac{\partial^2}{\partial y^2}+\gamma^2\right)e_z(x,y)=0 \qquad (1.11)$$

where $$\gamma^2=-k^2+\frac{\mu\varepsilon\omega^2}{c^2} \qquad (1.12)$$

and $$E_z(x,y,z)=e_z(x,y)e^{-jkz} \qquad (1.13)$$

Applying a PEC boundary condition at x=0 and x=d:

$$e_z(x=0)=0 \qquad (1.14)$$

$$e_z(x=d)=0 \qquad (1.15)$$

we have:

$$\gamma=\frac{n\pi}{d} \qquad (1.16)$$

The wave propagation constant is then given as:

$$k^2=\frac{\mu\varepsilon}{c^2}\left(\omega^2-\omega_c^2\right) \qquad (1.17)$$

where:

$$\omega_c^2=\frac{n^2\pi^2c^2}{\mu\varepsilon d^2} \qquad (1.18)$$

the cutoff frequency for the TM_n wave can then be defined as:

$$f_c=\frac{n}{2d\sqrt{\mu\varepsilon}} \qquad (1.19)$$

For the TE wave, following the similar derivation, the propagation constant and the cutoff frequency are the same as those of TM wave.

For practical consideration, typical power planes have a thickness of less than 2 mm. From the equations above, the calculated fundamental cut-off frequencies of the parallel-plate TE and TM modes will be in the order of tens or hundreds of GHz, so TE and TM modes are not a major concern for systems operating at 10 GHz and below. The only modes of concerns are the TEM modes and the resonance modes induced by the finiteness of the power planes. Actually, in the calculation of the parallel-plate waveguide modes, it is assumed that the plates have infinite length in the z-direction. In practical power planes, the width (*w*) and length (*l*) of the plates are finite. In this case, waves will be reflected back and forth when they propagate to the edge of the boards. Therefore, in addition to the parallel-plate TEM modes, rectangular cavity modes are also excited. Both TE_{mnp} and TM_{mnp} modes are excited. Their cut off frequency is given by the same equation:

$$f_{mnp} = \frac{1}{2\pi\sqrt{\mu\varepsilon}}\sqrt{\left(\frac{m\pi}{w}\right)^2 + \left(\frac{n\pi}{l}\right)^2 + \left(\frac{p\pi}{d}\right)^2} \tag{1.20}$$

Since *d* is very small compared to *l* and *w*, only TE_{mn0} and TM_{mn0} modes have low enough resonance frequencies that fall into the frequency range of interest (below 10 GHz), hence:

$$f_{cmn} = \frac{1}{2\pi\sqrt{\mu\varepsilon}}\sqrt{\left(\frac{m\pi}{w}\right)^2 + \left(\frac{n\pi}{l}\right)^2} \tag{1.21}$$

For our practical PCB board with dimension of 90mmx150mmx1.5mm, filled with FR-4 of dielectric constant 4.4, the resonant frequencies will appear at: 480MHz, 920MHz, 960MHz, and so on. Obviously, switching noise has its maximum impact if it is generated at the resonance frequencies of the parallel plate cavity.

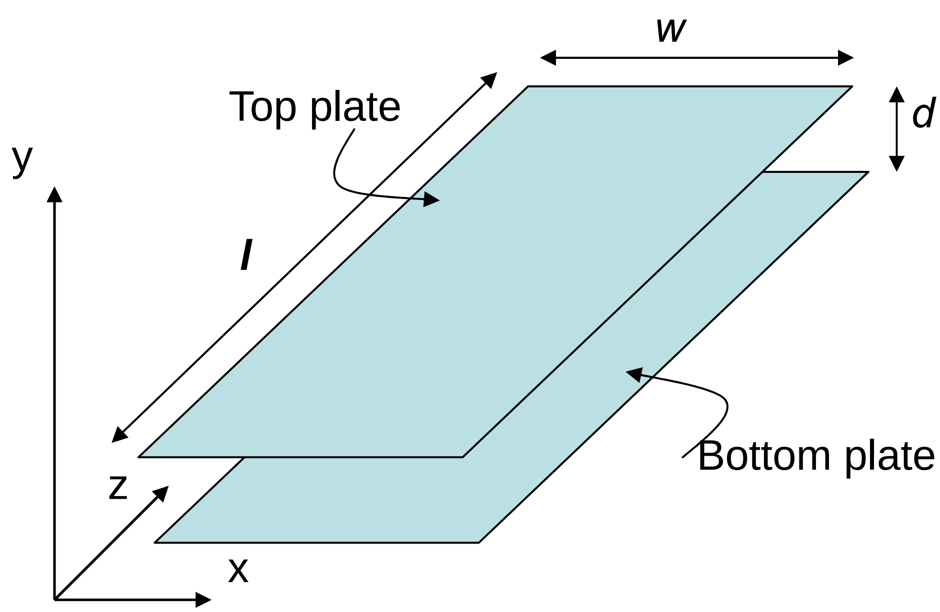

Figure 1-6: Diagram for an ideal parallel plate waveguide as a model for the power planes of a PCB.

CHAPTER 2

Planar EBG Structure Design and Wideband Mitigation of Simultaneous Switching Noise

2.1 Simultaneous Switching Noise Frequency Limitation

2.1.1 Introduction

As discussed in chapter 1, the magnitude of simultaneous switching noise (SSN) is proportional to the rate of change of charging/discharging currents. With the increase of clock frequency, problems may arise when the magnitude of noise reaches to fractional signal driving voltage. This will result in malfunctioning of digital circuit system. For example, when SSN is transferred to the outside through an output buffer driving low, i.e., logic “0”, if the noise magnitude is higher than the V_{IL}, the threshold of the input being driven, there is a possibility that the glitch will be recognized as a logic “1”, and vice versa.

The purpose of using electromagnetic bandgap (EBG) structure is to mitigate the propagation of the SSN. EBG structure has a limited bandwidth. What we hope is that the total bandwidth of the EBG will include the bandwidth sustaining the SSN.

Therefore we need to have detailed information on the SSN frequency range. In general, the lower frequency edge of SSN begins at the hundreds of Megahertz. It is important to define the upper frequency edge of SSN, which determines the requirement for the EBG upper frequency limit. Actually the upper frequency edge of SSN depends on the clock signal waveform. In the following section, a detail discussion of spectral content of SSN will be given.

2.1.2 Upper frequency edge of SSN

The waveforms of primary importance in digital circuits are those which represent clock and data signals. This analysis is based on the assumption that the clock or data signal has a generic trapezoidal waveform as shown in Figure 2-1(a). The clock signal is a periodic waveform with period T, magnitude S, pulse duration p, and rise/fall time τ. To analyze the waveform of Figure 2-1 the following assumptions are made:

1) Rise and fall times are equal: $\tau_r = \tau_f = \tau$

2) The waveform is periodic in time, with period T, frequency $f_0=1/T$, and angular frequency $\omega = 2\pi f_0$

If the waveform of CMOS output voltage is assumed to follow inversely that of clock signal (input driving voltage), the driving current, due to charging or discharging, will have a waveform as shown in Figure 2-2. The final waveforms for the SSN can be approximately represented as a trapezoidal waveform (Figure 2-1(b)). The magnitude of the SSN is defined by equation (1.1).

Next we look at the spectral content of this waveform using Fourier transforms. The purpose is to find the dependence of spectral content of switching noise on the clock/signal parameters.

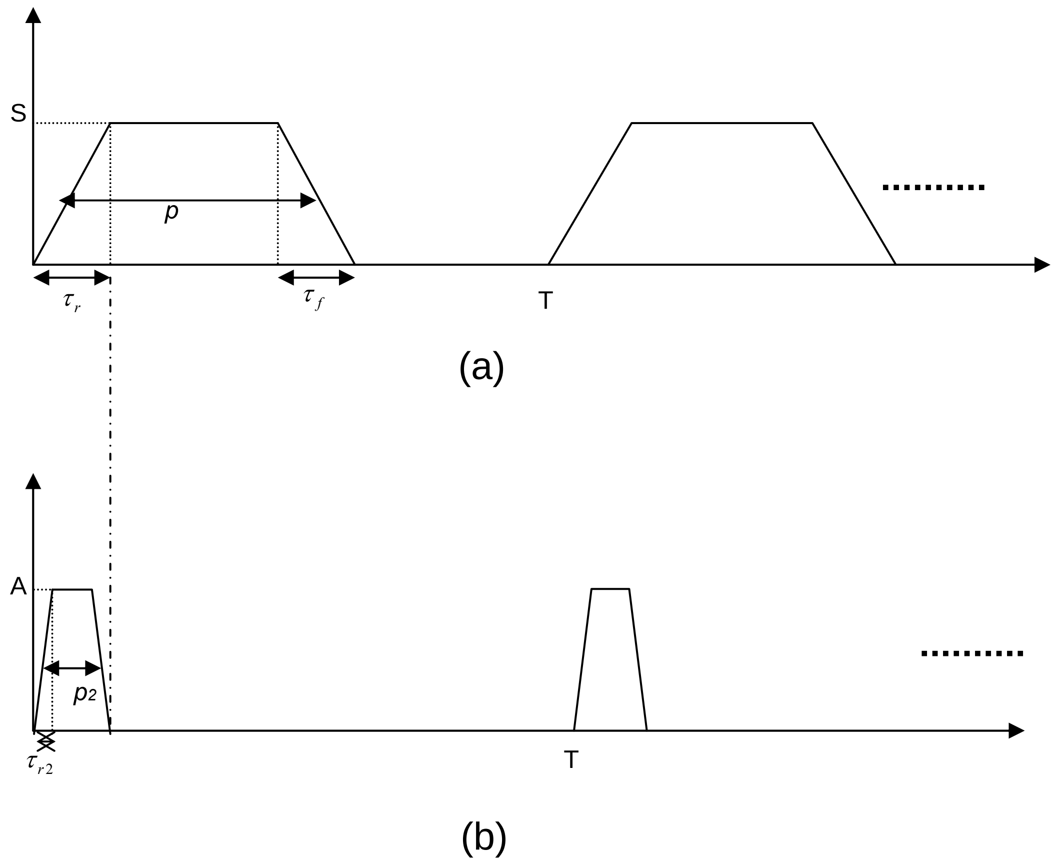

Figure 2- 1: Periodic trapezoidal pulse train representing (a) the clock or data signals of digital system. (b) SSN waveform due to the charging/discharging current

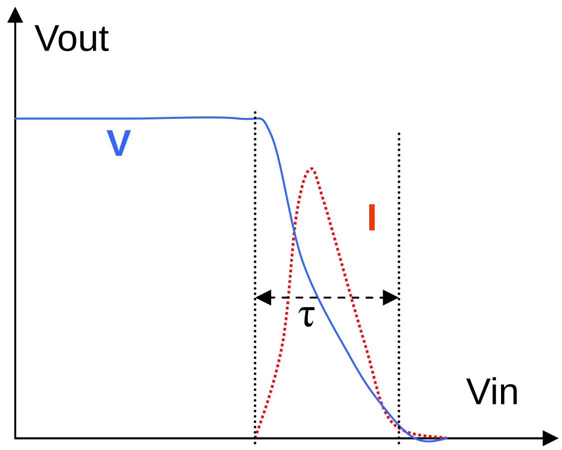

Figure 2- 2: Typical CMOS output driver switching characteristics

The SSN waveform as shown in Figure 2-1(b) is a periodic train of trapezoidal shaped pulses, in which each pulse is described by period T, magnitude A, rise/fall time τ_{r2}, and pulse duration p_2. As we notice, p_2 is actually limited by clock signal transition time τ, and can be approximated as $\tau \cong p_2$. Then the amplitude of the spectral components lies on an envelop [33, 34], that is:

$$envelop = 2A\frac{\tau}{T}\left|\frac{\sin(\pi\tau f)}{\pi\tau f}\right|\left|\frac{\sin(\pi\tau_{r2}f)}{\pi\tau_{r2}f}\right| \quad (2.1)$$

To generate the bounds for this spectrum, we express equation (2.1) using a logarithmic scale:

$$20\log_{10}(envelop) = 20\log_{10}(2A\frac{\tau}{T}) + 20\log_{10}\left|\frac{\sin(\pi\tau f)}{\pi\tau f}\right| + 20\log_{10}\left|\frac{\sin(\pi\tau_{r2}f)}{\pi\tau_{r2}f}\right| \quad (2.2)$$

The expression above is actually composed of three plots:

$$\text{Plot 1} = 20\log_{10}(2A\frac{\tau}{T}) \tag{2.3}$$

$$\text{Plot 2} = 20\log_{10}\left|\frac{\sin(\pi\tau f)}{\pi\tau f}\right| \tag{2.4}$$

$$\text{Plot 3} = 20\log_{10}\left|\frac{\sin(\pi\tau_{r2} f)}{\pi\tau_{r2} f}\right| \tag{2.5}$$

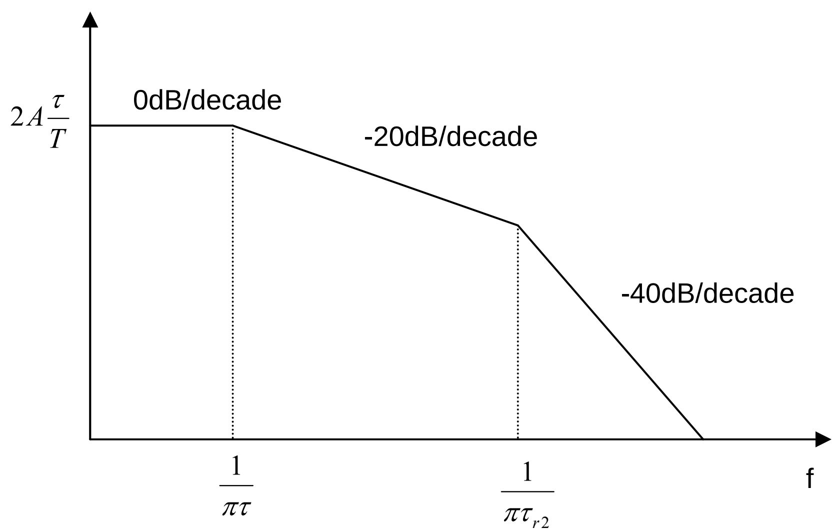

Figure 2- 3: Bounds on magnitude spectrum of a trapezoidal pulse train

Plot 1 has 0dB/decade slope. Plot 2 has two asymptotes. The first asymptote has a 0dB/decade slope. The second asymptote begins at $f = 1/\pi\tau$, with a slope -20dB/decade. Plot 3 also consists of two asymptotes, one of which has a 0 dB/decade slope and the other has a -20dB/decade slope. The two asymptotes join at $f = 1/\pi\tau_{r2}$.

The composite asymptote is the sum of these asymptotes, as shown in Figures 2-3. The composite asymptote thus consists of three straight-line segments. The first segment is due to plot 1 and has a slope of 0dB/decade, with a magnitude 2Aτ/T. The second segment has a slope of -20dB/decade and is due to plot 2. The third segment has a slope of -40dB/decade and is due to the combined effects of plots 2 and 3.

From the spectrum bound Figure 2-3, it clearly shows that the high frequency content of a SSN pulse train is due primarily to the rise/fall time of the clock signal. Signals having small rise/fall times will have larger high-frequency spectral content than that of signal having larger rise/fall times. Thus, faster clock frequency and faster transition time, the higher the frequency edge of the SSN noise spectrum. Therefore, in general we need to pay attention to the upper frequency edge of SSN, which can reach 10 times higher than the primary clock signal of a digital system.

Another important parameter is the duty cycle, $D = \frac{\tau}{T}$, which defines the ratio of the pulse width to the signal period. Figure 2-4 shows the dependence of pulse train duty cycle D on the spectral bounds ($f_0 = 1/T$, $1/\pi\tau = f_0/\pi D$). The graph shows that the starting level of spectrum depends on the pulse width. The narrower the pulse width is, the smaller the spectral level would be. The first breakpoint for the smaller duty cycle D_2 will lie on the -20dB/decade asymptote for the larger duty cycle D_1. In general, smaller the duty cycles reduce the lower frequency spectral content of the waveform, but it will not affect the higher frequency spectrum.

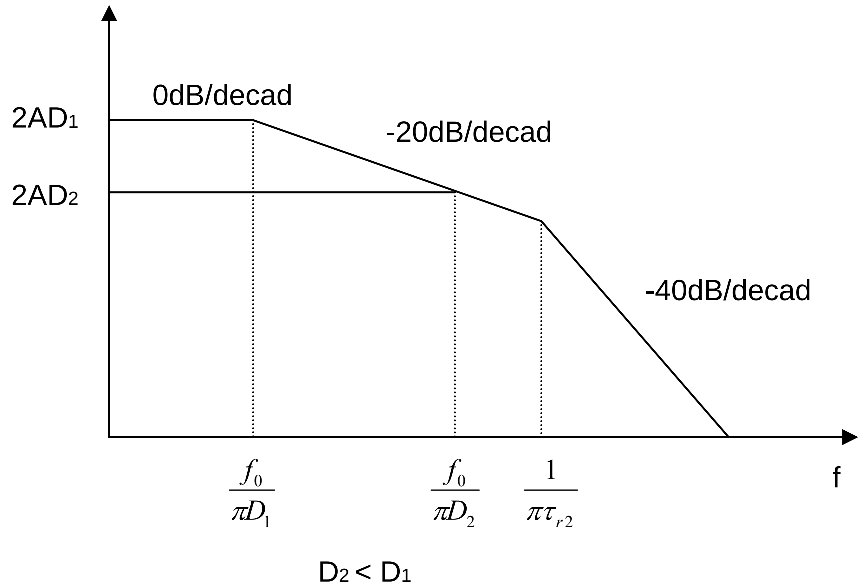

Figure 2- 4: Effect of duty cycle on the spectral bounds of trapezoidal pulse train

As an example, if the clock frequency is 1GHz, the rise/fall time of clock signal counts as 20% of the period, then the pulse width of the trapezoidal waveform for the SSN will be limited by this rise/fall time. From the spectrum bounds shown in Figure 2-3, it is estimated at f =12GHz, the amplitude of spectrum is attenuated by nearly 20dB compared with its low frequency spectrum magnitude. In general, the upper edge frequency of SSN is thought to be 10 times the clock frequency, so the bandwidth of SSN we are interested in this study is from several hundred megahertz to up to over 10 GHz.

2.2 Characterization of EBG Structures

2.2.1 Introduction

Different methods are used for the analysis, design and modeling of EBG structures. Some of these numerical methods include the Method of Moments (MOM) [35] which employs the pulse expansion functions, the Transmission Line Matrix (TLM) method [36], the Finite-Difference Time-Domain (FDTD) method [37] and Finite Element Method (FEM) [38]. In this work we use a commercially available simulation tool, Ansoft HFSS [39], which is based on the finite element method. HFSS is an interactive software package for calculating and analyzing three-dimensional (3D) electromagnetic radiation problem involving complex structures. During our study, two methods are used to characterize the EBG structures. One is a full wave complete space analysis method; the other is symmetry boundary method.

2.2.2 Full wave complete space analysis

Full wave complete space analysis method is used in our simulation throughout this thesis. This method gives a complete field solution of proposed EBG structures.

For the planar type of EBG structures discussed in this work, the radiation boundary is adopted to mimic radiation into infinite space.. The requirement of using ABC is the simulated structure should be electrically far away from the boundary to minimize the effects of reflective waves [39]. Typically, the spacing between the radiated structure and the boundary should be greater than $\lambda/4$, where λ is the wavelength in the medium. For a practical consideration of our EBG structure, the simulation frequency begins from as low as 200MHz, which requires the spacing to be over 30cm. This renders the simulation very inefficient due to large memory requirements. However, since the radiation from the powr planes is weak in comparison to antennas, we expect that the λ/4 rule to be unnecessarily stringent leading to inefficient simulations. In fact, we carried out several simulations where the distance between the outer edge of the structure and the mesh-truncation boundary (where the boundary condition is enforced) is decreased incrementally and found that sufficient accuracy can be obtained by using a distance of 3cm instead of 37cm (as would be expected if the λ/4 rule is followed). The results presented in Figure 2-5(b) where two different cases having a distance from the outer edge of the structure to the boundary condition is set at 10cm and 3cm clearly show that the 3cm case provides not only good accuracy but also sufficient computational savings

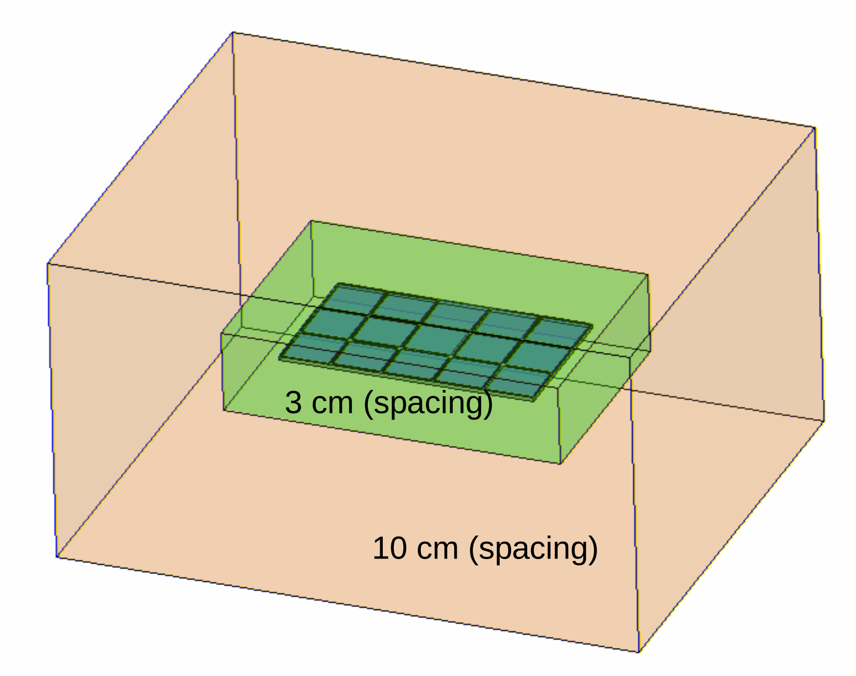

(a)

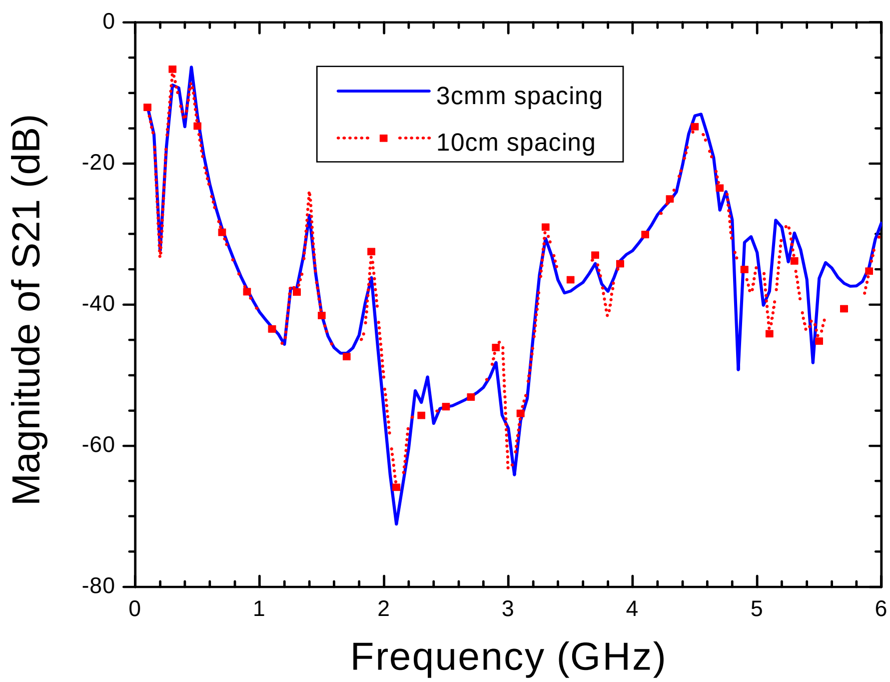

(b)

Figure 2- 5: EBG structure with different spacing (3cm, 10cm) from radiation boundary (a) simulation structure geometry (b) S-parameter simulation result

In general, however, while full wave analysis method can provide a fairly accurate result, it heavily consumes significant memory resource (execution time and memory allocation). Next we introduce the symmetry boundary method, which takes advantage of the symmetric property of EBG structures, thus resulting in significant computational savings.

2.2.3 Symmetry boundary method

This method relies on the special symmetric properties of the structures [39]. In HFSS simulation, actually there are two kinds of symmetry boundaries. One is the perfect E symmetry boundary; the other is perfect H symmetry boundary. By using symmetry boundaries it enable us to model only part of a structure, which reduces the size or complexity of the design, thereby shortening the solution time.

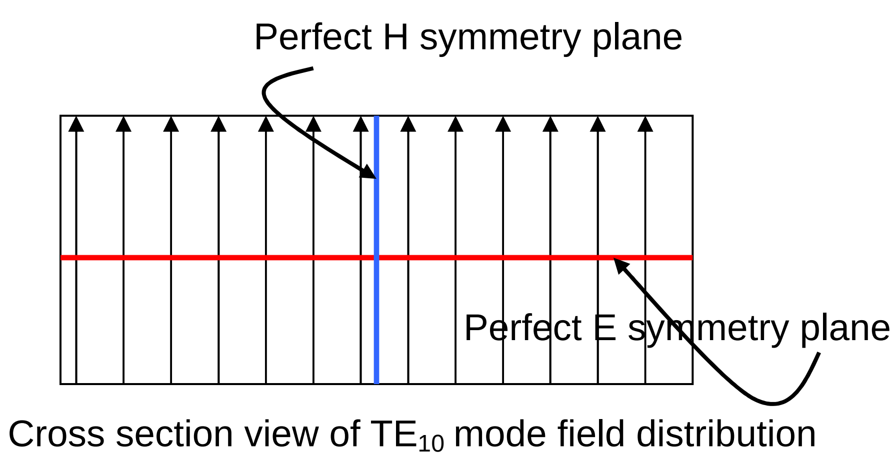

Figure 2- 6: Diagram showing the symmetric boundary for perfect E and H

If the symmetry is such that the E-field is normal to the symmetry plane, it belongs to perfect E symmetry boundary condition. For perfect H symmetry boundary condition, the symmetry is such that the E-field is tangential to the symmetry plane. Perfect E or H symmetry boundary in rectangular waveguide is shown in Figure 2-6.

For our EBG structure, the field inside is TEM mode as discussed in section 1.5. If we choose a computational space as shown in Figure 2-7, the lateral sides of this model are “symmetry boundary conditions” that create a double-mirror-like structure in which the model would look infinite in the y-direction (both positive and negative). For the E field is tangential along the symmetry plane, it satisfies perfect H symmetry boundary condition. Here instead of computing the field in the entire space, the simulation is reduced to a one dimensional problem by using this symmetry boundary method. The simulation result is shown in Figure 2-8. When compared with full computational space simulation, there is good agreement between the two. This method assumes the size of the board in the y direction is infinite, although in reality it is not the case.

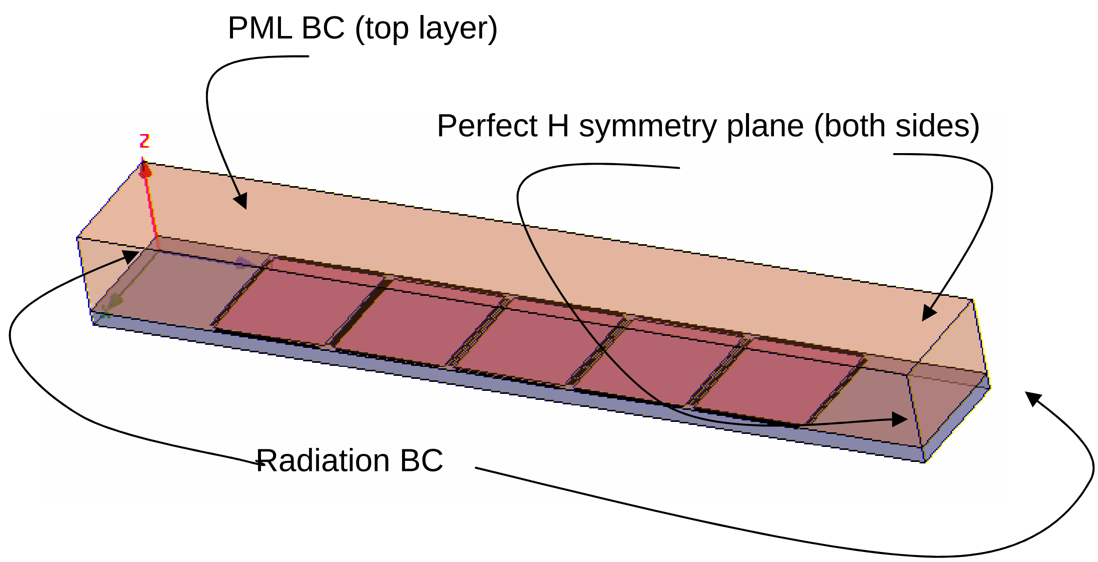

Figure 2- 7: Diagram representing the symmetric boundary model used to derive the bandgap of EBG structure

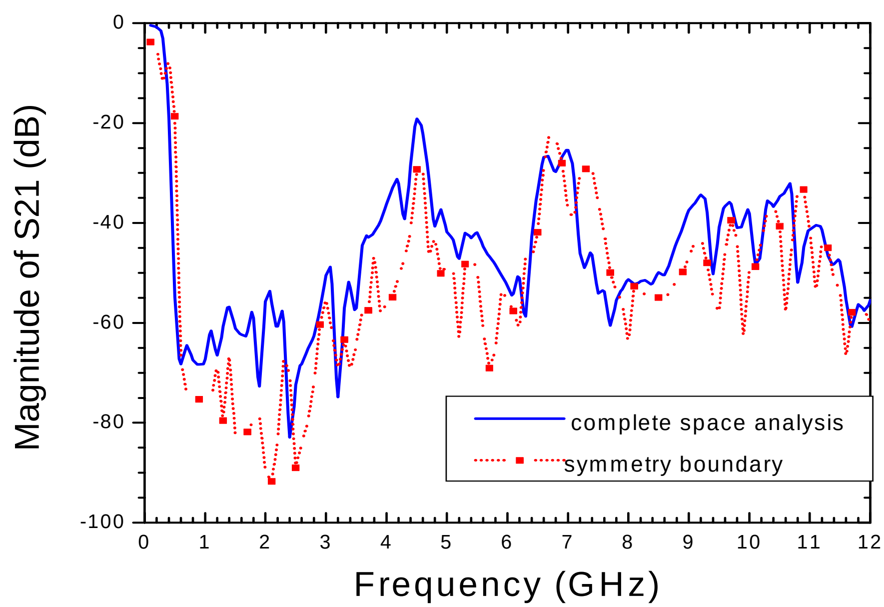

Figure 2- 8: Comparison of S parameter simulation using two different methods: one is full wave complete space method (solid line); the other is symmetry boundary method (dotted line).

2.3 Planar EBG Structures

2.3.1 Structure design

The underlying principle behind the two-layer EBG-embedded power plane structure is to filter out switching noise and other noise sources propagating within the power planes while providing a low-impedance path for DC current on each layer. Figure 2-9(a) shows the proposed two-layer power/ground plane with meander line EBG structure. The whole dimension of this structure with 3x5 unit cells is 90mm x 150mm. The solid layer can be used for one voltage level and the EBG-patterned layer is used for the second voltage level. Between these two layers, a uniform substrate material FR-4 with dielectric constant 4.4 and layer thickness of 1.54mm is selected due to its manufacturing flexibility at our local facilities.

The schematics of the unit cell of size 30mm x 30mm and its corresponding parameters are shown in Figure 2-9(b). For one-dimensional wave propagation, the unit cell of this EBG structure can be modeled with the equivalent circuit as shown in Figure 2-9(c). This qualitative model is inspired by the physical behavior of the field distribution in the patch. It consists of two parts. The first part describes the propagation characteristics between the EBG patch and continuous power plane, represented by equivalent inductance L_p and capacitance C_p. The second part characterizes the bridge effects between two adjacent unit cells, where the gap between the two neighboring unit cells induces the fringe capacitance C_b, and the bridge connecting the neighboring unit cells as the inductor L_b. So this EBG structure can be conceptually viewed as an electrical filter of parallel LC resonator.

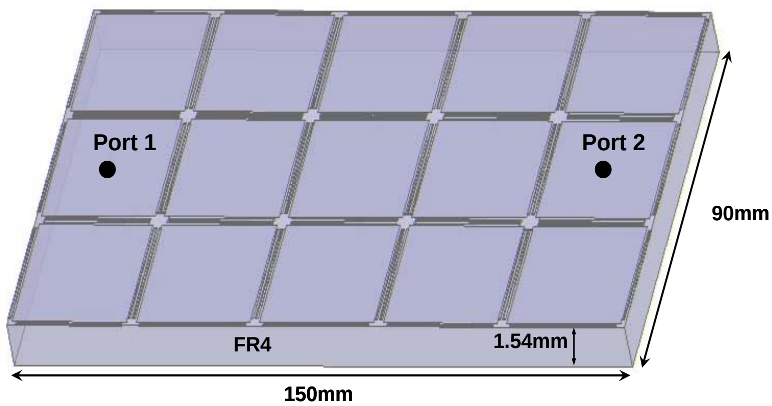

(a)

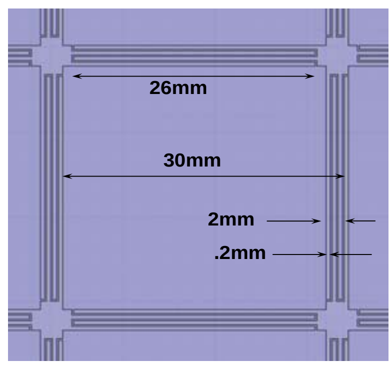

(b)

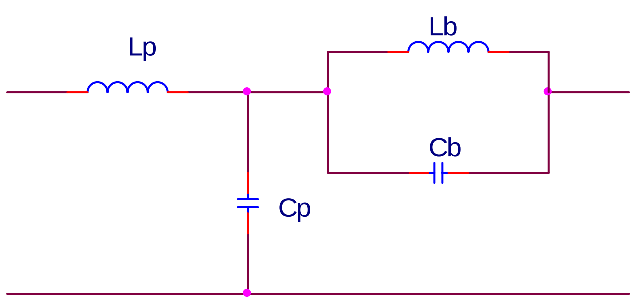

(c)

Figure 2- 9: (a) Planar EBG structure with Meander-L bridge showing the location of the ports used for S21 parameter measurements. (b) Unit cell showing the Meander Line bridge and dimensions. (c) Qualitative equivalent circuit model for unit cell of the Meander-L EBG structure

The center frequency of the stop-band for the EBG structure can be expressed semi-quantitatively as $f_0 = 1/(2\sqrt{(L_bC_b)})$. Consequently, one observes that in order to effectively implement the EBG structure in the lower frequency region, longer bridge length, corresponding to an increase in inductance, would be required. Therefore, we introduce a meander line as the connecting bridge (DC link) between adjacent patches. The width of meandered line is 0.2mm, which is within the fabrication tolerance capability of our lab facility LPKF ProtoMat machine.

2.3.2 Fabrication

EBG structures are fabricated with LPKF ProtoMat C100/HF machine. It is a circuit board plotter which can be used to produce high quality prototype for HF and microwave PCBs. The geometry of this machine is shown in Figure 2-10.

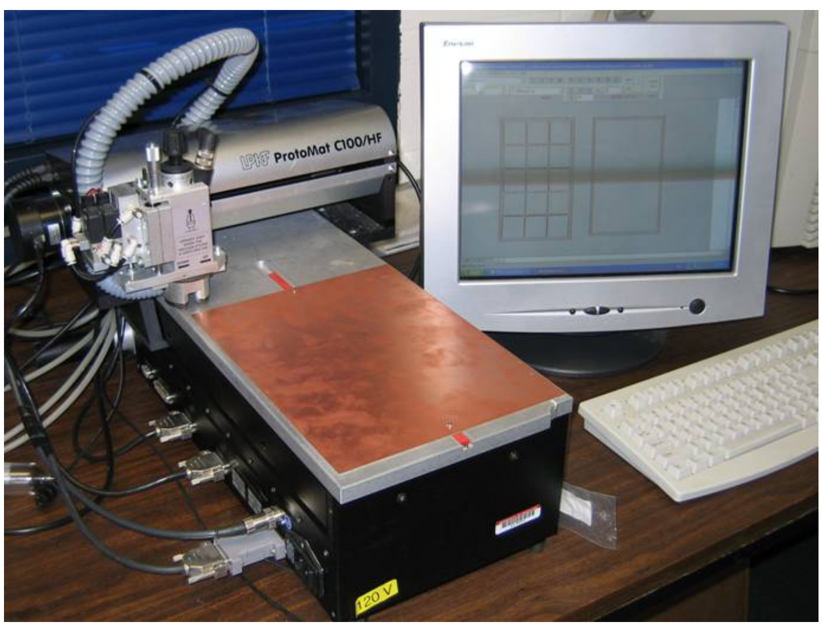

Figure 2- 10: LPKF ProtoMat C100/HF circuit plotter used for our prototype

The basic steps to make a board are as follows: First the pattern is designed with commercial CAD program to generate Gerber, Excellon, or DXF data file. The data is then transformed to the CircuitCAM environment, where you can define the milling tracks, drill size, and insulation width, etc. Finally the file is transformed to BoardMaster program, which controls the operation of ProtoMat machine, to implement the physical etching on the PCBs.

The real board which we made for meander line EBG structure is shown in Figure 2-11.

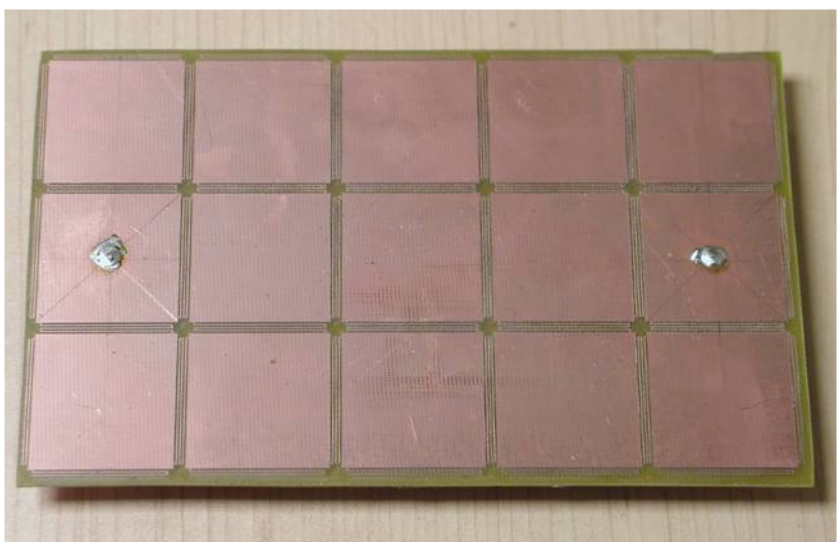

Figure 2- 11: Photo of top view of meander line EBG structure, two soldering points showing the two test ports

2.3.3 Simulation and experimental result

Performance of the EBG structures is characterized by S-parameters measured with the Agilent E8364A vector network analyzer (VNA). Each test port is located at the patch center as shown in Figure 2-11. From the S-parameters which in principle represent the frequency response of the power plane, the center frequency, the fractional bandwidth, the noise mitigation bandwidth and the maximum insertion loss in the stopband can be extracted.

In Figure 2-12, we show the simulation result of the EBG surface with meandered lines as obtained from the Ansoft HFSS full wave analysis method along with the measured data. In the HFSS analysis we use a lumped gap source which is located internally in the structure to represent the wave port. The lumped port is assigned between the top patch plane and solid bottom plane. The data shows an ultra-wide bandgap is achieved using this new structure with strong agreement between simulation and measurements. The stopband frequency range is observed to extend from approximately 450MHz to 12 GHz and beyond. The definition of bandwidth adopted here is the continuous frequency range over which the magnitude of the S_{21} is maintained below -28dB. (There is no standard definition for suppression bandwidth in the context of switching noise as the degree of suppression is application specific. Here, the -28dB was chosen for convenience as it represents significant suppression in comparison to the reference case.)

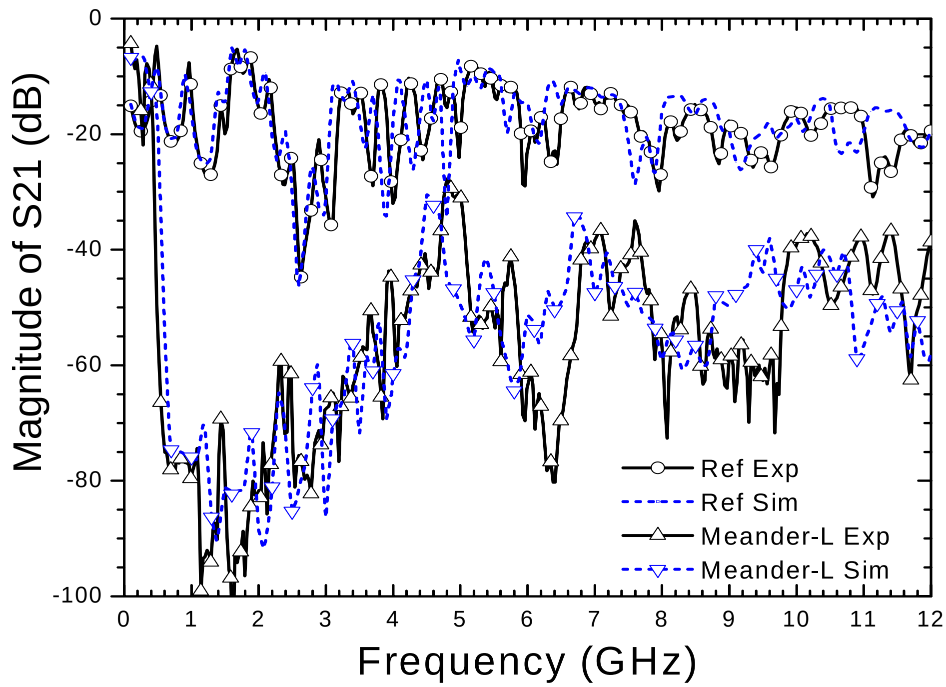

Figure 2- 12: Numerical simulation and measurement result for magnitude of S_{21} between two ports across EBG patches having Meander line bridge (Meander-L). Comparison is made with a two layer power plane (Reference)

2.3.4 Super cell EBG structure

Here we introduce the concept of a *super cell*. The super cell is formed by two patches with different topologies. The new super cell is cascaded resulting in a new structure that is expected to embody the bandgaps arising from the use of each of the two topologies if they were used separately, in addition to the bandgap arising from the increased periodicity formed by the new super cell. Figure 2-13(a) shows the super cell structure composed of adjacent EBG patches with two different connecting bridge topologies--a straight line and a meander line. The patch is kept at the same size of 30mm x 30mm. It shows a schematic of the entire board with similar overall dimensions as before. Notice that by the introduction of the two separate patch topologies and cascading them as shown in Figure 2-13(b), we have, in effect, doubled the period of the EBG structure. Based on the transmission line model of periodic structures, the increase in the period leads to a direct decrease in the lower edge of the frequency bandgap [40, 41]. Figure 2-14 gives the measurements of the magnitude of the S_{21} parameter. We see not just an appreciably wide bandgap, but more importantly, a downward shift, as predicted, to approximately 250MHz, in the lower edge of the bandgap. To highlight the bandwidth improvement at the lower end of the bandgap, we show in Figure 2-15 a comparison between the two cases. The 175MHz bandwidth improvement realized by the super cell can lead to cost reduction by eliminating decoupling capacitors needed to maintain minimal noise in the sub 500MHz range.

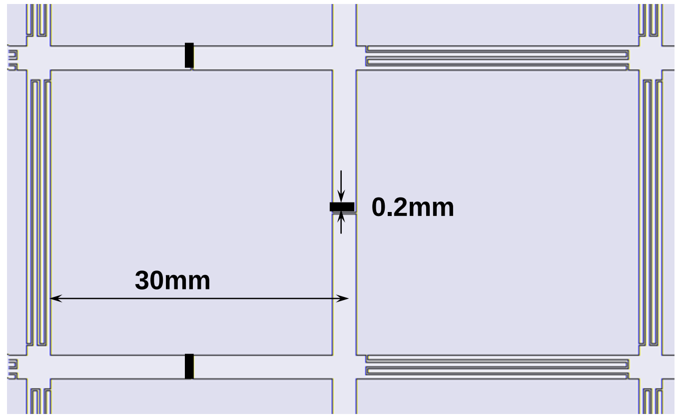

(a)

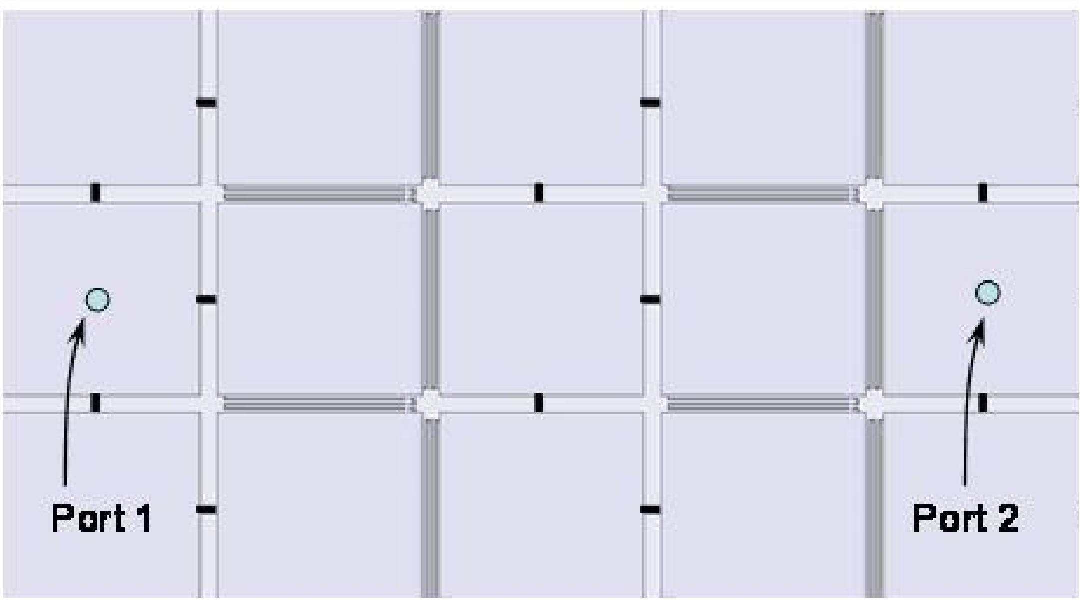

(b)

Figure 2- 13: (a) Schematic top view of a super cell with dimensions

(b) Top view of the board showing the layout of the super cell structure.

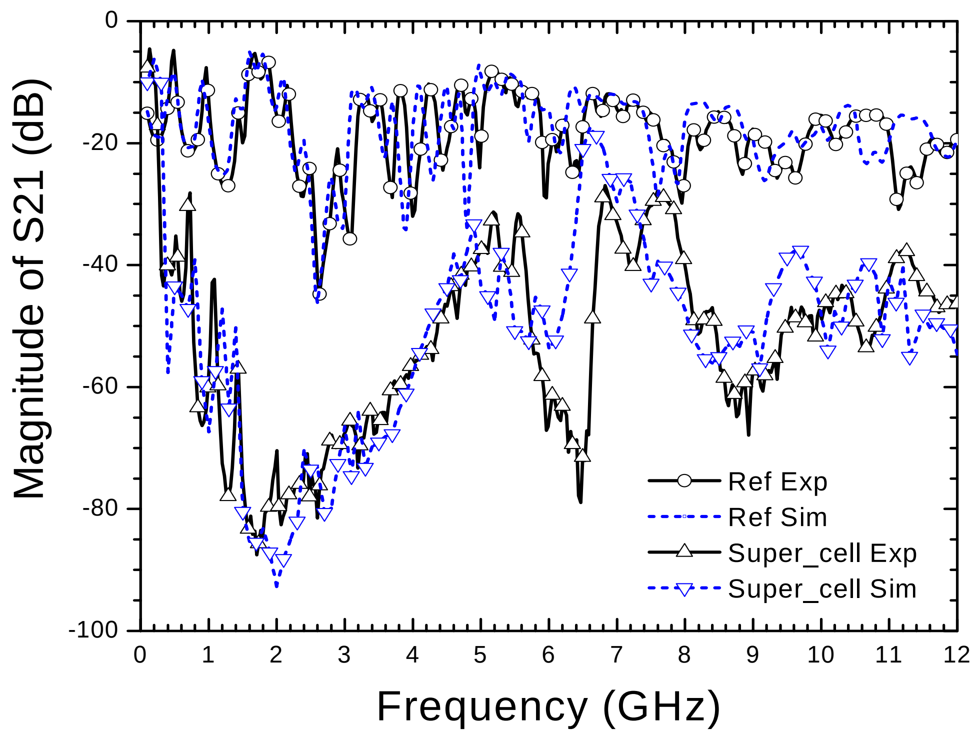

Figure 2- 14: Numerical simulation and measurement of the magnitude of S_{21} between for the novel structure proposed in this work (super cell) and for the two layer power plane (reference.)

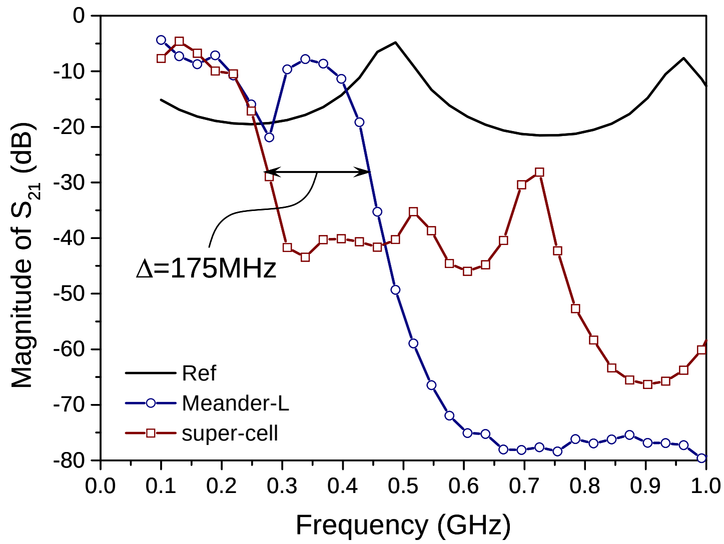

Figure 2- 15: Comparison between the lower frequency edge of the bandgap for the Meander Line and Super-cell structures.

The super cell structure was conceived based on the principle of increasing the effective inductance to lower the center frequency of the bandgap while not affecting the overall capacitance in order to maintain wide bandwidth, and on the principle of increasing the spatial periodicity in order to decrease the lower edge of the bandgap. If a single square patch of 60mm x 60mm in conjunction with the meander lines was used instead of the super cell, the lower edge of the bandgap would be close to that of the super cell structure, however, the bandgap would be much narrower. The simulation result of S-parameter for 60mm patch is shown in Figure 2-16.

Finally, we note that there is no unique choice for the topology of the connecting bridges between patches. These connecting meander and straight lines can be changed to more complex structures thus enhancing the tunability of the bandgap.

Therefore, such structure chosen here represents a generic type of structures with increased degrees of freedom to allow optimization for specific design needs.

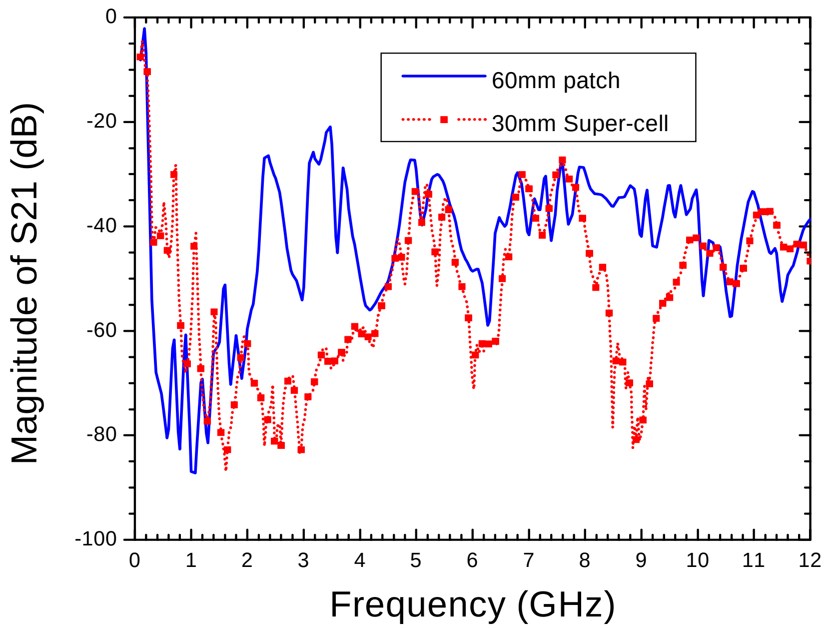

Figure 2- 16: Comparison of magnitude of S21 between 60mm Meander-L patch (solid line) and 30mm super cell patch (dotted line)

2.3.5 Miniaturization of EBG structure

The patch size of the EBG structure proposed above is 30mm x 30mm in size. In an increasing class of applications, such as computer cards, cell phone PCBs amongst others, a 30mm x 30mm patch size is impractical to use as the size of these boards spans few patches. Therefore, miniaturization of EBG patches becomes essential for noise mitigation in these important technologies.

According to the design rule discussed in section 2.3.1, if increasing the bridge inductance and capacitance, the lower edge of the stopband will be extended further. In other words if we can effectively decrease the lower edge of stopband, it will facilitate the miniaturization of the EBG structure. Another possible solution for miniaturization is employing high k thin film material in the EBG design. An example is a meander line EBG structure with dielectric constant of 100, film thickness 20um, and patch size 3mm. The simulated S parameter is show in Figure 2-17(a). The bandgap frequency range covers from 500MHz up to 6GHz above, with average attenuation below -50dB in comparison with the case without EBG structure. Also we notice the lower corner edge is critically depending on the thickness of material as shown in Figure 2-17(b). The reason is that the thinner the material, the higher the capacitance would be. Higher capacitance is highly desired in the design for noise mitigation in PCBs. In summary, it is a practical way to implement the planar EBG structure with high k thin film material in power distributed system to mitigate SSN with satisfactory stopband performance.

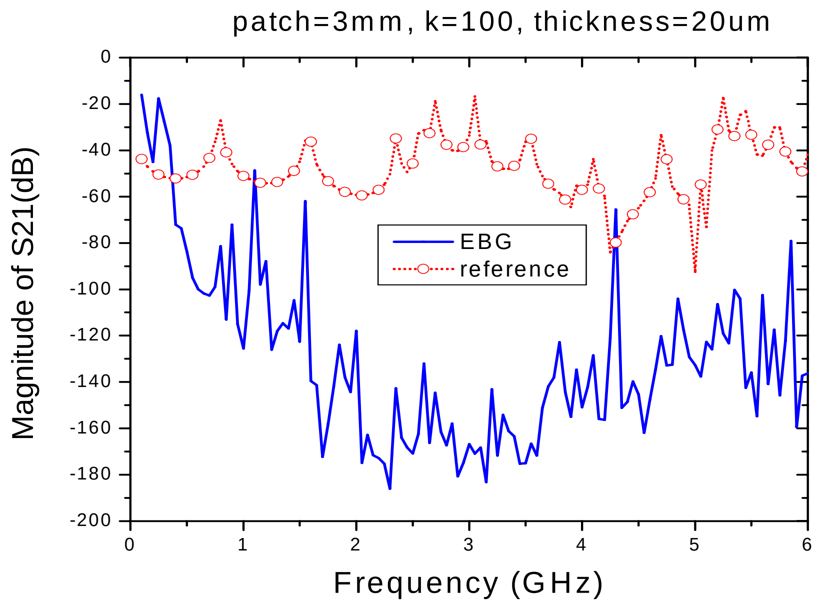

(a)

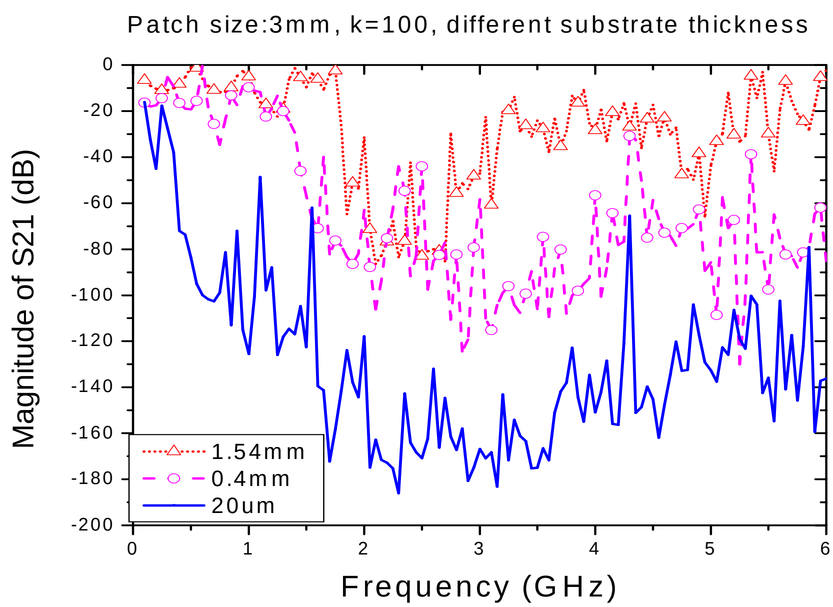

(b)

Figure 2- 17: Numerical simulation of the magnitude of S_{21} for high K thin film EBG structures (a) comparison between solid reference and EBG patterned plane (b)

comparison between different thickness: 1.54mm (dot line), 0.4mm (dash line) and 20um (solid line)

2.3.6 Summary

New types of planar EBG structures for suppression of power/ground noise in high speed PCB have been proposed. By using meander line as a dc link between patches, ultra-wideband noise suppression can be achieved. By cascading two different bridge topologies on the same board (referred to above as super-cell structure), lower periodicity can be achieved, thus decreasing the lower frequency edge of the bandgap without sacrificing the performance elsewhere. The super cell introduced here represents a complex structure that increases the overall inductance and capacitance leading to the enhancement in performance. The possibility to realize the miniaturization of EBG structure with high K material is also verified numerically. In general, using the new planar designs presented here, suppression of switching noise can be achieved over a wide bandwidth extending from 250MHz to 12GHz and beyond.

CHAPTER 3

Compact Circuit Modeling of Electromagnetic Bandgap Structures

3.1 Introduction

Although the full wave electromagnetic (EM) simulation can provide accurate and complete solutions for the studied problem, this approach, however, becomes very lengthy and memory intensive as the physical size of the structure increases. Although one could take advantage of the symmetry or of the periodicity to reduce the size of the problem to be solved in some cases as we described in chapter two, compact circuit modeling is highly required for its time efficiency.

Passive components can be modeled using lumped-elements at frequencies where the physical length of transmission line based devices and interconnects are much smaller than the wavelength. The same approach can be applied to periodic structures as long as the period is much smaller than the wavelength. In general, lumped-element equivalent circuits for one-dimensional structures can be obtained from the two port S-matrices. This concept has been applied intensively in the modeling of traditional power plane pairs [42, 43]. Compact models are combination of physical and behavioral aspects of a structure and can be obtained using numerical optimization to match measured or EM simulation-based S-parameters to those of the equivalent circuit. A very important point in developing such models is the identification of a proper model form that incorporates the physical effects of the components. Numerical optimization can then be used to determine the right parameter values by optimizing measurement or EM-simulation data against those of the equivalent circuit.

This chapter first introduces the lumped-element based circuit models for EBG structures (both meandered line structure and super cell structure). Main factors which affect the EBG bandgap features are discussed in detail. In later part of this chapter, the physical mechanism of electromagnetic bandgap structures is briefly addressed based on the Bloch-Floquet theorem. Finally, this theorem is applied on our practical EBG structures and dispersion diagram is derived.

3.2 Lumped Element Model Development

3.2.1 Model form definition

EBG structure with meander lines and its corresponding unit cell are firstly considered, and are shown in Figure 3-1. For one-dimensional wave propagation on this parallel plate transmission line cell, the equivalent circuit can be represented as in Figure 3-2 (a) and (b).

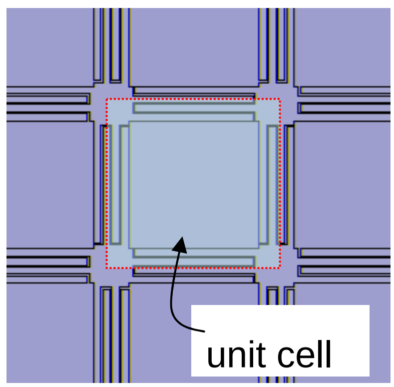

(a)

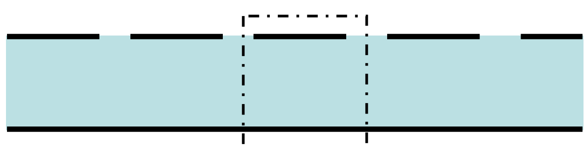

(b)

Figure 3- 1: Unit cell of meander-L EBG structure (a) top view (b) side view

Each unit section of the equivalent model consists of two parts. The first part describes the propagation characteristics between the square metal patch on the power plane and the continuous ground plane, represented by an equivalent inductance L_p and capacitance C_p. The second part characterizes the bridge effects between two adjacent unit cells, which include the bridging effect with the bridge inductance L_b, bridge capacitance C_b, and the capacitive gap coupling effect between two adjacent unit cells C_g. It is assumed that infinite unit sections are periodically cascaded, as shown in Figure 3-2 (b), to represent the EBG structure.

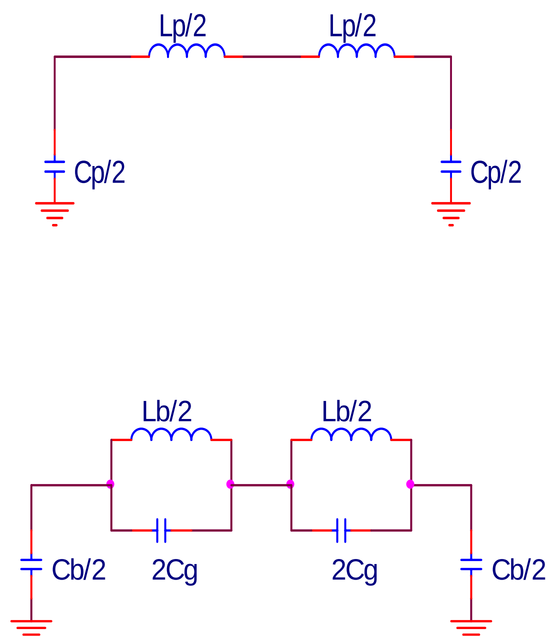

(a)

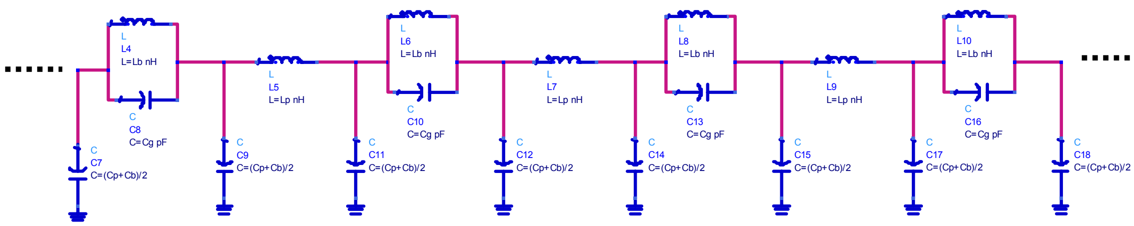

(b)

Figure 3- 2: (a) Equivalent circuit model for the unit cell of Meander-L EBG structure, where top part representing the metal patch effect, bottom part representing bridge effect (b) Circuit model for the cascaded periodic Meander-L EBG structure

3.2.2 Lumped parameters extraction

The extraction of the lumped element parameters involves the following steps: First S-parameters are generated for a structure including three periodic unit cells using electromagnetic full wave simulation. The reason to select three periods here is a compromise between high accuracy and simulation efficiency. Second initial values are assigned to the model using existing formulas of transmission line theory for microstrip line, as described in [44, 45]. The gap coupling capacitance C_g can be calculated as [13]:

$$C_{gap} = {}^{2b\varepsilon_0(1+\varepsilon_r)}\!\big/_{\pi} \cdot \cosh^{-1}\left[{}^{a}\!\big/_{2p}\right] \qquad (3.1)$$

Where b is the width of square patch, a is the distance between the centers of neighboring patches, and p is gap between neighboring patches. Finally a circuit analysis tool Agilent ADS is used to extract the values of the model components by fitting the numerically simulated S-parameters against that of the model. The validation of the lumped element model can be verified by direct comparison of the simulated and modeled S-parameter. The flow diagram of model parameter extraction is shown as Figure 3-3. Figure 3-4 shows the Agilent ADS optimization block diagram used to extract the lumped element parameters.

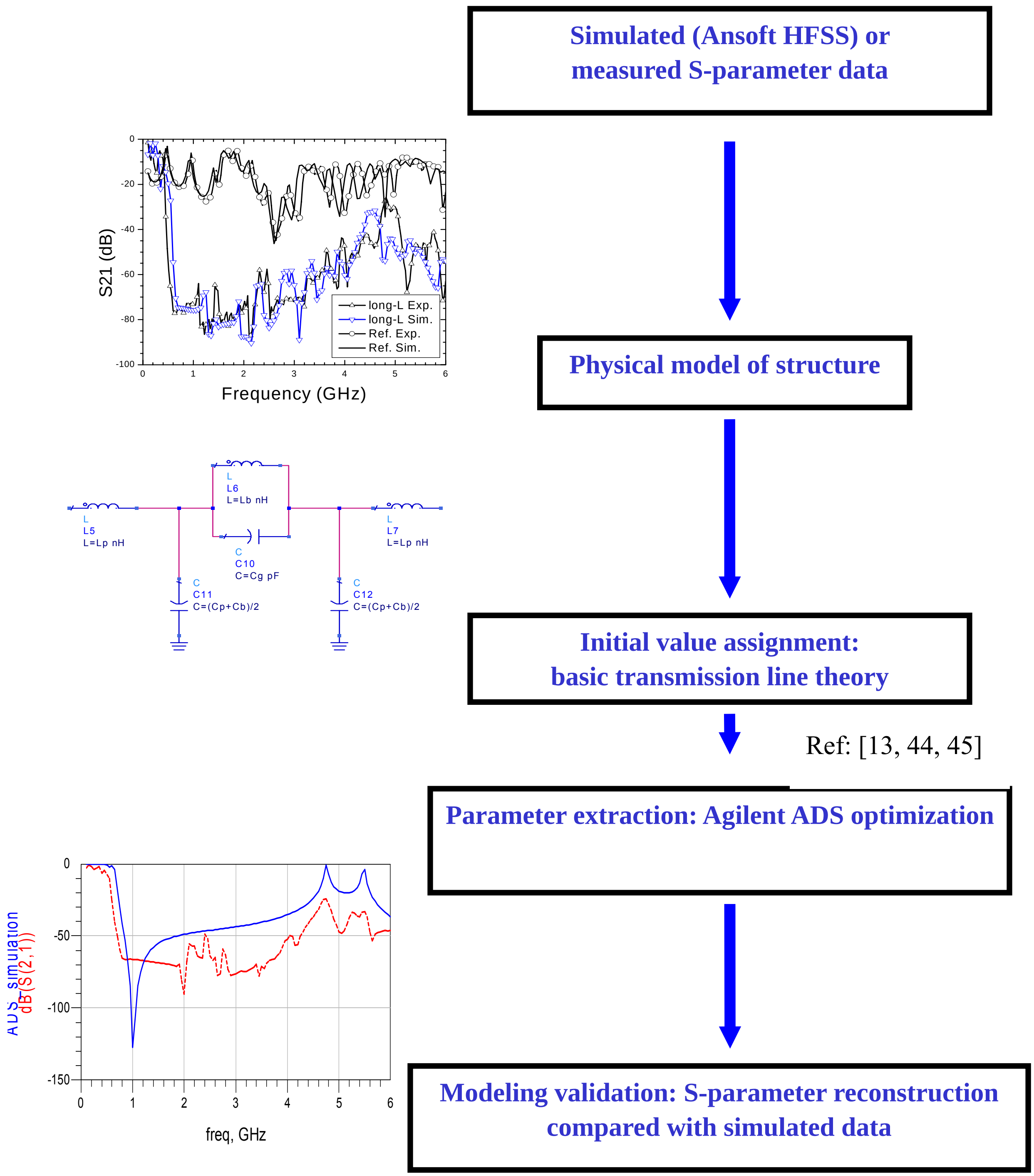

Figure 3- 3: Flow diagram of lumped elements extraction

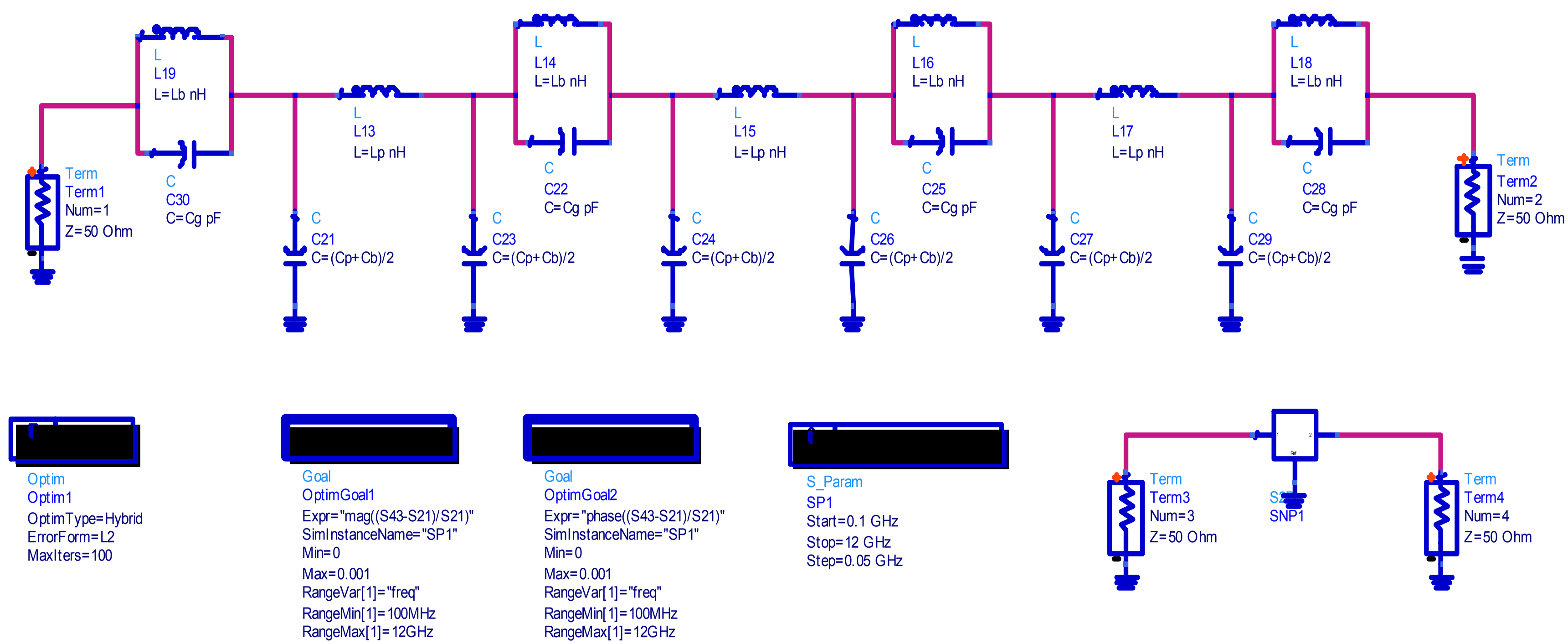

Figure 3- 4: Agilent ADS optimization block diagram

The lumped element parameters generated by this optimization are as following: L_p=0.14nH, C_p=8.82pF, L_b=14.3nH, C_b=1.2pF, and C_g=3.96pF. The validation of this circuit model can then be obtained by direct comparison of the simulated and modeled S-parameters. As shown in Figure 3-5, a reasonable agreement between full wave analysis and lumped element modeling is achieved.

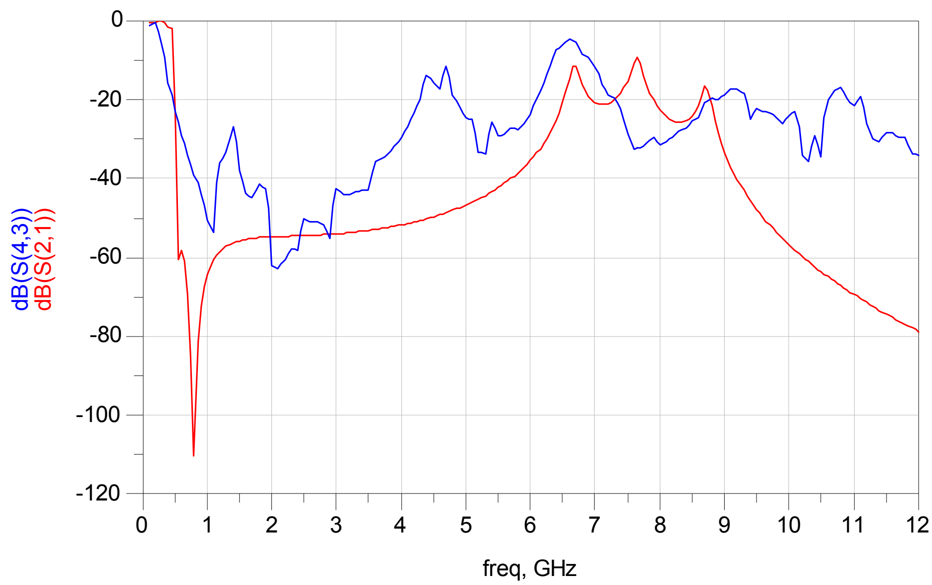

Figure 3- 5: Modeled vs. simulated S-parameters of EBG structure

solid line----ADS optimization, dotted line---- HFSS simulation

3.2.3 Meander line EBG 2D model

The equivalent circuit for two-dimensional (2D) wave propagation on the meander-L EBG structure can be modeled as of Figure 3-6.

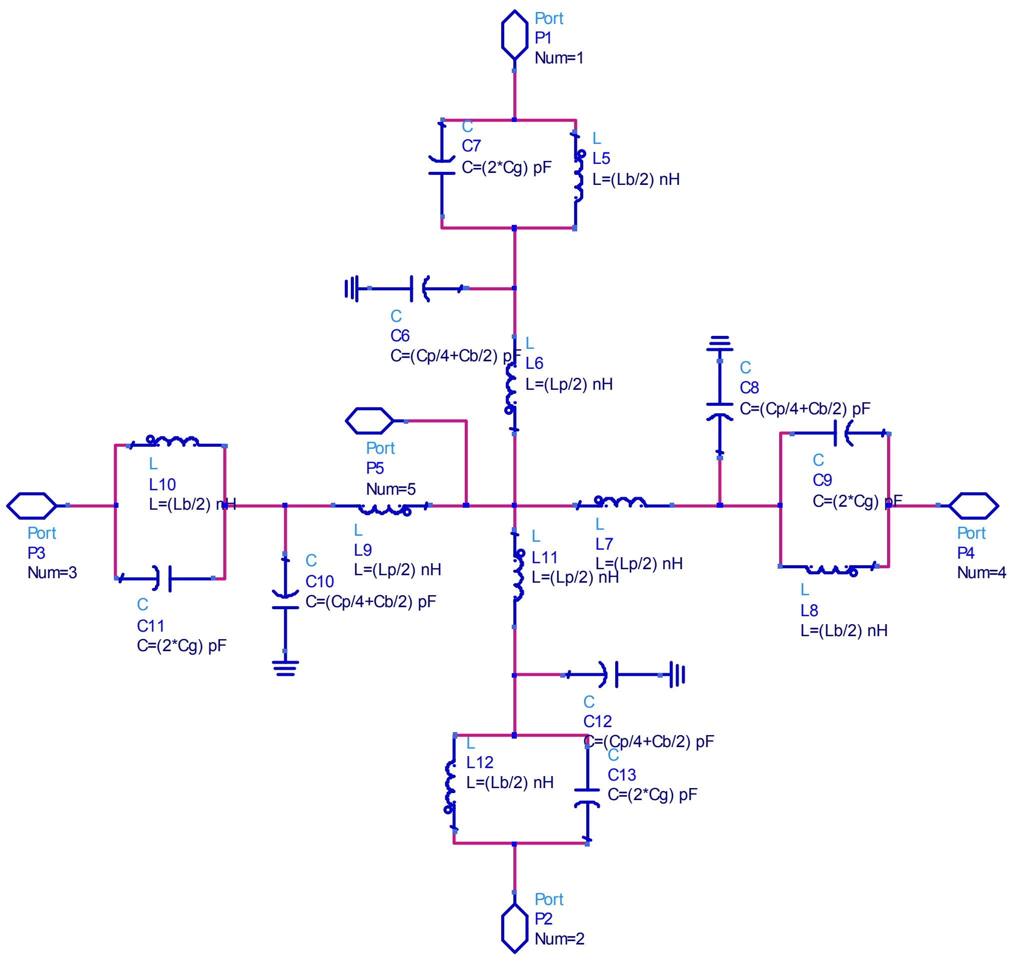

Figure 3- 6: equivalent circuit model of meander-L EBG unit cell for two-dimensional wave propagation with ports 1-5 indicated

The compact model of a full power plane can be obtained by connecting the unit cell model periodically into a two-dimensional array. Figure 3-7 is an illustration of the 2D-model of a large power plane by cascading of many cells. Each rectangle represents a multiport (5-port in this case) equivalent circuit of the unit cell.

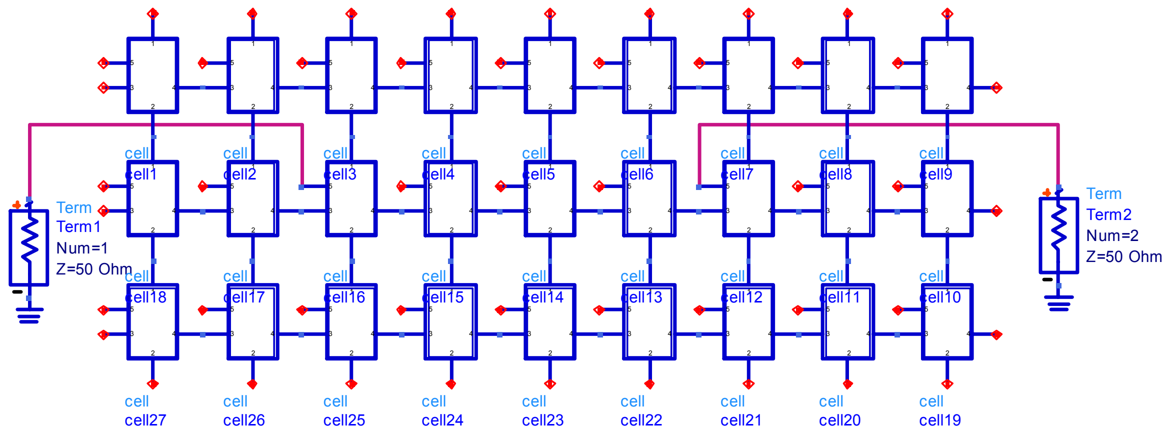

Figure 3- 7: Illustration of meander-L EBG structure based on cascading of several unit cell models

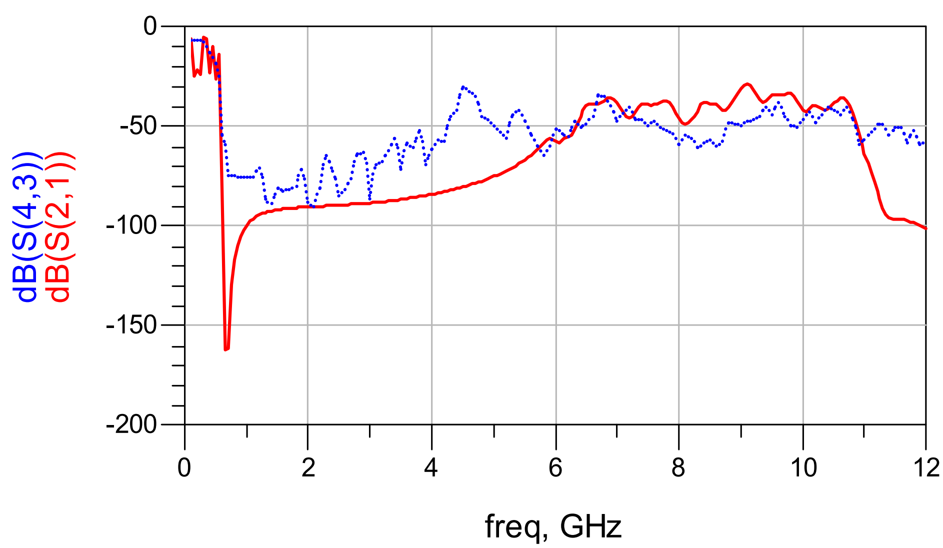

Figure 3- 8: Modeled vs. simulated S-parameters of 2D EBG structure

solid line----ADS optimization, dotted line---- HFSS simulation

Figure 3-8 shows the simulated vs. modeled S_{21} parameter of two-dimensional 3x5 array of meander line EBG structure. Good agreement is obtained over the frequency range of interest (DC to 12GHz). Also we notice the value of different lumped element will affect different features of S parameter. Next we will discuss these effects.

3.2.4 Simulation and discussion of results

Once the circuit modeling is established, it is our interest to find the system performance depends on these lumped-element parameters to give us general design instruction in order to optimize EBG bandgap capability. From the circuit model proposed in Figure 3-6, we notice the key lumped element parameters are the product of bridge inductance L_b and gap capacitance C_g, the ratio of L_b/C_g, and the product of patch inductance L_p and its corresponding capacitance C_p.

Figure 3-9 shows the frequency response of EBG power plane when the product of (L_bC_g) is varied, all other parameters are fixed. The simulation results tell us with the increase of the L_bC_g, the center frequency of stopband will be shifted downward. This center frequency is just coming from the self-resonance of the bridge, which form the high impedance surface (HIS) to block the propagation of EM wave. So if we can effectively increase the L_b (that is the reason why we adopt the meander line structure), and C_g (applying high k material), the center frequency of stopband will be shifted downward in frequency further. A significant increase of this parameter is desirable to achieve noise mitigation in the hundreds MHz range.

Figure 3-10 shows the bandwidth of stopband vs. ratio of bridge inductance L_b to its corresponding gap capacitance C_g. If the ratio of L_b/C_g increases, the bandwidth of stopband will also increases. The reason is the characteristic impedance of the EBG surface can be semi-qualitatively expressed as $Z_0 \propto \sqrt{L_b / C_g}$. The total bandwidth is approximately equal to the characteristic impedance of the surface divided by the impedance of free space. The readers can refer to [13] for the detailed analysis. So the increase of the bridge inductance is an effective way to achieve both the wider bandwidth and the lower corner frequency.

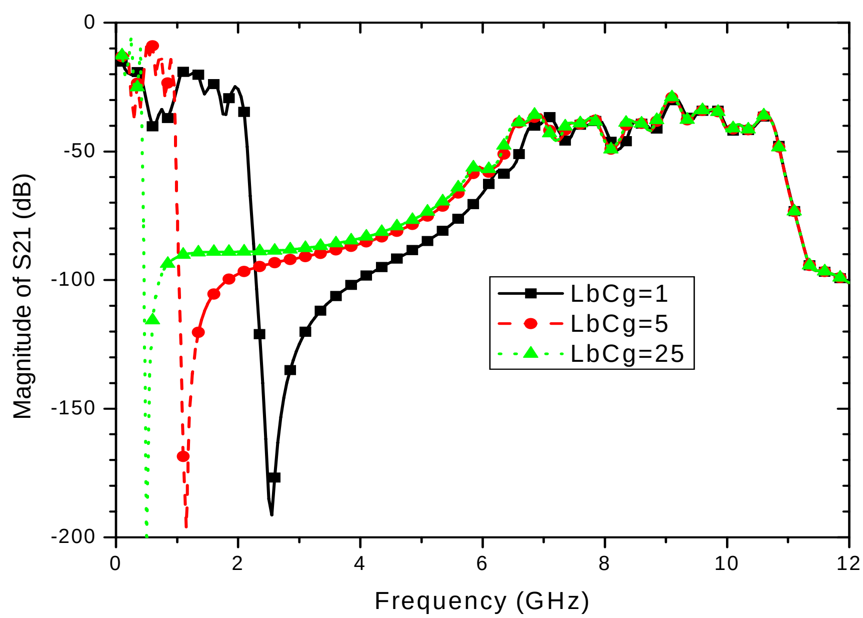

Figure 3- 9: Dependence of the bandgap center frequency on the product of bridge inductance L_b and gap capacitance C_g.

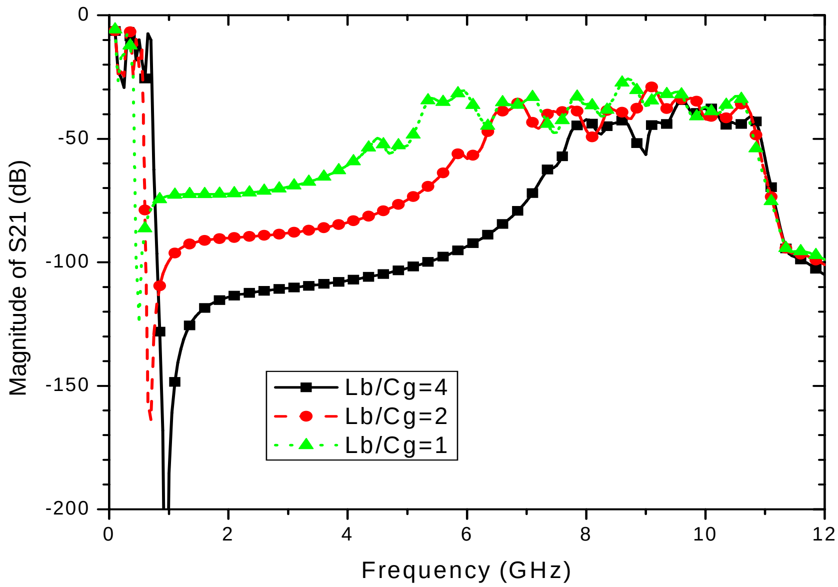

Figure 3- 10: Dependence of the bandwidth on the ratio of bridge parameters L_b/C_g.

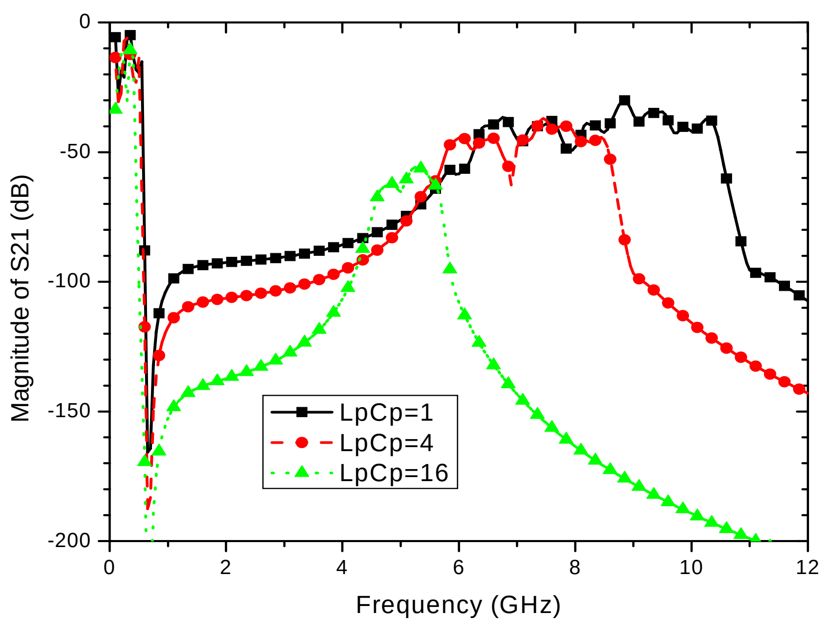

Figure 3- 11: Dependence of the upper corner frequency of stopband on the product of patch parameters L_pC_p.

Another noticeable feature is that the variation of the product of patch capacitance and patch inductance will have a direct impact on the upper corner frequency of stopband as shown in Figure 3-11. Further analyzing model diagram of Figure 3-6, we notice at the patch resonance frequency $f_{patch} \propto 1/\sqrt{L_p C_p}$, the EM wave will be reflected back and forth, which results in strong transmission of wave.

In summary, the EBG structure reflection/transmission performance significantly depends on the physical geometry of the patch. The analysis above gives us a general design rules for planar EBG structure in order to achieve the best noise mitigation effects.

3.2.5 Super cell EBG model

The unit cell for the super cell structure is shown in Figure 3-12.

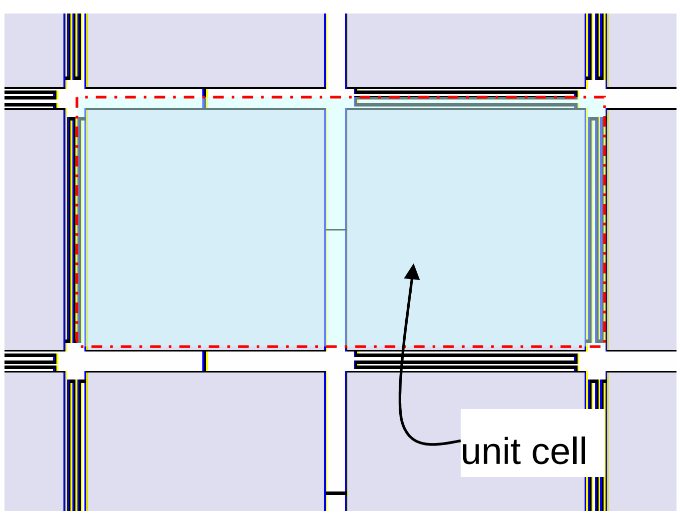

Figure 3- 12: unit cell for circuit simulation of super cell EBG structure

The circuit model of unit cell is decomposed of three parts: one for the patch (a), the other two represents different bridges (b) and (c) as of Figure 3-13.

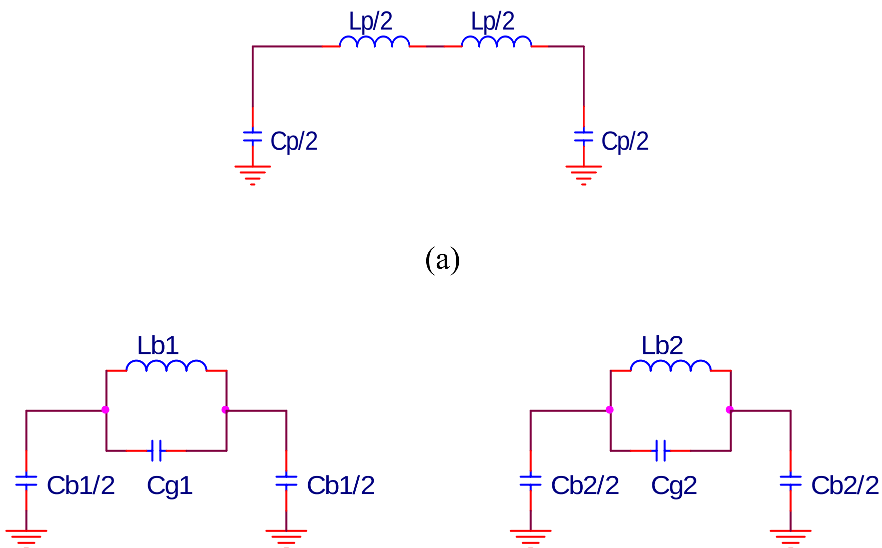

(a)

(b) (c)

Figure 3- 13: Decomposition of unit cell for super cell EBG structure (a) metallic patch (b) meander-L bridge (c) short-L bridge

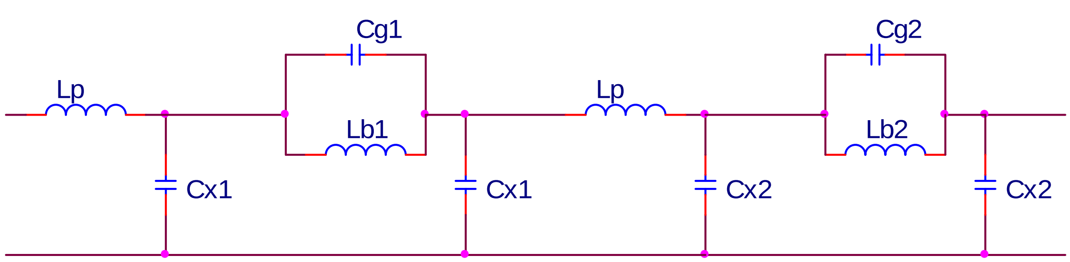

Figure 3- 14: The equivalent circuit for unit cell of super cell EBG structure

The equivalent circuit for unit cell is modeled as Figure 3-14.

where: $C_{x1}=(C_p+C_{b1})/2$, $C_{x2}=(C_p+C_{b2})/2$

Following the same scheme as described in section 3.2.2, the equivalent lumped element for the super cell structure is:

L_p=0.25nH, C_p=5.2pF, L_{b1}=11.3nH, L_{b2}=0.15nH, $C_{g1}=C_{g2}$=3.96pF, C_{b1}=1.2pF, and C_{b2}=0.9pF. When put these numbers into 2D circuit model, the final S_{21} parameter for 3x5 cells super cell EBG structure is shown in Figure 3-15.

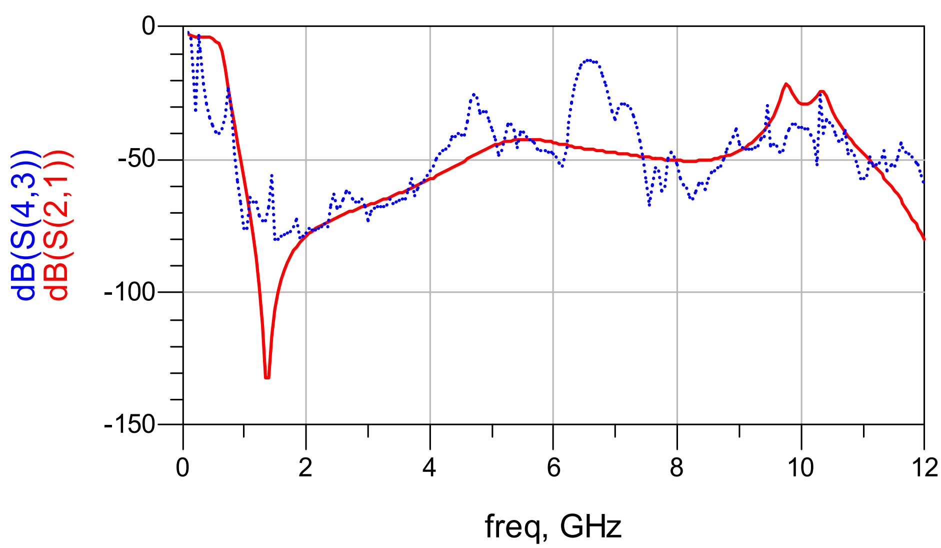

Figure 3- 15: Modeled vs. simulated S-parameters of super cell EBG structure

solid line----ADS optimization, dotted line---- HFSS simulation

3.3 Bloch-Floquet Theorem

Floquet first studied the problem of differential equations with periodic coefficients from the mathematical perspective [46]. Bloch successfully applied the periodic structure theory to study electronic wave in a periodic crystal lattice [47]. Because particle wave function in the periodic potential of crystal lattice can be described by Schrodinger equation:

$$-\frac{\hbar^2}{2m}\frac{d^2\psi}{dx^2}+V(x)\psi = E\psi \tag{3.2}$$

Where *V(x)* represents the potential of the crystal lattice that has the periodicity of the lattice d, i.e.,

$$V(x+d)=V(x) \tag{3.3}$$

Bloch found the wave function of the particle in periodic lattice potential can be expressed as the wave function of a free particle modulated by a periodic function which has the same periodicity of the lattice potential, which is called Bloch wave:

$$\psi(x)=e^{ikx}u(x) \tag{3.4}$$

where

$$u(x+d)=u(x) \tag{3.5}$$

The wave function can also be written in another form:

$$\psi(x+d)=e^{ikd}\psi(x) \tag{3.6}$$

This means that any wave function $\psi(x)$, that is a solution to the Schrodinger equation of the problem, differs only by a phase factor e^{ikd} between equivalent positions in the lattice.

Recently, there has been a great interest in periodic dielectric structures (photonic crystal, or photonic bandgap, PBG) for electromagnetic waves propagation [48-50]. Band gap behavior is achieved by periodic variation in the dielectric constant of the substrate. According to Maxwell's equations, the EM wave in periodic dielectric can be written as follows:

$$\nabla^2 \vec{E} + \frac{\mu\varepsilon(r)\omega^2}{c^2}\vec{E} = 0 \tag{3.7}$$

$$\nabla^2 \vec{H} + \frac{\mu\varepsilon(r)\omega^2}{c^2}\vec{H} = 0 \tag{3.8}$$

where:

$$\varepsilon(r+d) = \varepsilon(r) \tag{3.9}$$

Similar as the derivation of electron wave in solid crystal, EM wave in the periodically arranged dielectric substrate will also looks like a Bloch wave. The constructive and destructive interference of electromagnetic waves results in transmission and reflection bands in frequency.

While for the EBG structure considered in this work, the periodicity is not constructed by inserting periodically distributed dielectric material in the substrate, but rather is achieved by arranging the metallic pattern in a periodic fashion. Actually the effect of periodically arranged pattern is just the same as that of periodically arranged material because the different geometry of microstrip line will result in different effective dielectric constant even in the same substrate. The wave propagation in the EBG structure can be conceptually thought of as that in the PBG. So the EM field in the EBG structure also obeys the equations of (3.7)-(3.9). If considering the wave propagation in the infinite line as being composed of cascaded identical two port networks as shown in figure 3-16, we can relate the voltage and current at the (n+1)th terminal to be equal to the voltage and current at the nth terminal, apart from the phase difference due to the finite propagation time [51]. Thus we can write:

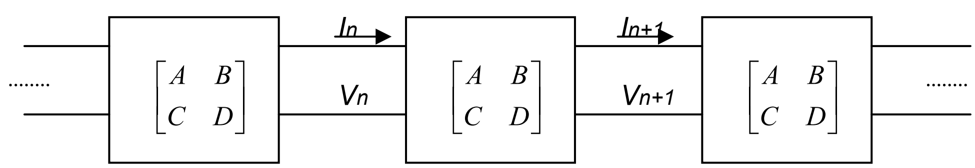

Figure 3- 16: transmission line with infinite periodic structures

$$V_{n+1} = e^{j\beta d} V_n \tag{3.10}$$

$$I_{n+1} = e^{j\beta d} I_n \tag{3.11}$$

where β is the propagation constant for the periodic structure and d is the periodicity. It is important to note that the voltage and current waves defined in the equation are meaningful only when measured at the terminals of unit cells, and do not apply to voltages and currents that may exist at points within the unit cell. Next we apply this Bloch-Floquet theorem to derive the dispersion behavior of EBG structures.

3.4 Dispersion Diagram

3.4.1 Meander-L EBG structure

The approach used for the derivation of the dispersion relationship is analogous to that of the phonon dispersion derivation in solids. The electrical filter is analogous to the one dimensional diatomic lattice, the circuit schematics of meander-L EBG structure is shown in Figure 3-17, where $C_x=(C_p+C_b)/2$. For the lumped parameters definition please refers to section 3.2.1.

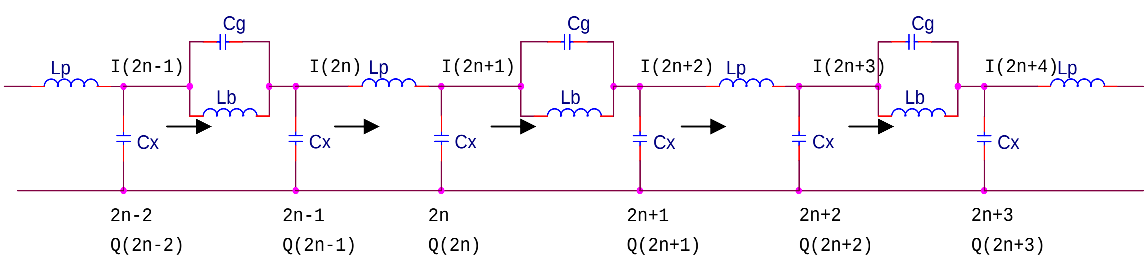

Figure 3- 17: equivalent circuit model for periodic meander-L EBG structure

The current on the first part (L_p) and the second part (sum of the current on C_g and L_b) of section n are denoted as i_{2n} and i_{2n+1}. The electrical charges on C_p and C_b of section n are denoted as Q_{2n} and Q_{2n+1}. The relations between the currents and node charges can be derived as:

$$i_{2n} - i_{2n+1} = \frac{dQ_{2n}}{dt} \tag{3.12}$$

$$i_{2n+1} - i_{2n+2} = \frac{dQ_{2n+1}}{dt} \tag{3.13}$$

$$\frac{L_b}{1-\omega^2 L_b C_g}\frac{di_{2n+1}}{dt} = \frac{Q_{2n}}{C_x} - \frac{Q_{2n+1}}{C_x} \tag{3.14}$$

$$L_p \frac{di_{2n+1}}{dt} = \frac{Q_{2n-1}}{C_x} - \frac{Q_{2n}}{C_x} \tag{3.15}$$

Differentiating (3.14) and (3.15) with time, and combining with equations of (3.12) and (3.13), yields

$$\frac{L_b}{1-\omega^2 L_b C_g}\frac{d^2 i_{2n+1}}{dt^2} = \frac{i_{2n}}{C_x} - \frac{2}{C_x} i_{2n+1} + \frac{i_{2n+2}}{C_x} \tag{3.16}$$

$$L_p \frac{d^2 i_{2n}}{dt^2} = \frac{i_{2n-1}}{C_x} - \frac{2}{C_x} i_{2n} + \frac{i_{2n+1}}{C_x} \tag{3.17}$$

Considering periodicity of this EBG structure, applying Bloch-Floquet theorem as we discussed in section 3.3, the wave solutions for the current i_{2n} (2n+2, 2n+4…), and i_{2n+1} (2n+3, 2n+5…) can be written as:

$$i_{2n} = A_0 e^{j(\omega t - 2nk)} \qquad \text{;for even terminal: 2n, 2n+2 ...} \tag{3.18}$$

$$i_{2n+1} = A_1 e^{j[\omega t - (2n+1)k]} \qquad \text{;for odd terminal: 2n+1, 2n+3 ...} \tag{3.19}$$

where $k = {}^{\pi d}\!/_{\lambda}$

When substituting (3.18) and (3.19) into (3.16) and (3.17), for non-trivial solutions for A_0 and A_1, the determinant (3.20) must equal to zero.

$$\begin{vmatrix} \frac{1}{C_x} 2\cos(k) & \frac{\omega^2 L_b}{1-\omega^2 L_b C_g} - \frac{2}{C_x} \\ \omega^2 L_p - \frac{2}{C_x} & \frac{1}{C_x} 2\cos(k) \end{vmatrix} = 0 \tag{3.20}$$

Next, we use the lumped-element parameters obtained from section 3.2.2 leading to the dispersion relation between ω and k shown in Figure 3-18. In this diagram, the bandgap is represented by the frequency range in which there is no propagating mode for value of k with imaginary part. The bandwidth of stopband predicted by this 1-D circuit model is 4.7GHz, ranging from 0.5GHz to 5.2GHz. Furthermore, a stopband is visible at 8.5GHz and beyond. Compared to the numerical simulation result (using full wave analysis as in Figure 2-12, the first bandgap appears between 460MHz to 5GHz), a good agreement is seen from the dispersion diagram, especially at lower frequencies. At the higher frequency, the lumped circuit model is not precise due to the physical length of lumped components is comparable with the electrical wavelength.

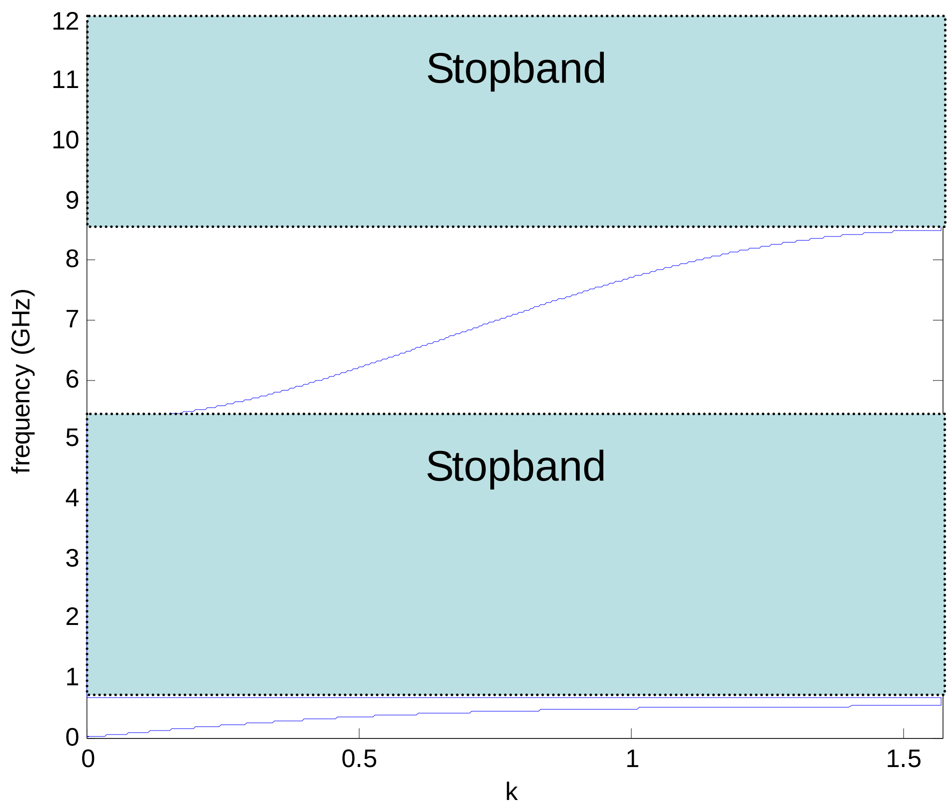

Figure 3- 18: Dispersion diagram for Meander-L EBG structure obtained using the Bloch-Floquet Analysis using lumped circuit elements.
The gray area shows the stopband region.

3.4.2 Super cell EBG structure

The difference between the super cell EBG structure and meandered-L EBG structure is that super cell structure has two different bridges represented by different sets of lumped element parameters. Assuming that the meandered L bridge is characterized by equivalent inductance L_{b1}, bridge capacitance C_{b1}, and gate capacitance C_{g1}. Short L bridge is then described with parameters L_{b2}, C_{b2} and C_{g2}. Actually we can assume $C_{g1}=C_{g2}=C_g$. Figure 3-19 shows circuit model for the periodic super cell EBG structure:

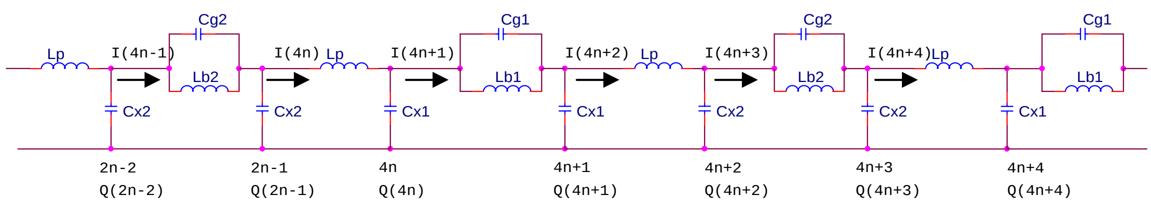

Figure 3- 19: Equivalent circuit model for the periodic super cell EBG structure

The derivation process is similar as the meander L structure described above:

$$i_{4n} - i_{4n+1} = \frac{dQ_{4n}}{dt} \tag{3.21}$$

$$i_{4n+1} - i_{4n+2} = \frac{dQ_{4n+1}}{dt} \tag{3.22}$$

$$i_{4n+2} - i_{4n+3} = \frac{dQ_{4n+2}}{dt} \tag{3.23}$$

$$i_{4n+3} - i_{4n+4} = \frac{dQ_{4n+3}}{dt} \tag{3.24}$$

Differentiating (3.23) and (3.24) with time, and combining with equations of (3.21) and (3.22), yields:

$$L_p \frac{d^2 i_{4n}}{dt^2} = \frac{1}{C_{x2}}(i_{4n-1} - i_{4n}) - \frac{1}{C_{x1}}(i_{4n} - i_{4n+1}) \tag{3.25}$$

$$\frac{L_{b1}}{1-\omega^2 L_{b1} C_{g1}} \frac{d^2 i_{4n+1}}{dt^2} = \frac{1}{C_{x1}}(i_{4n} - 2i_{4n+1} + i_{4n+2}) \tag{3.26}$$

$$L_p \frac{d^2 i_{4n+2}}{dt^2} = \frac{1}{C_{x1}}(i_{4n+1} - i_{4n+2}) - \frac{1}{C_{x2}}(i_{4n+2} - i_{4n+3}) \tag{3.27}$$

$$\frac{L_{b2}}{1-\omega^2 L_{b2} C_{g2}} \frac{d^2 i_{4n+3}}{dt^2} = \frac{1}{C_{x2}}(i_{4n+2} - 2i_{4n+3} + i_{4n+4}) \tag{3.28}$$

Applied Bloch-Floquet theorem,

$$i_{4n} = A_0 e^{j(\omega t - 4nk)} \tag{3.29}$$

$$i_{4n+1} = A_1 e^{j(\omega t - (4n+1)k)} \tag{3.30}$$

$$i_{4n+2} = A_2 e^{j(\omega t - (4n+2)k)} \tag{3.31}$$

$$i_{4n+3} = A_3 e^{j(\omega t - (4n+3)k)} \tag{3.32}$$

where $k = \pi d / \lambda$

When substituting equations of (3.29)-(3.32) into (3.25)-(3.28), for the non-trivial solutions for A_0 to A_4, the determinant (3.33) need to be equal to zero.

$$\begin{vmatrix} \omega^2 L_p - (\frac{1}{C_{x1}} + \frac{1}{C_{x2}}) & \frac{1}{C_{x1}} e^{-jk} & 0 & \frac{1}{C_{x2}} e^{jk} \\ \frac{1}{C_{x1}} e^{jk} & \frac{\omega^2 L_{b1}}{1-\omega^2 L_{b1} C_{g1}} - \frac{2}{C_{x1}} & \frac{1}{C_{x1}} e^{-jk} & 0 \\ 0 & \frac{1}{C_{x1}} e^{jk} & \omega^2 L_p - (\frac{1}{C_{x1}} + \frac{1}{C_{x2}}) & \frac{1}{C_{x2}} e^{-jk} \\ \frac{1}{C_{x2}} e^{-jk} & 0 & \frac{1}{C_{x2}} e^{jk} & \frac{\omega^2 L_{b2}}{1-\omega^2 L_{b2} C_{g2}} - \frac{2}{C_{x1}} \end{vmatrix} = 0 \qquad (3.33)$$

Following similar procedure to that used earlier, the dispersion diagram for the super cell structure is derived and is is shown in Figure 3-20, the bandgap is represented by the frequency range in which there is no propagating mode. We observe that the stopbands for the super cell EBG structure extend from 0.5GHz to 4.7GHz, from 5.5GHz to 8.8GHz, and above 10GHz. The results show the super cell structure has multi-stopband feature, the same as the numerical simulation as shown in Figure 2-14. These sub-stopbands are due to the different resonances from the different bridges, and the interactions between these resonance modes.

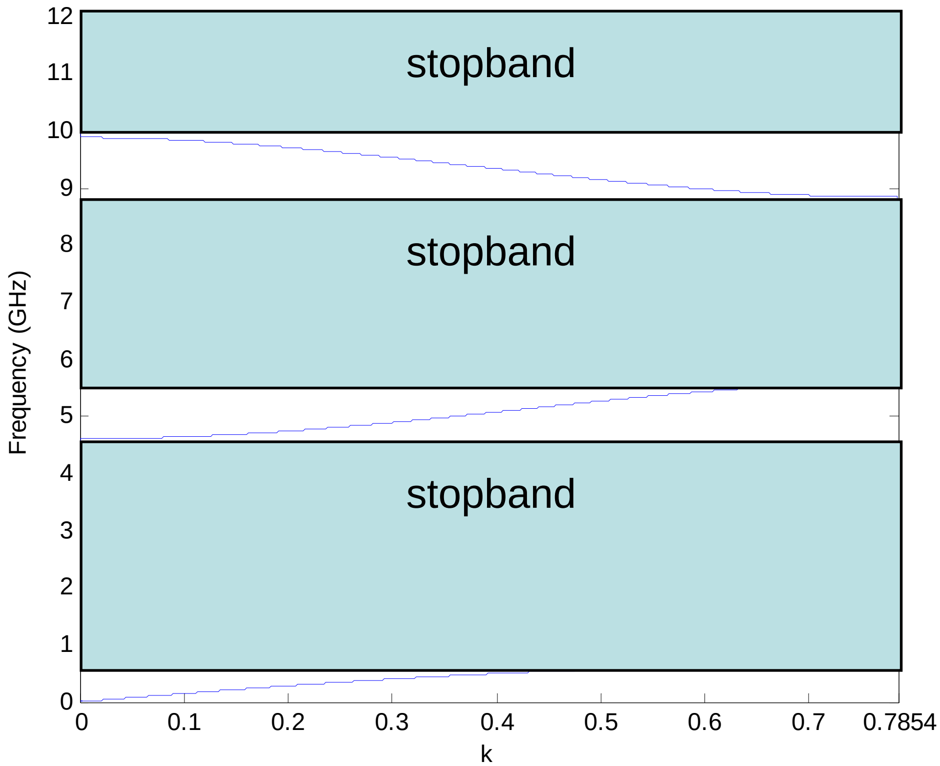

Figure 3- 20: Dispersion diagram for super cell EBG structure, the gray area shows the stopband region.

CHAPTER 4

Leakage Radiation and EMI Reduction of Electromagnetic Bandgap Structures

4.1 Introduction

The primary goal for the EMI/EMC engineer is to ensure proper operation and performance of a product when used within an intended electromagnetic environment. Also, the engineer needs to insure that the product is electromagnetically compatible with other circuit or system.

The proliferation of high-speed electronic device and communication equipment is leading to an increasingly hostile electromagnetic environment. With the continuous decrease in power supply and threshold voltage levels, CMOS based digital circuits become more vulnerable to external electromagnetic interference (EMI). At the same time, the increase in clock and bus speed increases the potential of the circuit to radiate, thus compromising its compatibility potential and also increasing its security vulnerability.

EMI is a complex mechanism that takes place at different levels including the chassis, board, component, and finally, the device level. Radiation sources typically include trace coupling, cables attached to the boards, components such as chip packages and heat sinks, power busses and practically anything that can provide a low impedance current path.

EMI can be transmitted through two basic modes. The one is conducted emission, where the component of RF energy is transmitted through a medium as a propagating wave. The other is radiated emission, where component of RF energy is transmitted through a medium as an electromagnetic field.

In chapter two, we emphasis on the first type of EMI radiation mode, where we introduce EBG structures to block the wave propagation along the parallel plate waveguide. In this chapter, we will focus on the problem of radiation through the perforated planar EBG structure and from edges of boards, i.e., the second type of EMI radiation mode. Our objective is to gain the comprehensive knowledge of the field distribution through this imperfect plane and develop techniques to reduce the radiation without affecting the performance of neighboring products.

4.2 Leakage Radiation through EBG Patterned PCBs

Electromagnetic penetration through perforated metal surfaces needs to be analyzed in a detailed way in order to fulfill the compliance of the strict electromagnetic compatibility (EMC) regulations. Previous studies [52, 53] show the radiation from solid power planes comes from a time-varying electric field at the board edges similar to the way a patch antenna radiates. If the signal is fed at one port and received at another port, part of the signal radiates at the edge of the board and it never reaches at any of the ports. The radiation loss is characterized by the parameter: $1-|S_{11}|^2-|S_{21}|^2$. This is different from a closed lossless system, in which the total combination of reflection coefficient and transmission coefficient equals to unity. For the perforated planar EBG structures described above, in addition to the radiation at the edges of board, there are gaps between the cells, which may cause extra radiation leakage, especially at the frequency where the patches resonate. In sharp contrast to the three- or multi-layer EBG structures with solid power plane, this extra radiation from these perforated boards can potentially be sufficient to create incompatibility with either circuit functionality, or simply be high enough to violate regulatory radiation standards.

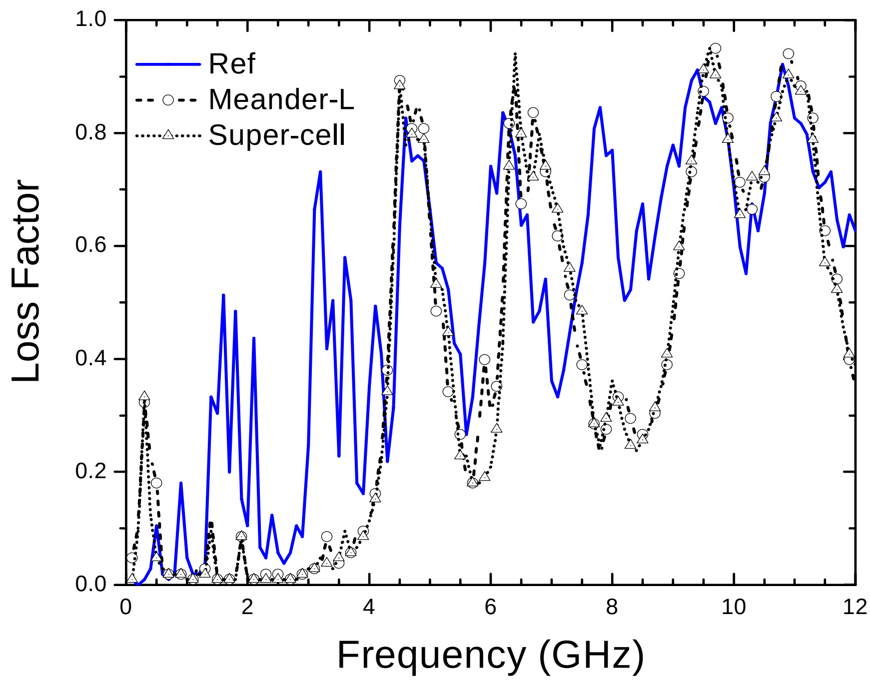

Figure 4- 1: Radiation loss for different structures

Here the calculated loss factor: $1-|S_{11}|^2-|S_{21}|^2$ is examined for EBG-based power planes and compared to the case with solid power plane. The results shown in Figure 4-1 demonstrate that the radiation peaks at 480MHz, 960MHz…etc., which arise from the cavity modes of the 90mm x 150mm reference board, are significantly suppressed for the EBG-patterned structures. The strong radiation peaks at 4.7GHz, 6.6GHz, 9.4GHz, and 10.6GHz for the EBG-patterned power planes are due to the patch resonance, which can be further confirmed from the input impedance (self impedance of excitation port) data. As we discussed previously, the solid power/ground plane can be modeled as an RLC network, the impedance matrix of one port can be described as a resonator circuit model which consists of inductor, capacitor and resistor in parallel [54, 55]. It has been theoretically proved the resonator circuits for every odd mode are removed if the port is located at the center of the board. This is also confirmed in our simulation result shown in Figure 4-2 where the first high impedance peak corresponds to the $f_{20,02}$ modes of the 30mm x 30mm patch at 4.7GHz followed by even numbered modes f_{22}, f_{40}. Notice that odd numbered modes do not appear because the feed port consists of a center-fed patch. When the patch is fed off center, odd numbered modes appear consistent with cavity resonance behavior shown in Figure 4-3, where the fundamental mode begins at 2.3GHz, ie f_{10} mode. Because of this, the via should be designed through the center of patch in order to avoid the resonance of odd modes. Therefore, the radiation energy would be decreased significantly.

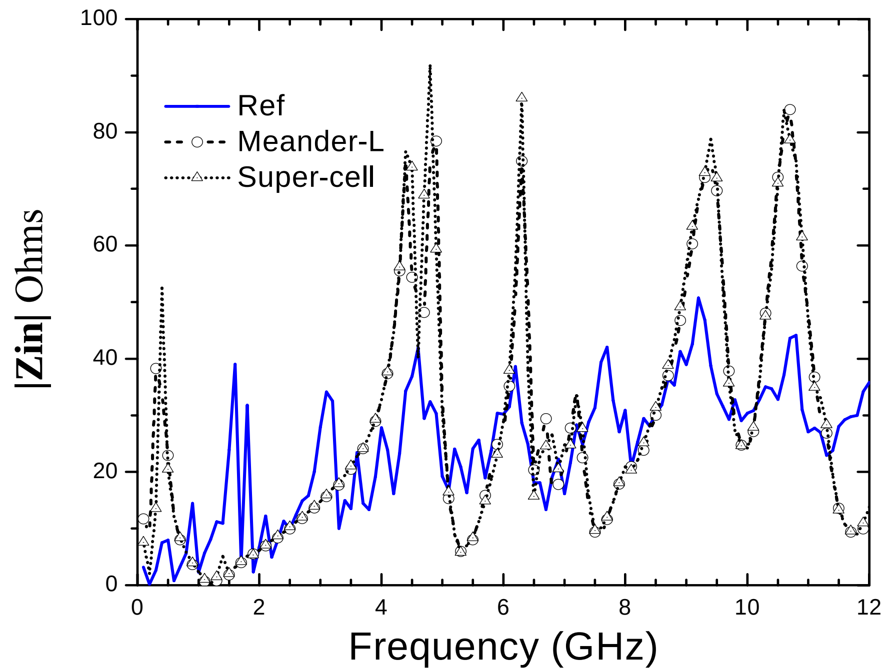

Figure 4- 2: Simulated port input impedance for different structures

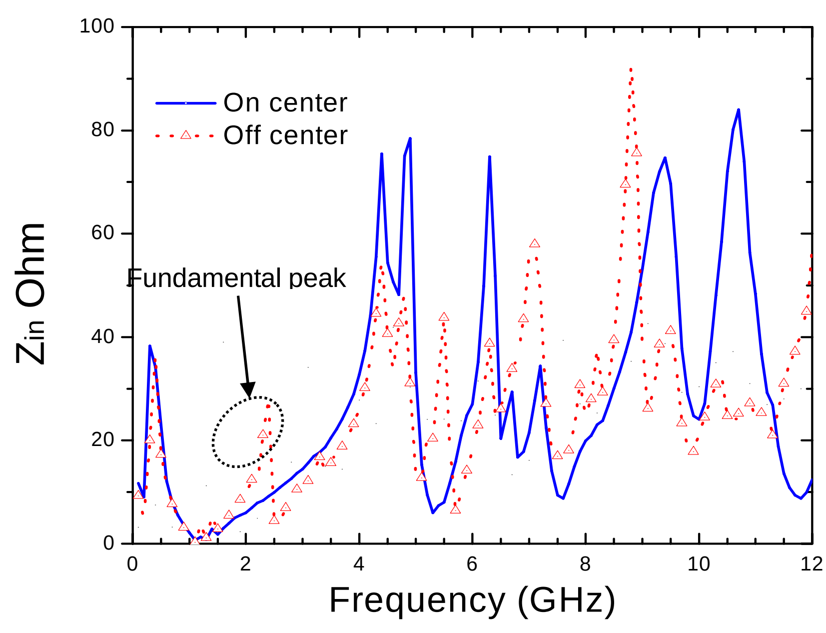

Figure 4- 3: Simulated port input impedance for on-center and off-center excitation

However, the radiation loss from these impedance peaks does not show much increase when comparison is made to the case with solid reference plane. This is due to the resonance modes overlap between those of the reference plane and of the single patch. Overall, the data shows the total radiated power from EBG patterned PCB is diminished, especially at the lower frequency region (below the fundamental resonance of patch at 4.7GHz) in comparison to the reference plane.

We emphasize that the measure of the radiation loss used here, i.e., the quantity $1-|S_{11}|^2-|S_{21}|^2$, is only indicative of the fact that the electromagnetic energy prevented from propagating between the two ports is either stopped at the source (the transmitting port, due to a change in its input impedance as a result of using the EBG patches) or leaks through other channels. A more detailed analysis of the power leakage is given below.

4.3 Near Field Characterization

In order to obtain a better understanding of the shielding behavior of perforated power planes, the near field of these proposed planar EBG structures is studied. In all the cases studied here, comparison is always made to the fields arising from a two-layer solid power plane.

The analysis here is carried out by using a monopole antenna connected to a power meter to monitor the field along a test line positioned 1cm above the EBG-patterned plane and aligned along the open slot extending from the left to the right edge (represented by normalized distance) as shown in Figure 4-4 (a),(b). An RF signal of 10 dBm is launched into the power plane at the feed port shown in Figure 4-4(a). The field intensity as a function of normalized distance is shown in Figure 4-5 (a)-(c) for different frequencies. The frequencies selected here are 480MHz (fundamental resonance frequency for reference board), 2.6GHz (within the stopband of the EBG structure), and 4.7GHz (patch fundamental resonant frequency).

In comparison to the solid reference plane, at the resonance frequency of the PCB at 480MHz, the data shows that the near field is significantly suppressed by using the EBG structures. Notice that while the 480MHz is at the bottom edge of the stopband, it is a resonant mode for the solid plane (reference). The reason for the reduced near field is attributed to the perforated top plane which prevents the "dipole-like" behavior that is characteristic of solid planes (or patch antennas.) Therefore, the planar EBG structure has the added advantage of reducing the dominant resonance of the board.

At the 2.6GHz and 4.7GHz frequencies, the field leakage is stronger when using the planar EBG structure in comparison to the solid plates PCB. In fact, we observe the field to be highly concentrated around the feeding port. This is expected at these frequencies as the EBG blocks the transmission of energy between the ports and one expects a high-reflection at the transmitting port and hence the higher concentration of the field there. Furthermore, we observe that the field intensity gradually dies down after traversing several EBG patches. This attenuation is mainly attributed to the EBG structure surface current mitigation mechanism.

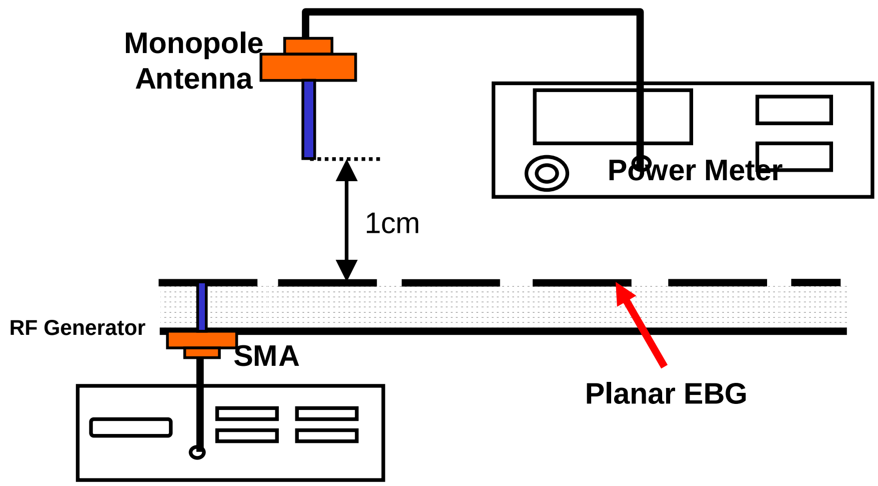

(a)

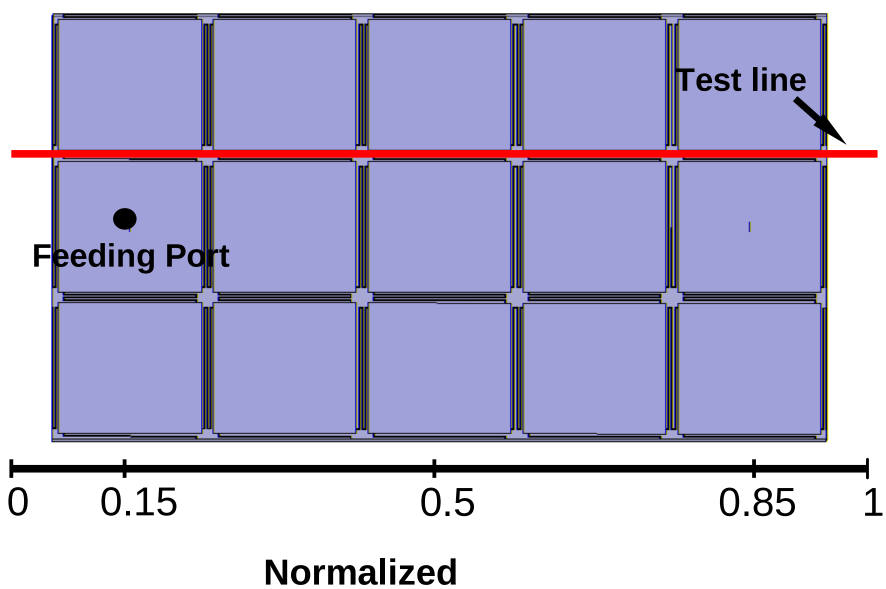

(b)

Figure 4- 4: (a) Near-field measurement setup

(b) Top view of test board, showing the test line and the normalized distance

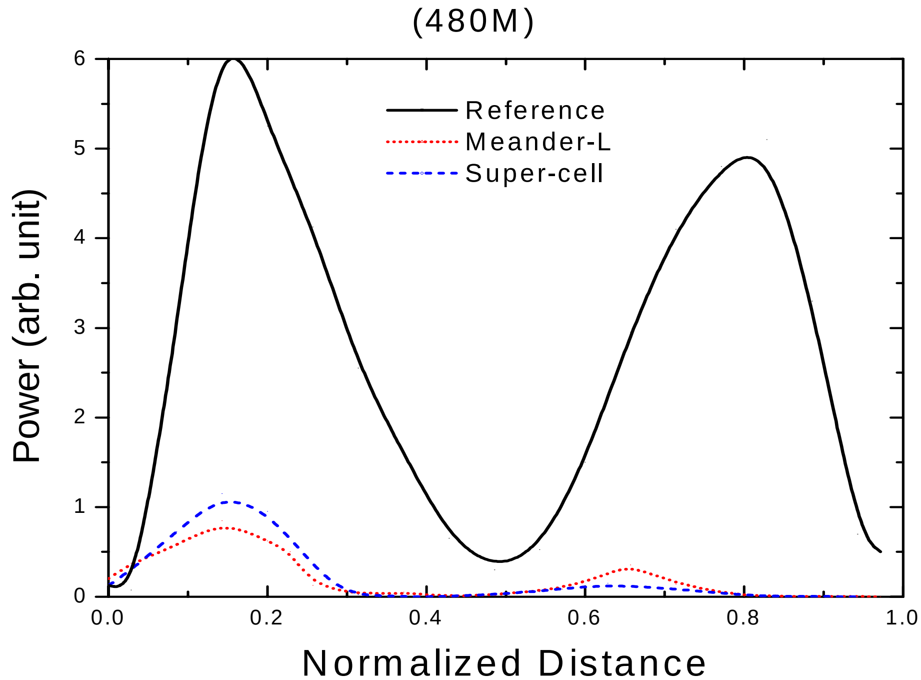

(480M)
Reference
Meander-L
Super-cell
Power (arb. unit)
Normalized Distance
0
1
2
3
4
5
6
0.0
0.2
0.4
0.6
0.8
1.0

(a)

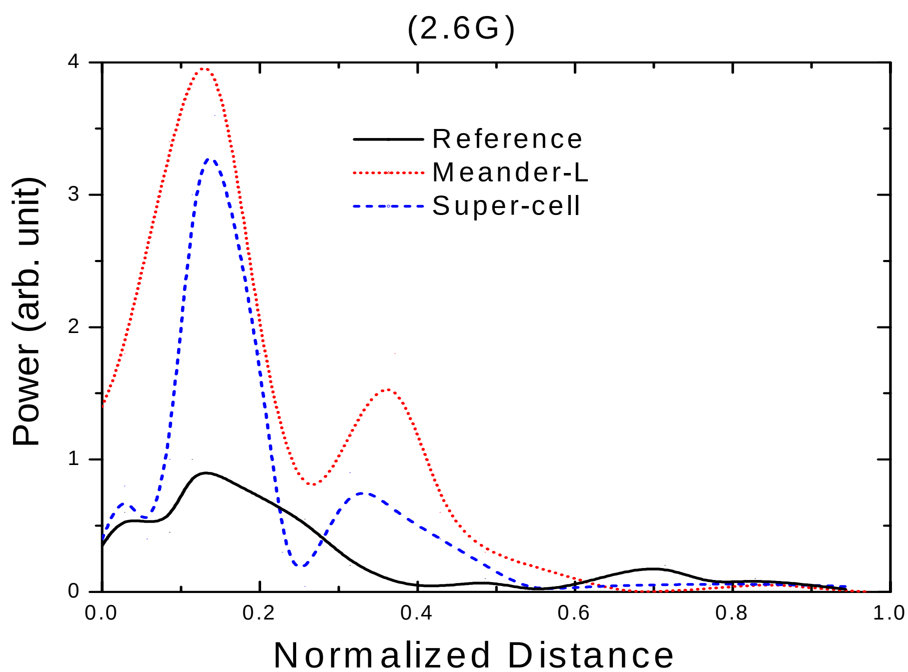

(2.6G)
Reference
Meander-L
Super-cell
Power (arb. unit)
Normalized Distance
0
1
2
3
4
0.0
0.2
0.4
0.6
0.8
1.0

(b)

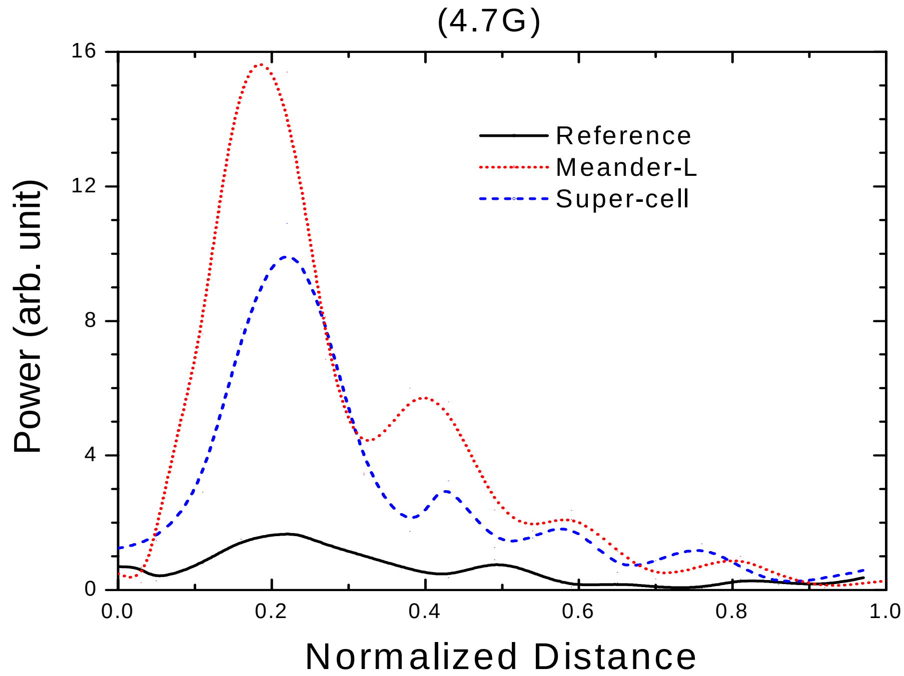

(c)

Figure 4- 5: Near field radiation intensity measured 1 cm above the board over the test line shown in Figure 4-4. Measurements performed for three different frequencies: (a) 480MHz, (b) 2.6GHz, and (c) 4.7GHz.

4.4 EMI Shielding Using EBG Patterned Surface

The results obtained above demonstrate distinct features of EBG patterned structures, such as reducing the total radiation, suppressing the resonance modes and surface current propagation, and localizing the field leakage around the excitation region. This suggests the use of the EBG patterned surface as an electromagnetic shield to reduce the radiation from power busses of PCBs.

Figure 4-6 is a diagram that shows the experimental setup used to test shielding effectiveness of the EBG planar structure. The total amount of radiation from both the edges of board and open slots is measured by S_{21} as a representative for the radiated power at various points along the test line as shown in Figure 4-4(b). Here, the input signal is fed to the parallel-plate environment through an SMA connector while a monopole probe is connected to the other port representing the receiver. Figure 4-7(a)-(d) show the measured magnitude of the S_{21} corresponding to different normalized distances of 0.15 (source), 0.44, 0.73, and 1 (far end of board edge). The data clearly demonstrates that for planar EBG-based power planes, when the test point is away from excitation region, wider and deeper bandgap can be achieved. Near field intensity with average suppression of 20dB is achieved in a wide frequency range from 0.5 to 4.6 GHz and 7-12GHz in comparison to the case without EBG structures. It is important to note, however, that such suppression is achieved at a distance spanning few patches from the source in a manner fully consistent with filter theory and EBG surface current suppression mechanism.

.

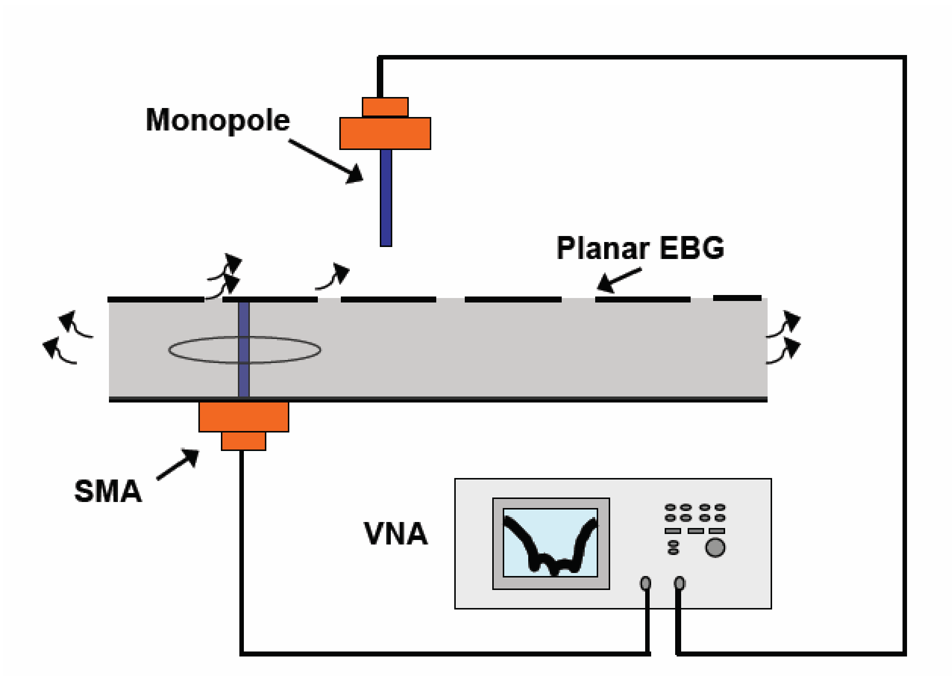

Figure 4- 6: Experimental setup for S_{21} Measurement for testing EMI shielding

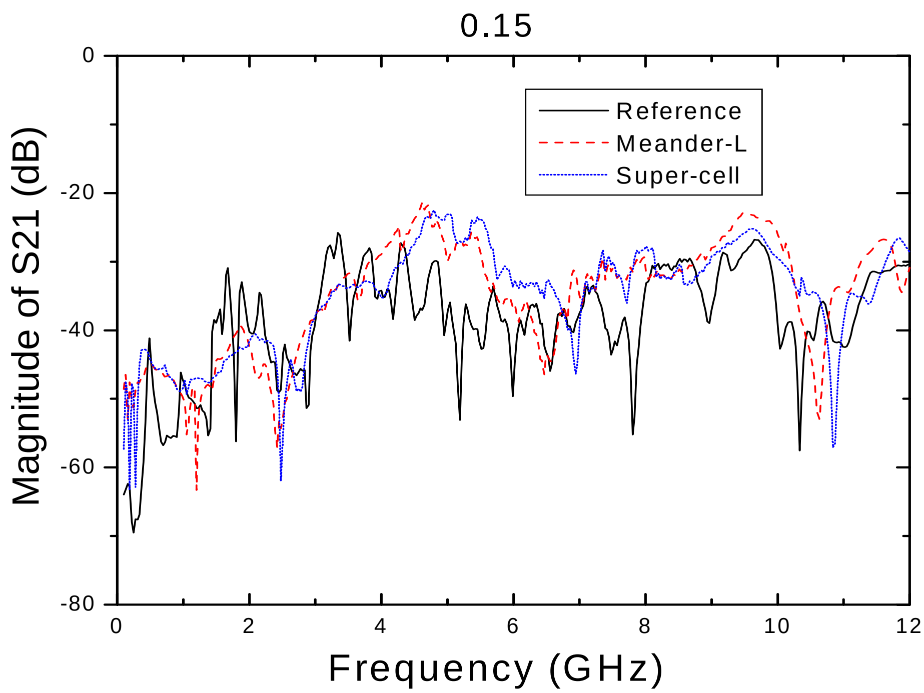

0.15
Magnitude of S21 (dB)
Frequency (GHz)
Reference
Meander-L
Super-cell
0
-20
-40
-60
-80
0
2
4
6
8
10
12

(a)

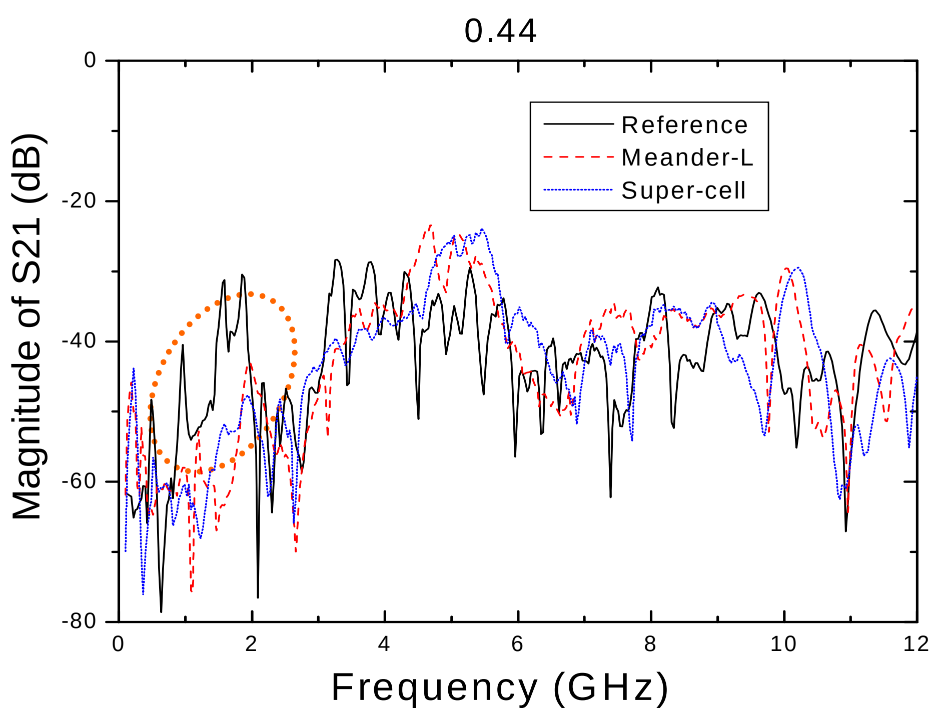

0.44
Magnitude of S21 (dB)
Frequency (GHz)
Reference
Meander-L
Super-cell
0
-20
-40
-60
-80
0
2
4
6
8
10
12

(b)

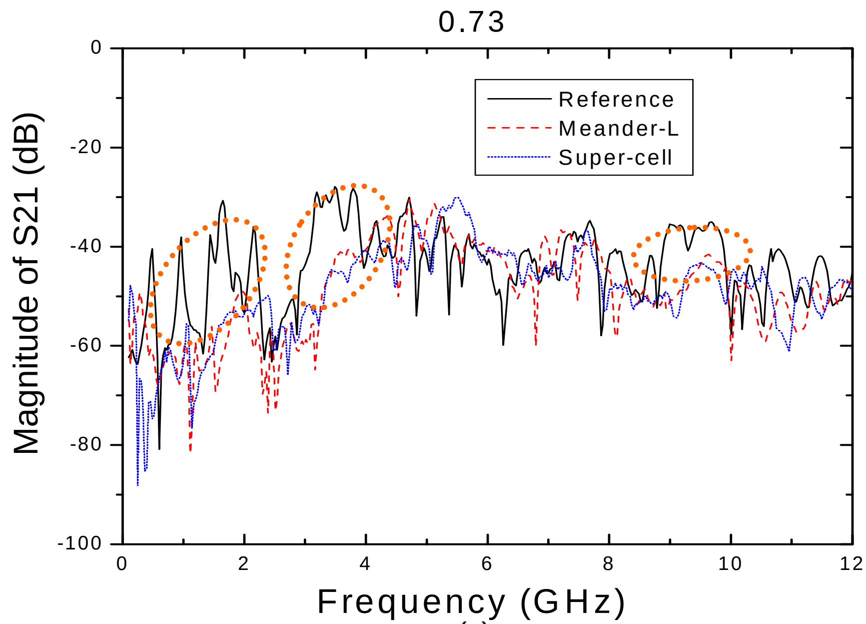

(c)

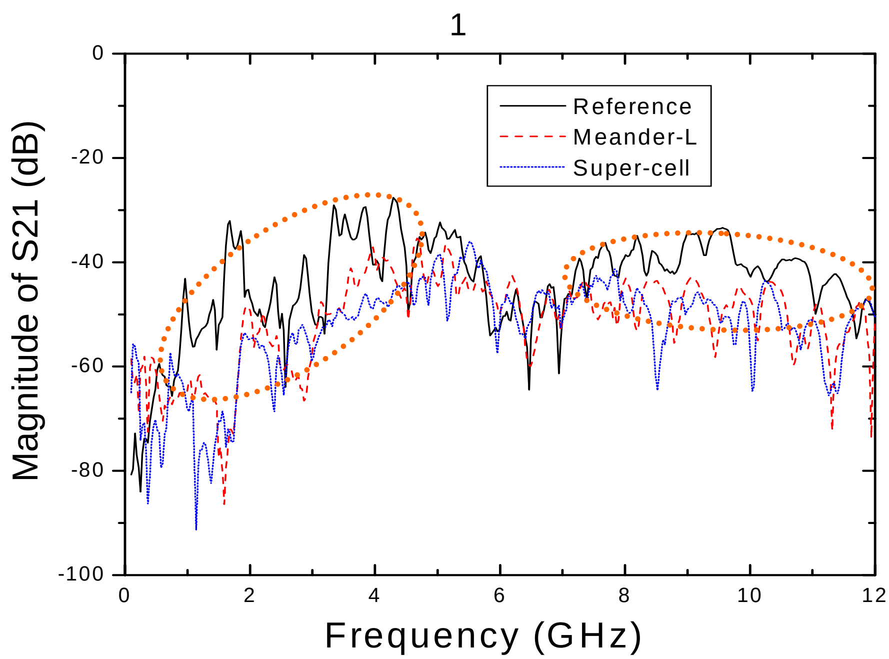

(d)

Figure 4- 7(a)-(d): S_{21} parameter measured at different test point represented by normalized distance (with respect to the size of the board): (a) 0.15 (coinciding with the source location), (b) 0.44 (c) 0.75, and (d) 1.

4.5 Antenna Normalization

It should be noted in the above measurements we use the same monopole antenna to characterize the field properties through the full measured frequency range, ie from 100MHz to 12 GHz. Actually this monopole antenna has different frequency response. While the measurement results (Figure 4-7) give us information of comparative results between field intensity of EBG patterned surface and that of the case with solid power plane, it cannot tell us the normalized field among the full frequency range for a single measurement. In order to get the normalized field intensity, antenna effective aperture must be known.

The monopole antenna we used is about 2.5cm in length. It is assumed the antenna is very thin, ie the diameter of the rod is much smaller than the wavelength of test frequency, and the ground is infinite large.

Antenna effective aperture (A_e) is defined as the ratio of the power delivered to the load to the incident power density [56, 57]. It characterizes the power collecting capability of the antenna. In general, for any linear reciprocal antenna it is found the effective aperture has a direct relationship with its directivity (D). The relation can be described as:

$$A_e = \frac{\lambda^2}{4\pi} D \tag{4.1}$$

The values of the directivity D for linear wire antenna for length within the range:

$0 \le l \le 3\lambda$ (this condition is satisfied for our measurement) have been calculated and are shown in the Figure 4-8 [57].

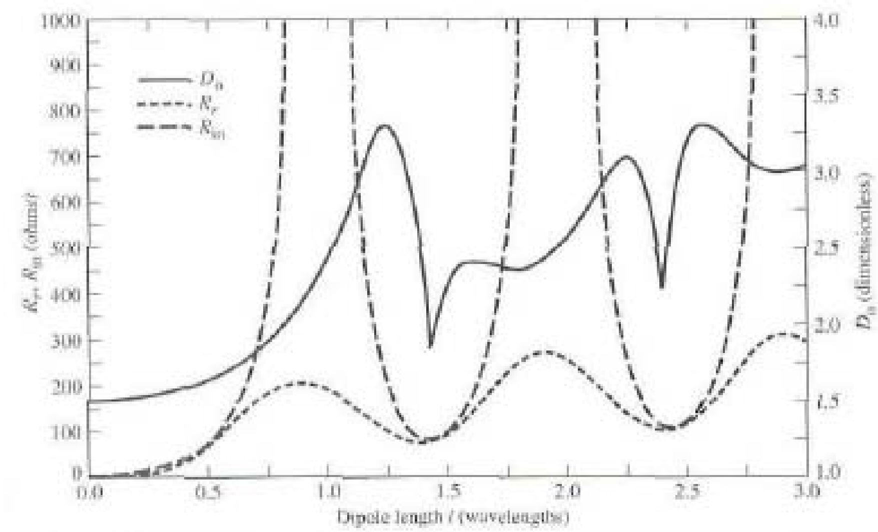

Figure 4- 8: radiation resistance, input resistance, and directivity of a thin dipole with sinusoidal current distribution ($0 \le l \le 3\lambda$) [57]

If there are losses associated with antenna, its effective aperture must be modified to account for its conduction loss, impedance mismatch, etc.

The impedance mismatch will induce voltage reflection at the input terminals of the antenna. This means the partial energy of antenna picking up from the environment cannot be transmitted to the load (50 Ohm for the VNA input). The voltage reflection coefficient can be determined directly by measuring the S_{11} parameter of this monopole antenna as shown in Figure 4-9.

We notice the dip at 3.7G is corresponding to the self resonance of this monopole antenna where most of the power is radiated with minimum reflection. So finally the modified effective aperture can be expresses as:

$$A_e = (1-|S_{11}|^2)\frac{\lambda^2}{4\pi}D \tag{4.2}$$

Because S parameter measures the ratio of voltage, A_e represents the ratio of power. So the normalized factor should be:

$$\sqrt{\frac{(1-|S_{11}|^2)\cdot D}{4\pi}}\cdot\lambda \tag{4.3}$$

When substitute the data of S_{11} (from Figure 4-9) and D (from Figure 4-8), the final normalization field can be obtained.

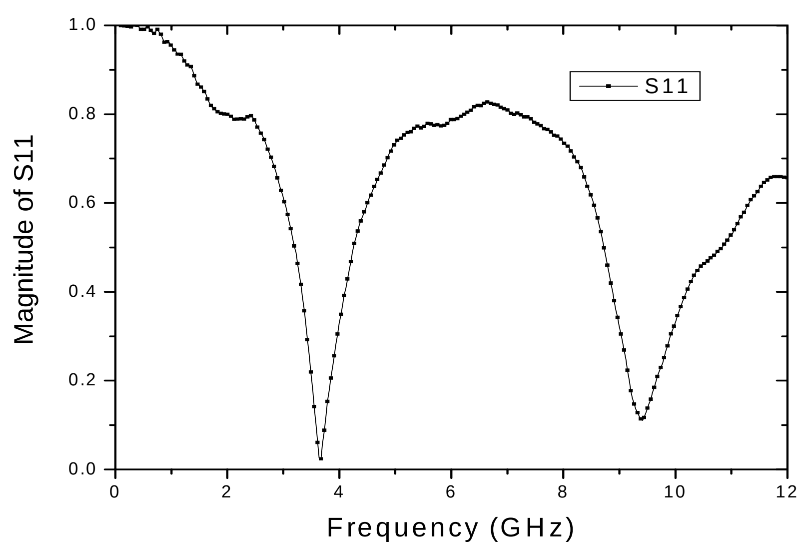

Figure 4- 9: S_{11} measurement of monopole antenna

4.6 Summary

In this study, leakage radiation effects from EBG-patterned surface containing open slots are carefully investigated numerically and experimentally. Comparing with solid reference plane, it is found that the strong field leakage from this perforated EBG structure is mainly concentrated around the feeding point and the field intensity attenuates strongly as the distance from the excitation region increases. In addition, this planar EBG structure can effectively suppress resonant modes of cavity. Finally, we introduce a novel concept of applying electromagnetic bandgap structures for the suppression of electromagnetic radiation generated by high speed and high-current switching from power busses of printed circuit boards. It is found 20dB field attenuation is achieved over wide frequency range because EBG electrical filtering effects can effectively shield the PCBs and therefore reduce the level of radiation from edges of boards or open slots. In summary this planar EBG structure not only strongly reduces the power/ground noise for a wide frequency range, but also can be used for wideband field mitigation for EMI applications.

CHAPTER 5

Signal Integrity of Power Plane with Electromagnetic Bandgap Structures

5.1 Introduction

In recent years, silicon-based complementary metal-oxide semiconductor (CMOS) technology and circuits have been advancing to several gigabits interface standards. As digital designs migrate to gigahertz signal frequencies, signal-integrity issues, such as reflections, cross talk, frequency-dependent transmission line loss and dispersion, can significantly degrade system performance and reliability [58-60].

In chapter 2 and 4, we have demonstrated that the power plane with electromagnetic bandgap structures shows excellent performance on mitigation of SSN and corresponding EMI reduction at wide frequency range, while the strong reflection noise due to impedance mismatch of perforated planes may also result in degrading the signal quality for the signal traces referring to these imperfect planes. Its effect on the propagating signal needs to be investigated, especially in light of recent studies [21, 27, and 28].

In this chapter, signal integrity (SI) for a trace on top of embedded EBG boards is characterized in the time domain with the eye diagram. The eye diagram, which is commonly used in signal integrity characterization, gives an indication of the signal quality. Typically, the larger the eye opens, the better the signal quality is.

First, we will introduce some basic concepts of eye diagram. Then we will characterize the effect of multi-layer boards with embedded EBG patterned power plane on the SI. Some possible solutions to improve the signal quality of power plane are proposed finally.

5.2 Eye Diagram Characterization

Eye diagram provides a quick and intuitive view of parametric performance of a system. The quality of a digital signal can be judged successfully with this method. First let us look how the eye diagrams are created. Considering a data string to be composed of a sequential bits with value 1 (high) or 0 (low), if the data string is looked at an oscilloscope screen, we would see the right-hand bit appears first. Then it would shift to the right (in time) and we would see the next bit. So if we are going to read the data string as it passes by a point in our circuit we would read (from right to left) 1-0-1-1-0-1-0-0, and so on.

More generally, if we look at a specific point in a circuit and watch a large number of data streams passing by that point, and look only at the three most recent bits, there are only eight possible combinations of bits that would pass by. Now if we take a time exposure of a large number of data bits passing a point, and superimpose them on a single graph, they would look like as shown in Figure 5-1.

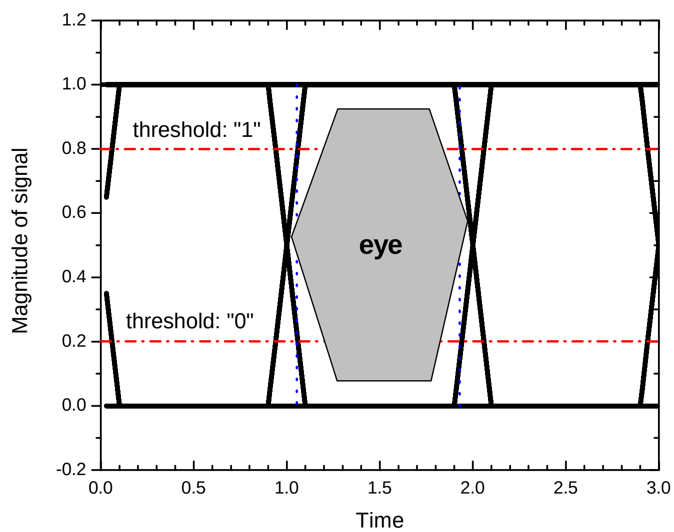

Figure 5- 1: Typical eye diagram generated with three data bits, showing the threshold level of logic “0” and “1”

Figure 5-1 represents an ideal eye diagram. It shows all possible combinations of three data bits passing by a point in a circuit. The transition between logic states is very clean and predictable. The upper and lower logic threshold levels are indicated in the figure. The vertical lines represent the sampling time during which there will be no logic errors. That is, if the data stream is sampled between these times, the data will always be in a correct and valid state. This is referred to be an eye diagram because of the obvious resemblance of the open area to an eye. So eye diagram is obtained by overlaying multiple unit intervals of a long data stream.

Much of information can be gained merely by looking at such an eye pattern, and the system performance can be judged based on some parameters, such as eye amplitude, eye width, eye jitter, and rise/fall time etc.

Eye amplitude provides an idea of the level one and the zero of the waveform. Amplitude distortion of the signal along the trace, due to discontinuities or losses, reduces the eye opening and the noise margin, so that the receiver at the end of the line has difficulties in correctly detecting the signal. The eye width gives information about the time interval where the data can be sampled at the receiving end without problems due to inter-symbol interference. Eye rise/fall time is a measure of the transition time of the data on the rising/falling edge of a waveform. Eye jitter is a measure of the time variances of the rising or falling edges of a pulse waveform at the middle threshold. The eye can become completely closed if the data signal has a lot of timing jitter with respect to the master clock, or if varying amounts of noise and attenuation cause the signal amplitude to vary excessively.

In general, the vertical thickness of the line in the eye diagram is indicative of the AC voltage noise, whereas the horizontal thickness is indicative of the AC timing noise (jitter). A very clean signal will have a large, clear eye, while a noisy, low-quality signal will have a smaller one.

5.3 Eye Diagram of Power Plane with EBG Structures

5.3.1 Test vehicle description

Here we consider four-layer PCB structures, and compare two different cases: in the first case (structure A), the signal propagates on a microstrip line and is referenced to a solid plane (return current path). In the second case, the signal is referenced to an EBG patterned plane (structure B).

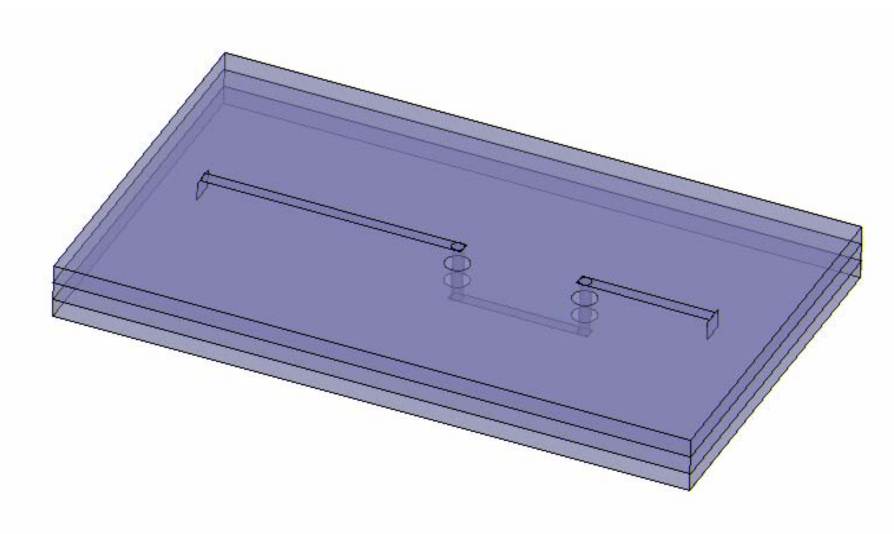

Figure 5- 2: 4-layer PCBs with signal layer referring to solid power plane

(Structure A)

For structure A as shown in Figure 5-2, the middle 2 layers serve as solid power/ground planes. The signal propagates along the trace on the top signal layer, through via down to the bottom layer and back to the top layer again. All layers are filled with FR4, with thickness of 1.54mm for each layer. The board geometry is 90mm x 150mm as used in previous examples. The signal traces are designed as 50 Ohm lines (with respect to a solid reference plane). In structure B, the middle 2 layers are replaced with a meander line EBG structure. The 3D view and side view of structure B are shown in Figure 5-3(a), (b).

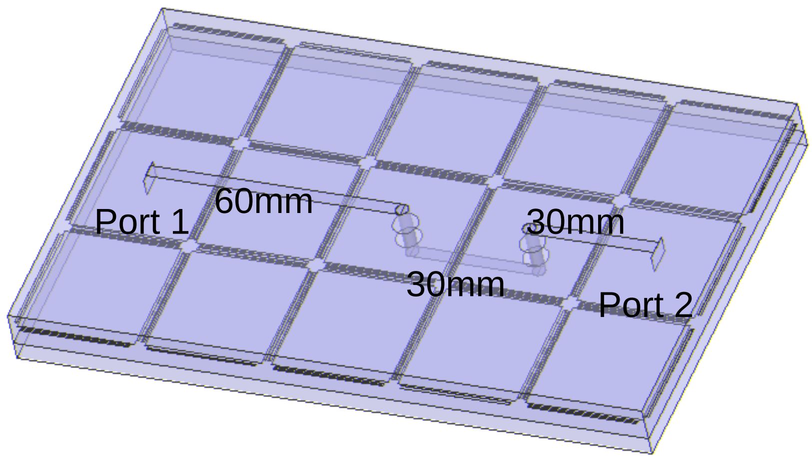

(a)

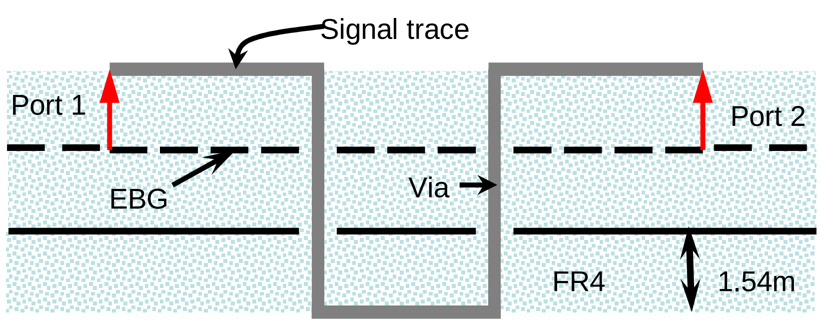

(b)

Figure 5- 3: (a) 4-layer PCBs with signal layer referring to the Meander-L EBG patterned power plane (structure B) (b) Side-view.

First we take a look of the S_{21} parameter for both structures as shown in Figure 5-4. We see stronger attenuation of S_{21} parameter, especially at higher frequency range for the EBG patterned structure B when compared with solid plane of structure A. This may induce a signal integrity problem. Next we will characterize this effect with eye diagram tool.

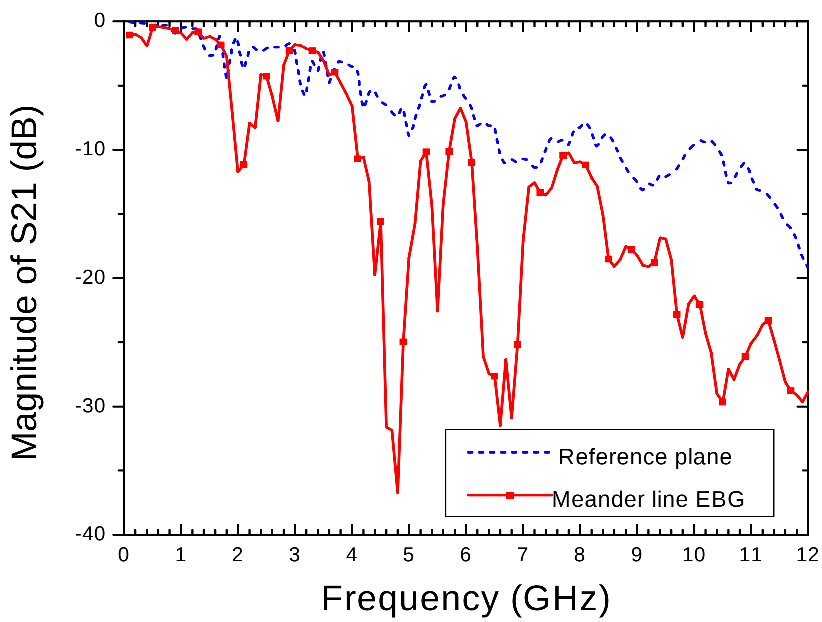

Figure 5- 4: Comparison of S parameter for structure A (dotted line) and structure B (solid line)

5.3.2 Eye diagram of meander-L EBG structure

A non-return to zero (NRZ), pseudorandom binary sequence (PRBs) 2^7-1 is sent at input (port 1, shown in Figure 5-2 and 5-3 respectively), and the signal propagation properties is monitored at output (port 2). The launched PRBs are coded at 1Gbps, with 1V swing, and nominal rise/fall time is 200ps. The eye patterns are generated by using Agilent ADS convolution simulator, which convolving the inverse fast Fourier transforms (IFFT) of the scattering parameter along the traces directly. Figure 5-5 (structure A) and 5-6 (structure B) show the input (ideal data stream) and output (after passing structure A or B) of 2^7-1 PRBs at time domain, frequency domain respectively. The simulated eye diagrams for signal streams at the end of traces of structure A and B are shown in Figure 5-7.

In frequency spectrum of structure B, there is a significant dip around 400MHz, and stronger attenuation at higher frequencies as shown in Figure 5-6, which means the signal at these frequencies cannot be propagated through the EBG structure. This result is consistent with the S_{21} parameter measurement shown in Figure 5-4.

The data in Figure 5-7 shows the eye significantly shrinks. This indicates that the signal quality is seriously degraded for structure B. This is mainly due to the strong reflections arising from these imperfect EBG patterned power planes. When EBG pattern structure is used as one of power/ground plane, it may seriously affect its eye pattern; the digital signal cannot be faithfully transmitted to make digital circuit system function properly. Next we will discuss some possible ways to improve the signal quality.

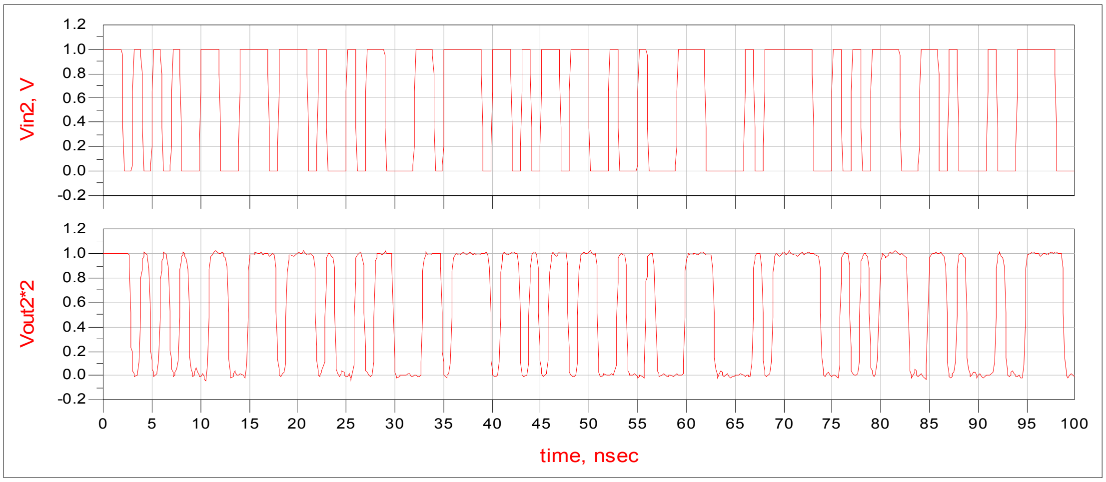

(a)

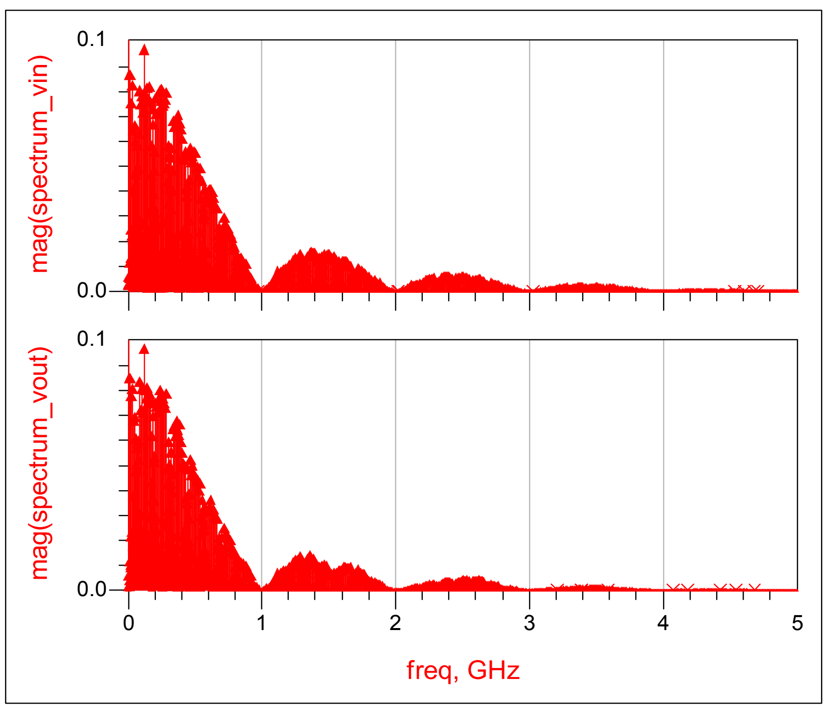

(b)

Figure 5- 5: Comparison of input (original 2^7-1 PRBs) and output at time domain (a) and frequency domain (b) (note for each graph, the original signal is shown at top half, the output signal is shown at bottom half) ------- Structure A

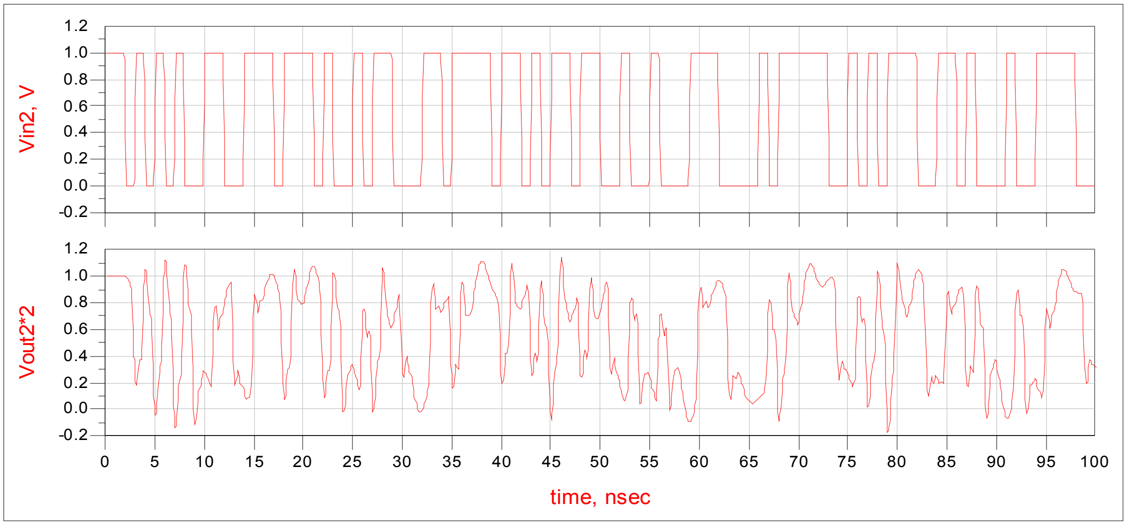

(a)

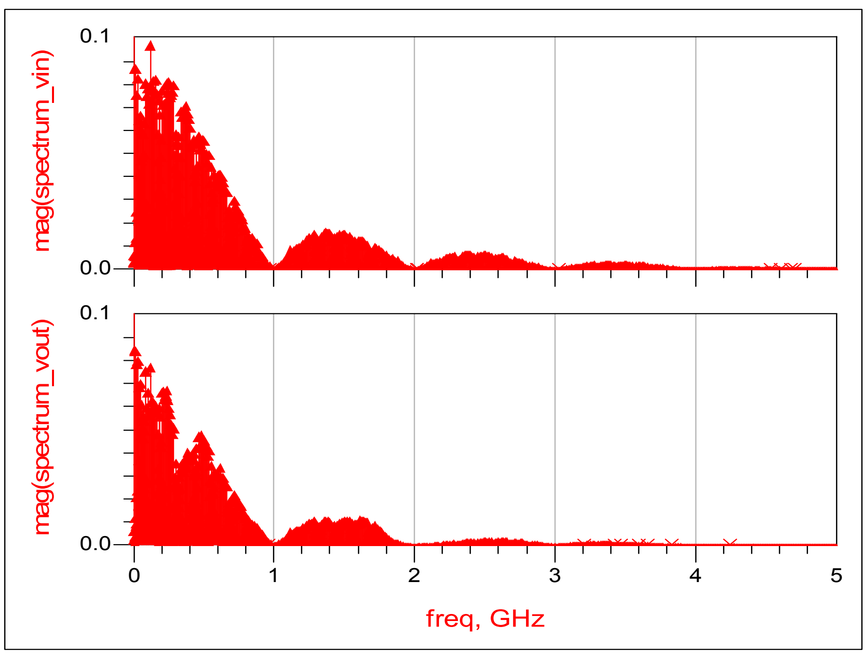

(b)

Figure 5- 6: Comparison of input (original 2^7-1 PRBs) and output at time domain (a) and frequency domain (b) (note for each graph, the original signal is shown at top half, the output signal is shown at bottom half) ------ Structure B

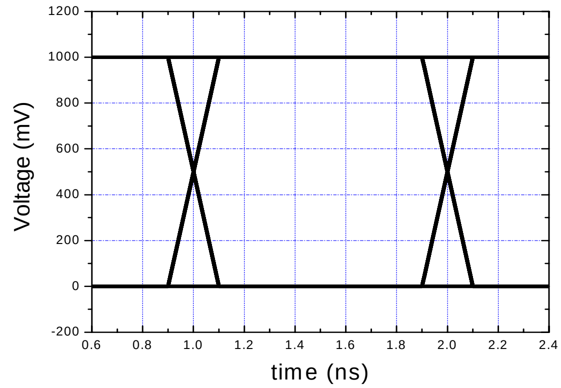

(a)

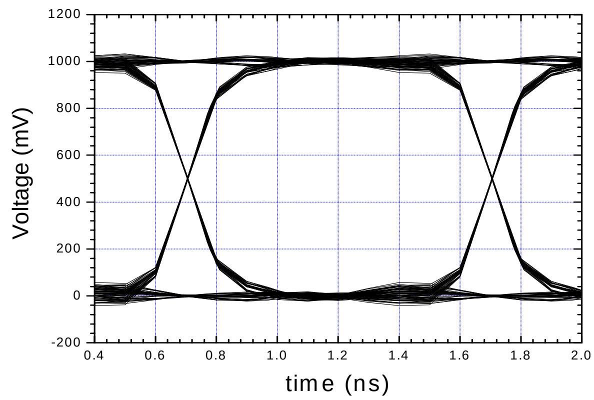

(b)

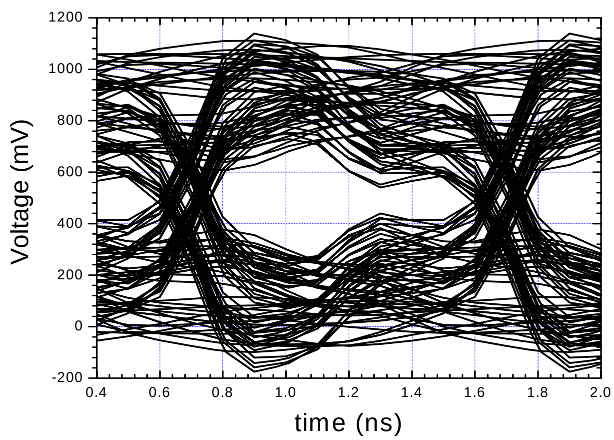

(c)

Figure 5- 7: Eye diagram for input (2^7-1 PRBs) and output of structure A (b) and structure B (c)

5.3.3 Differential pair scheme

In order to improve the signal quality, differential signaling approach is adopted.

A differential pair is made of two transmission lines. Each transmission line can be a simple, single-ended transmission line with a signal propagating on each line, and the differential signal between the two lines. Together, these two lines are called a differential pair. Compared with single-ended signaling propagation, differential signaling has a number of advantages. Strong coupling between the two signal lines allows differential signals to propagate with less noise picked up from other active nets. The greater the coupling, the more robust the differential signals will be to discontinuities and imperfections.

In the example considered here, the traces are designed with a differential impedance of 100 Ohm for the differential pair configuration shown in Figure 5-8. The width of the lines is 2mm, and the spacing between the two lines is 3mm. The excitation signal is still the same as before, 2^7-1 PRBs is feed differentially at the two terminals of input, and eye diagram is monitored at the other ends of the differential pair. Figure 5-9 shows the differential signal of the input and output, ie before and after passing EBG structure, at time domain and frequency domain respectively. It can be seen the signal quality is greatly improved if compared with that of the single line feeding as shown in Figure 5-6.

Two parameters, maximum eye open (MEO) and maximum eye width (MEW), are used as metrics of the eye pattern quality. MEO represents maximum difference between points in the interior of the eye diagram at the same time instant. MEW measures the maximum difference, at the same voltage level, between two points in the interior of the eye diagram. The simulated eye diagram in Figure 5-10 shows for the differential signaling case, MEO = 950mV, and MEW = 980ps. This is a sizable improvement in comparison to the case of the single line. So it is a practical way to apply EBG structures as one of power/ground plane to mitigate SSN noise without degrading the signal propagation performance if using differential pair configuration.

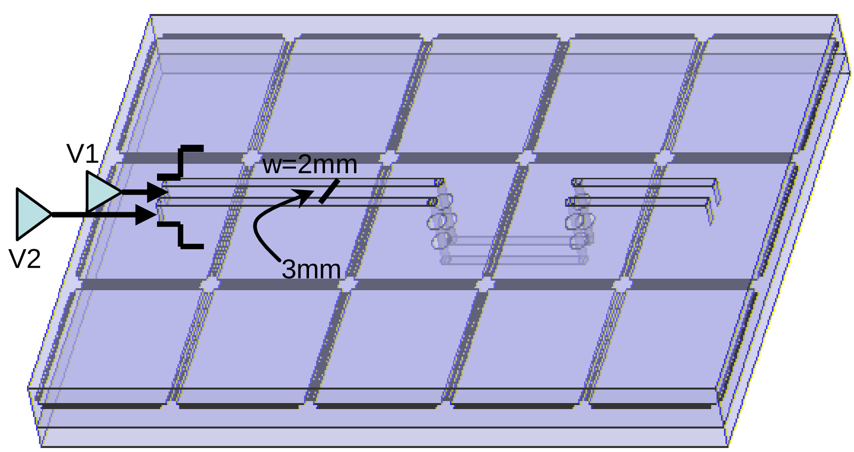

Figure 5- 8: Test geometry for Meander-L EBG patterned structure for differential pair configuration

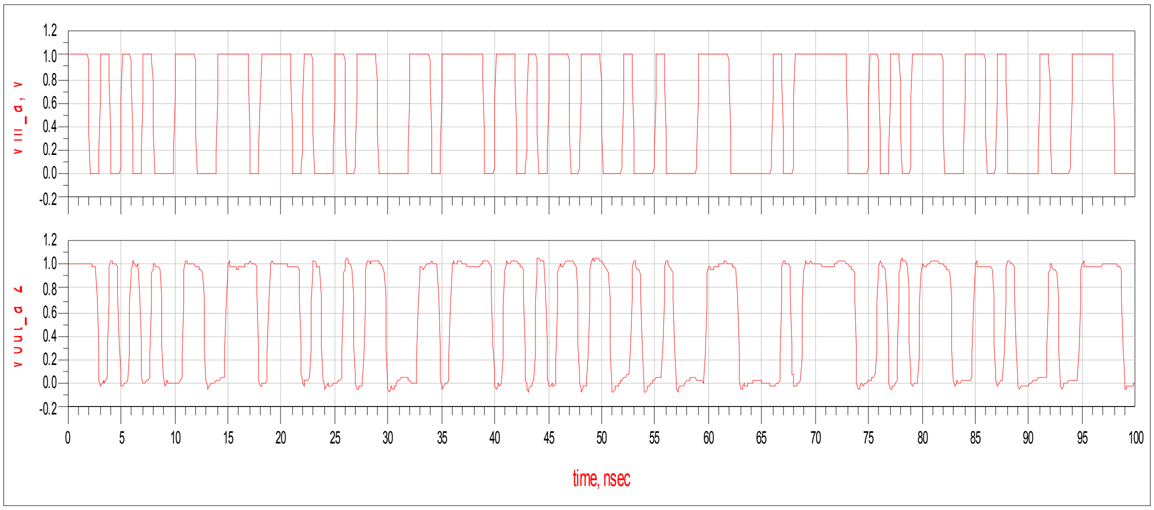

(a)

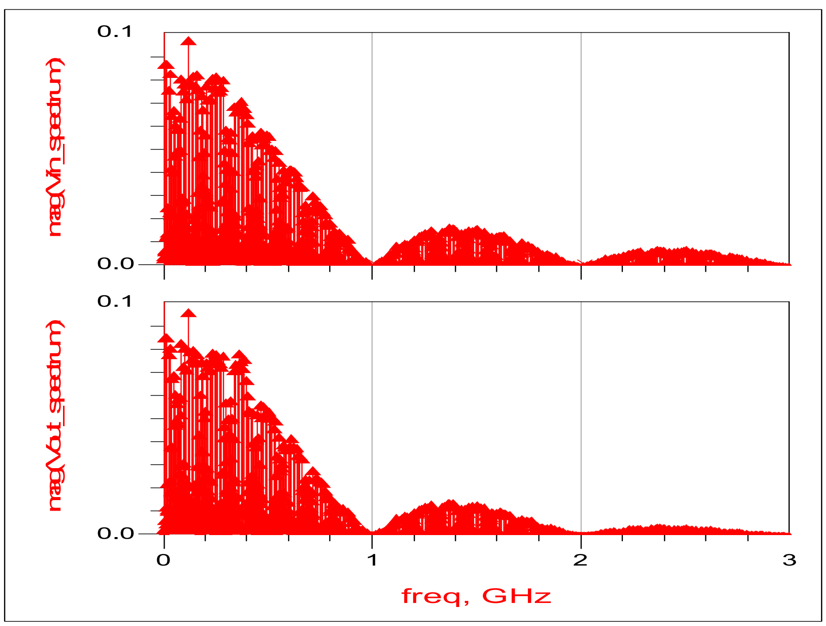

(b)

Figure 5- 9: Comparison of input (original 2^7-1 PRBs) and output (after passing structure B) with differential pair configuration at time domain (a) and frequency domain (b) respectively.

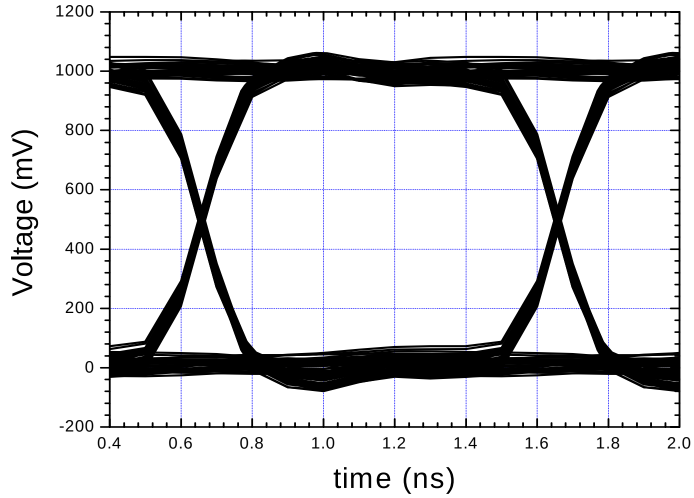

Figure 5- 10: Eye diagram for Meander-L EBG patterned structure with differential pair configuration. .

5.3.4 5-layer structure scheme

Another idea to improve the signal quality for the EBG patterned power plane is adding one more solid ground plane above EBG patterned power plane. The 3D view and side view of this type of structure is shown in Figure 5-11, the EBG power plane is sandwiched between two solid ground planes. As the signal traces are now referencing uniform plane, it is expected the reflection noise due to the impedance mismatch is substantially removed, and good signal quality is achieved as shown in Figure 5-12, where MEO = 950mV, and MEW = 980ps. Compared with the performance of single-ended signaling using a four-layer design shown in Figure

5-7(c), the advantage of this type of design is that the signal quality is much better than the previous design because both reference planes are now continuous, but the design is at the cost of one more layer need to be added.

(a)

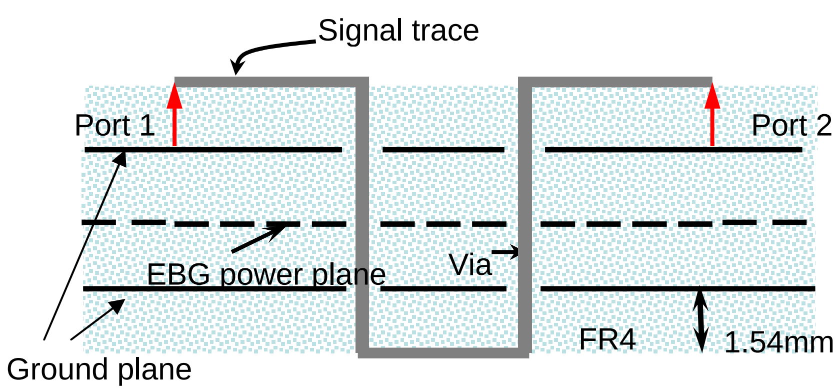

(b)

Figure 5- 11: 5-layer PCBs with Meander-L EBG structure sandwiched between two solid ground planes (a) 3D view (b) Side-view.

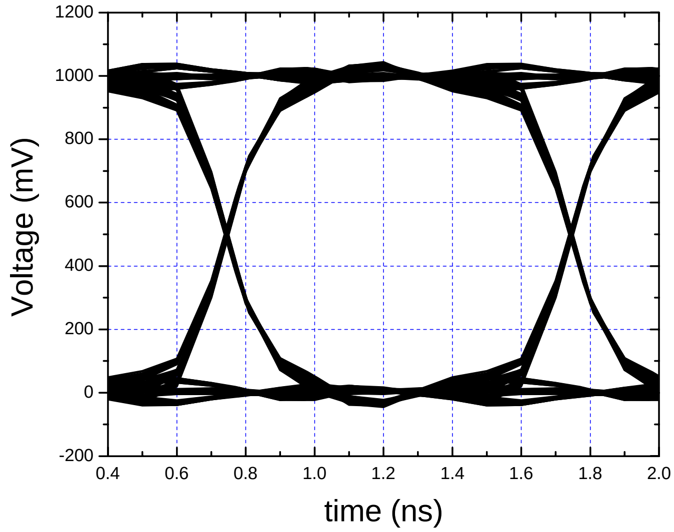

Figure 5- 12: Simulated eye diagram for single-ended trace of meander-L EBG structure with 5 layer PCBs configuration.

5.3.5 Eye diagram of super-cell EBG structure

If the Meander-L EBG structure is replaced with the super-cell EBG structure, the corresponding simulated eye diagram for single-ended signal is shown in Figure 5-13. The test pattern is the same as that described before. It can be seen that for super-cell patterned structure, MEO=800mV, and MEW=940ps. Comparing with performance of meander-L EBG structure shown in Figure 5-7(c), we observe that the eye pattern for the super-cell EBG structure is more open. A possible explanation for this is that the Meander-L structure induces extra phase difference per unit length (due to increased inductance) when the signal propagates along the traces, which results in the degradation of signal quality. So, the signal quality for signal traces referring to this super cell EBG patterned plane is acceptable (only with mild signal degradation) in high speed circuits even at single-ended signal configuration.

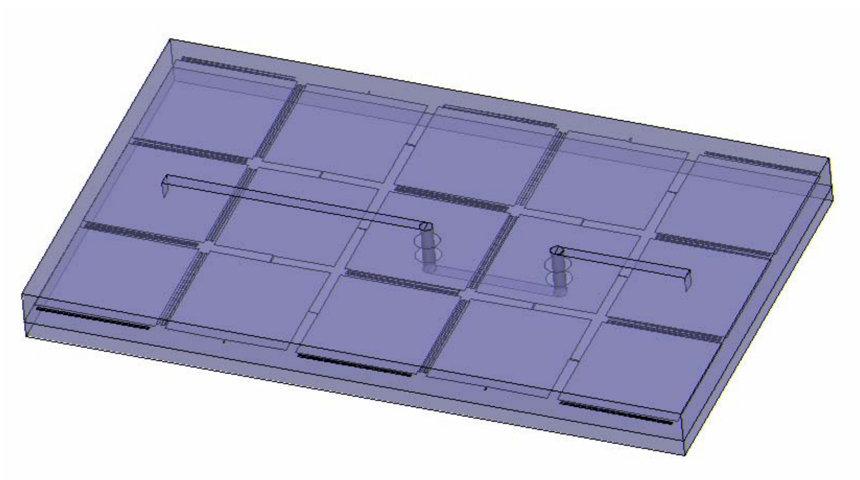

(a)

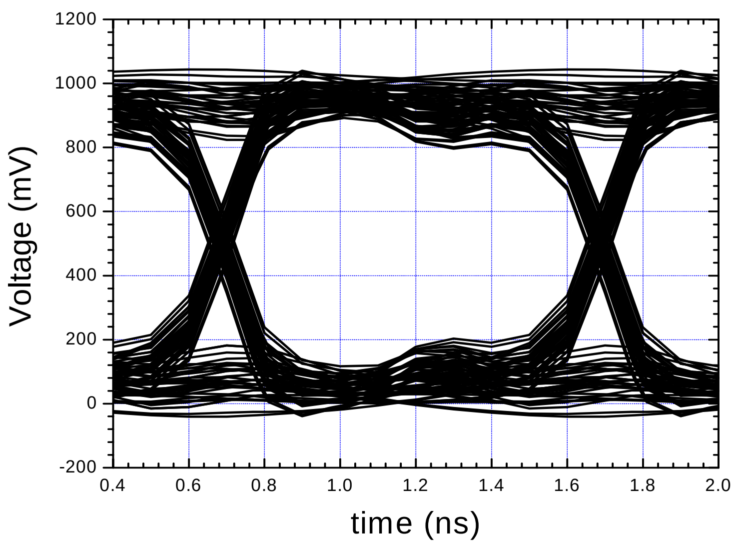

(b)

Figure 5- 13:(a) Test geometry for super cell EBG patterned structure for single-ended signal configuration (b) Corresponding eye diagram

5.4 Voltage Drop of Power Plane with EBG Structure

As we know, power distributed system (PDS) can be modeled as a combination of RLC network [54, 55]. A time-varying current (due to switching) across an inductor gives rise to a voltage variation on the power plane. As discussed in section 2.3.1, the meander lines of the EBG structures can be modeled as an effective inductance. While the increase of effective inductance facilitates suppressing noise propagation over a wide frequency range, especially down-shifting the lower corner frequency, on the other hand this may also induce side-effects. The increased inductance may result in larger voltage fluctuation because of the relationship: $V_{fluct} = L \cdot {di}/{dt}$ shown in equation (1.1). In the following, we study the effect of EBG structures on the voltage fluctuation of power/ground plane.

5.4.1 Circuit schematics

The general configuration of EBG structure with driver to study the switching noise is shown in Figure 5-14. The driver is made of a CMOS which consists of one NMOS and one PMOS transistor in series. The EBG patterned power plane can be viewed as a black box, which is represented by S parameter from the simulation data using HFSS. The switching noise voltage is monitored at port 2. EBG-patched plane is sourced with power supply voltage V_{dd}, and GND is provided to solid ground plane at port 1 (the right edge of board shown in Figure 5-14).

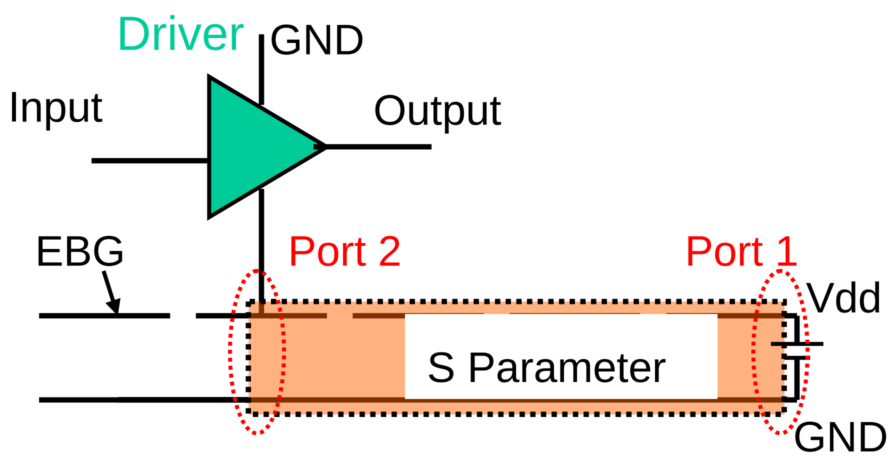

Figure 5- 14: General configuration of EBG structure with driver to study the switching noise

The circuit analysis tool is Agilent ADS. The simulation block diagram is shown in Figure 5-15, where V_{in} is input signal. The output signal (invert to input signal) is represented by V_{out}. V_{dd} is selected to be 2.5V here. The voltage drop on EBG patterned power plane is monitored at V_{out2}. For the CMOS inverter, typical values for R_{ds} is around 10K, the buffer's current draw is very small, assumed I_{ds} is around uA scale. In practical application, usually thousands of transistors are switching simultaneously, so they can drop larger current from power/ground plane. In my simulation I assume the output driving current is over mA scale. The input signal is a clock stream with period 1ns, duty cycle 50%, and rise/fall time 100ps.

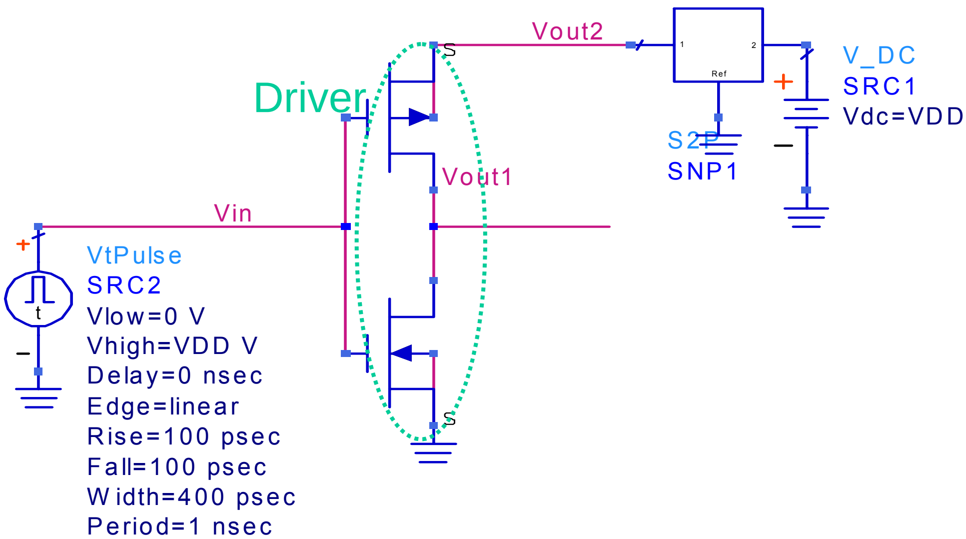

Figure 5- 15: Simulation block diagram studying the voltage drop (Agilent ADS) represented by V_{out2}

5.4.2 Simulation results and discussion

The simulated voltage variation of EBG patterned power/ground plane is shown in Figure 5-16, the magnitude is around 0.2V for 2.5V input signal. In order to see if this EBG structure will induce extra effect on the switching noise, here we compared the voltage fluctuation of EBG patterned power plane with that of solid power plane, and the result is shown in Figure 5-17. Actually we do not see much difference between these two different cases. The meander-lines do not result in larger fluctuation as we expected before. The reason is the EBG structure is not just a simple inductance problem, either the solid power/ground plane or EBG patterned power/ground plane can actually be modeled as a complicated RLC network as we talked before. The parasitic capacitance in the structure itself has “eaten up” some effects of voltage fluctuation. According to other studies [4. 61, 62], adding a decoupling capacitance between power plane and ground plane near the via can reduce this voltage drop across the power plane. Our simulation results shown in Figure 5-17 also confirm this conclusion. Here we put the 5pF capacitance in parallel, and the voltage drop fluctuation is significantly decreased. This is due to the intrinsic capacitance property which inhibits the voltage variation across itself. We also notice if bigger decoupling capacitance added in parallel, the stronger attenuation would be for voltage fluctuation.

In summary, the EBG structure with more turns of meander lines is helpful to widen the bandgap and lower the corner edge frequency. The meander-lines will not induce extra power/ground bounce to the circuits due to its parasitic RLC effects, so this EBG structure has a great potential to be used in power/ground plane to mitigate the propagation of switching noise without any circuit degradation.

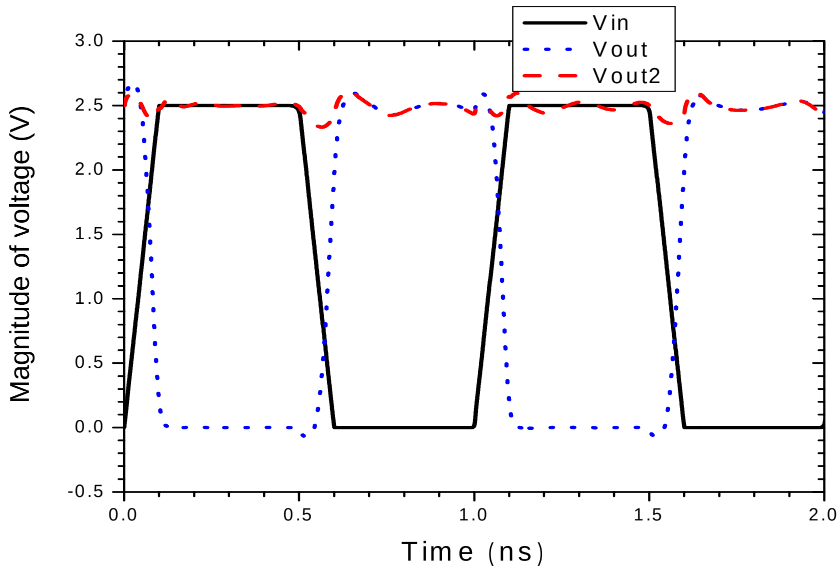

Figure 5- 16: simulated voltage fluctuation (V_{out2}) on meander-line EBG patterned power/ground plane, where V_{in}: input voltage, V_{out}: output voltage

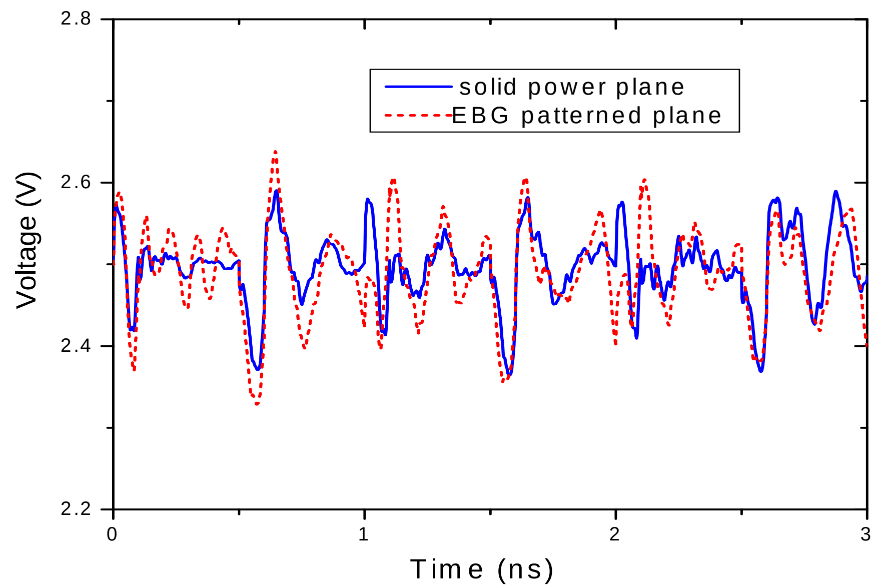

Figure 5- 17: Simulated voltage drop of meander line EBG patterned power plane compared with that of solid power plane

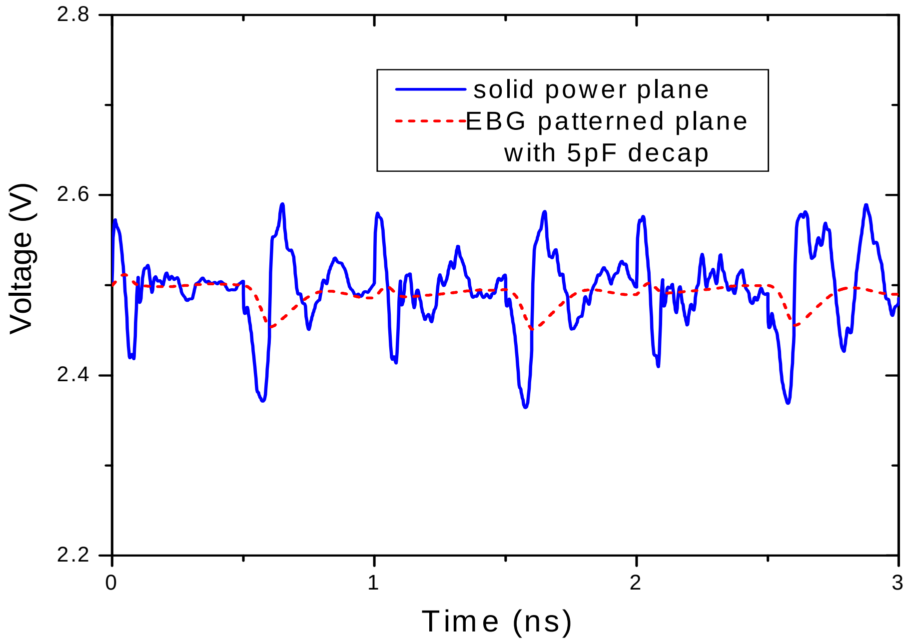

Figure 5- 18: Simulated voltage drop in power/ground power plane with decoupling capacitor (here the decap is chosen as 5pF) compared with the case without decap.

CHAPTER 6

Conclusions and Future Work

6.1 Conclusions

In this thesis, new technology to mitigate the propagation of simultaneous switching noise (SSN) and resonance modes in high speed circuits and packages is studied and the following results are obtained.

Novel design of power/ground plane with planar EBG structures for suppressing SSN has been developed. The novel design is based on using meander lines to increase the effective inductance of EBG patches. A novel concept of *super cell* EBG structure, comprising two different topologies on the same board, is proposed to extend the lower edge of the band. Both novel designs presented in this study are also validated experimentally. A -28dB suppression bandwidth starting at 250MHz and extending to 12GHz and beyond is achieved.

Lumped-element based compact models of the planar EBG structures are developed both for one dimensional and two dimensional cases. Main factors which affect the EBG bandgap features are discussed and general instruction for designing new types of EBG structure can be inferred. The physical mechanism behind these EBG structures is also addressed. The circuit models are further validated with the dispersion diagram of EBG structures calculated with periodic wave equation analysis.

Leakage radiation effects from EBG-patterned surface are carefully investigated numerically and experimentally. EBG structures are shown to be a very effective tool for suppressing Electromagnetic Interference (EMI) from PCBs. A novel concept of using EBG structures as an enhancing shielding technology is developed.

The effect of the planar EBG structures on signal integrity (SI) of multi-layer PCBs is also investigated. Time domain analysis of planar EBG structures is characterized with the tool of eye diagrams. Some methods, such as differential signaling and 5-layer structure, are introduced to improve the signal quality of the EBG patterned multi-layer printed circuit boards.

In addition, some important issues closed related with this study are also carefully addressed, such as SSN frequency range limitation, effect of EBG structures on local switching noise generation, etc.

In summary, this thesis developed a new effective design of planar EBG structure to mitigate noise propagation in power distributed system (PDS). By carefully characterize its EMI and SI performance, we show this planar EBG structure has a potential to be used in next generation IC packaging technology.

6.2 Future Work

Miniaturization is a still challenging work. To design a compact, miniaturized EBG structure is a key issue to apply this technology in the future industry applications. Although we have numerically proved high k thin film material is a possible way to achieve this goal, while fabrication processes and material availability at this time are not adequate for such designs. It is recommended future work can address this issue.

Our work introduce for the first time the possibility of using complex cell structures to achieve very wide bandgap with a starting frequency of approximately 250MHz and extending to 12GHz and beyond. We note that there is no unique choice for the topology of the connecting bridges between patches. Such structure chosen here represents a generic type of structures with increased degrees of freedom to allow optimization for specific design needs. These connecting meander and straight lines can be changed to more complex structures thus enhancing the tunability of the bandgap. Therefore, we believe that more work needs to be done to understand the full potential of complex structures as the one introduced here. Following an in-depth understanding of the potential of such complex structures, design guidelines will naturally follow.

Bibliography

[1] D. J. Frank, "Power-constrained CMOS scaling limits," *IBM Journal of Research and Development,* vol. 46, no. 2/3, , pp.235-244, 2002.

[2] S. H. Hall, G. W. Hall and J. A. McCall, *High-Speed Digital System Design: A Handbook of Interconnect Theory and Design Practices,* Wiley-IEEE Computer Society, 1st edition, Jan. 2000.

[3] L.D. Smith, "Simultaneous switching noise and power plane bounce for CMOS technology," in *IEEE 8th Topical Meeting Electr. Perform. Electron. Packag.,* San Deigo, CA, Oct. 25-27, 1999, pp. 163-166.

[4] R. Senthinatan and J. Price, *Simultaneous Switching Noise of CMOS Devices and Systems,* Norwell, MA: Kluwer, 1994.

[5] V. Ricchiuti, "Power-supply decoupling on fully populated high-speed digital PCBs," *IEEE Transactions on Electromagnetic Compatibility,* vol. 43, no.4, pp. 671-676, Nov. 2001.

[6] S. Radu, R. E. DuBroff, J. L. Drewniak, T. H. Hubing and T. P. VanDoren, "Designing power bus decoupling for CMOS devices," *Proc. of the IEEE International Symposium on Electromagnetic Compatibility, Denver,* CO, USA,

23-28 August 1998, vol. 1, pp. 375-380.

[7] A. Madou and L. Martens, “Electrical behavior of decoupling capacitors embedded in multilayered PCBs,” *IEEE Transactions on Electromagnetic Compatibility*, vol. 43, pp. 549–556, Nov. 2001.

[8] M. Xu, T. H. Hubing, J. Chen, T. P. Van Doren, T.P., J. L. Drewniak, and R. E. DuBroff, “Power-bus decoupling with embedded capacitance in printed circuit board design”, *IEEE Transactions on Electromagnetic Compatibility*, vol. 45, no. 1, pp. 22-30, Feb. 2003.

[9] I. Novak, “Reducing simultaneous switching noise and EMI on ground/power planes by dissipative edge termination,” *IEEE Transactions on Advanced Packaging,* vol. 22, no. 3, pp. 274-283, Aug. 1999.

[10] T. M. Zeeff and T.H. Hubing, “Reducing power bus impedance at resonance with lossy components,” *IEEE Transactions on Advanced Packaging,* vol. 25, no. 2, pp. 301 -310, May 2002.

[11] X. Ye, D. M. Hockanson, M. Li, Y. Ren, W. Cui, J. L. Drewniak and R. E. DuBroff, “EMI mitigation with multilayer power bus stacks and via stitching of reference planes,” *IEEE Transactions on Electromagnetic Compatibility,* vol. 43, no. 4, pp. 538-548, Nov. 2001.

[12] D. F. Sievenpiper, L. Zhang, R. F. J. Broag, N. G. Alexopolous, and E. Yablonovitch, “High-impedance electromagnetic surfaces with a forbidden

frequency band," *IEEE Trans. Microw. Theory Tech.*, vol. 47, no.11, pp. 2059–2073, Nov. 1999.

[13] D. F. Sievenpiper, "High-impedance electromagnetic surfaces," Ph.D. dissertation, Dept. Elect. Eng, Univ. California at Los Angeles, Los Angeles, CA, 1999.

[14] R. Abhari and G. V. Eleftheriades, "Metallo-dielectric electromagnetic bandgap structures for suppression and isolation of the parallel-plate noise in high-speed circuits," *IEEE Trans. Microw. Theory Tech.*, vol. 51, no. 6, pp. 1629–1639, Jun. 2003.

[15] T. Kamgaing and O. M. Ramahi, "A novel power plane with integrated simultaneous switching noise mitigation capability using high impedance surface," *IEEE Microwave and Wireless Components Letters,* vol. 13, no. 1, pp. 21-23, Jan. 2003.

[16] S. Shahparnia and O. M. Ramahi**,** "Miniaturized Electromagnetic Bandgap Structures for Broadband Switching Noise Suppression in PCBs," *Electronics Letters*, vol. 41, no. 9, pp. 519-520, Apr. 2005.

[17] T. Kamgaing and O. M. Ramahi, "Inductance-enhanced high-impedance surfaces for broad-band simultaneous switching noise mitigation in power planes," in *IEEE MTT-S Int. Microwave Symp. Dig.*, Philadephia, PA, Jun. 8-13, 2003, pp. 2165–2168.

[18] S. D Rogers, “Electromagnetic-Bandgap Layers for Broad-Band Suppression of TEM Modes in Power Planes”, *IEEE Trans. Microw. Theory Tech.*, vol. 53, no. 8, pp. 2495–2505, Aug. 2005.

[19] S. Shahparnia, B. Mohajer-Iravani, and O. M. Ramahi, “Electromagnetic noise mitigation in high-speed printed circuit boards and packaging using electromagnetic bandgap structures,” in *Proc. 54th Electronic Components and Technology Conf.*, , Las Vegas, NV, Jun.1–4, 2004, pp. 1831–1836.

[20] M. Rahman and M. A. Stuchly, “Modeling and application of 2D photonic band gap structures”, *Aerospace Conference, 2001 IEEE Proceedings*, vol. 2, Montana, Mar. 10-17, 2001, pp. 893-898.

[21] T. L. Wu, C. C. Yang, Y. H. Lin, et al. “A novel power plane with super wideband elimination of ground bounce noise on high speed circuits” *IEEE Microwave and Wireless Components Letters,* vol. 15 no. 3, pp. 174-176, Mar. 2005.

[22] J. Choi, V. Govind, M. Swaminathan, L. Wan, and R. Doraiswami, “Isolation in mixed-signal systems using a novel electromagnetic bandgap (EBG) structure,” in *IEEE 13th Topical Meeting Electr. Perform. Electron. Packag.,* Portland, OR, Oct. 25-27, 2004, pp. 199 – 202.

[23] T. L. Wu, Y. H. Lin, and S. T. Chen, “A novel power planes with low radiation and broadband suppression of ground bounce noise using photonic bandgap

structures," *IEEE Microwave and Wireless Components Letters,* vol. 14, no. 7, pp. 337–339, Jul. 2004.

[24] N. Shino and Z. Popovic, "Radiation from ground-plane photonic bandgap microstrip waveguide," in *IEEE MTT-S Int. Microw. Symp. Dig*, Seattle, WA, Jun. 2-7, 2002, pp. 1079–1082.

[25] J. Lee, H. Kim, J. Kim, "High dielectric constant thin film EBG power/ground network for broad-band suppression of SSN and radiated emissions," *IEEE Microwave and Wireless Components Letters,* vol. 15 no.8, pp. 505-507, Aug. 2005.

[26] Y. Ko, K. Ito, J. Kudo, and T. Sudo, "Electromagnetic radiation properties of a printed circuit board with a slot in the ground plane," in *Proc. Int. Symp. Electromagnetic Compatibility,* Tokyo, Japan, May 17-21, 1999, pp. 576 -579.

[27] Paul, Clayton, *Introduction to Electromagnetic Compatibility*. Hoboken, NJ: Wiley-Interscience, 1992.

[28] J. C. W. Ho, Q. Zhu, and R. Abhari, "Modeling of transmission lines with textured ground planes and investigation of data transmission by generating eye diagrams," in *IEEE 13th Topical Meeting Electr. Perform. Electron. Packag.,* Portland, OR, Oct. 25-27, 2004, pp. 199 – 202.

[29] G. A. Katopis, "Delta I-noise specification for a high-performance computing machine", *IEEE proceedings*, vol. 73, no. 9, pp. 1405, Sep. 1985.

[30] S. Van den Berghe, F. Olyslager, D. De Zutter, J. De Moerloose and W. Temmerman, “Study of the ground bounce caused by power planes resonance”, *IEEE Transactions on Electromagnetic Compatibility*, vol. 40, no. 2, pp. 111-119, May 1998.

[31] D. K. Cheng, *Field and Wave Electromagnetics*, Prentice Hall, Second Edition, 1989.

[32] D. Pozar, .*Microwave Engineering*,. 2nd Edition, John Wiley & Sons, 1998.

[33] S. J. Mason and H. J. Zimmerman, *Electronic Circuits, Signals, and Systems*, Wiley, New York, 1960.

[34] A. B. Carlson, *Communication Systems*, McGraw-Hill, New York, 1968.

[35] D. M. Pozar, “Analysis of an infinite array of rectangular microstrip patches with idealized probe patches”*, IEEE Transactions on Antenna and Propagation*, vol. 32, no. 10, pp. 1101-1107, Oct. 1984.

[36] P. B. Johns, “The solution of inhomogeneous waveguide problems using a transmission-line matrix,” *IEEE Trans. Microwave Theory and Tech*, vol. 22, no. 3, pp.209-215, Mar 1974.

[37] O. M. Ramahi, V. Subramanian and B. Archambeault, “A simple and efficient finite-difference frequency-domain (FDFD) algorithm for analysis of switching noise in printed circuit boards and packages,” *IEEE Transactions on Advanced Packaging,* vol. 26, no. 2, pp. 191-198, May 2003.

[38] M. Aubourg, J.P. Villotte, F. Godon, and Y.Garault, "Finite element analysis of lossy waveguides—application to microstrip lines on semiconductor substrate," *IEEE Trans. Microwave Theory Tech.*, vol. MTT-31, pp. 326-331, Apr. 1983.

[39] High frequency structure simulator (HFSS), Ansoft Co., Pittsburgh, PA.

[40] M. Rahman and M. A. Stuchly, "Transmission line-periodic circuit representation of planar microwave photonic bandgap structures," *Microwave and Optical Technology Letters,* vol. 30, no. 1, pp. 15-19, Jul. 2001,

[41] S. Shahparnia, "Electromagnetic Bandgap Structures for Broadband Switching Noise Mitigation in High-Speed Packages", PhD Thesis, University of Maryland, 2005.

[42] G.. T. Lei, R. W. Techentin, P. R. Hayes, D. J. Schwab and B. K. Gilbert, "Wave model solution to the ground/power plane noise problem," *IEEE Transactions on Instrumentation and Measurement,* vol. 44, no. 2, pp. 300-303, Apr. 1995.

[43] S. Chun, M. Swaminathan, L. D. Smith, J. Srinivasan, Z. Jin and M. K. Iyer, "Modeling of simultaneous switching noise in high speed systems," *IEEE Transactions on Advanced Packaging,* vol. 24, no. 2, pp. 132-142, May 2001.

[44] E. F. Kuester, "Accurate approximation for a function appearing in the analysis of microstrip," *IEEE Transactions on Microwave Theory and Technique*, vol. 32, no. 1, pp. 131-133, Jan. 1984.

[45] H. M. Greenhouse, "Design of planar rectangular microelectronics inductors" *IEEE Transactions on Parts, Hybrids, and Packaging*, Vol. PHP-10, No. 2, June 1974.

[46] C. Chicone, *Ordinary Differential Equations with Applications,* Springer-Verlag, New York, 1999.

[47] L. Brillouin, *Wave Propagation in Periodic Structures: Electric Filters and Crystal Lattices*. Mineola, NY: Dover, 1953.

[48] T. A. Birks, P. J. Roberts, P. S. J. Russell, D. M. Atkin, and T. J. Shepherd, "Full 2-D photonic bandgaps in silica/air structures," *Electron. Lett.*, vol. 31, pp. 1941–1943, Oct. 1995.

[49] J. S. Foresi, P. R. Villeneuve, J. Ferrera, E. R. Thoen, G. Steinmeyer, S. Fan, J. D. Joannopoulos, L. C. Kimerling, H. I. Smith, and E. P. Ippen, "Phonotic-bandgap mocrocavities in optical waveguides," *Nature*, vol. 390, pp. 143–145, 1997.

[50] M. Inoue and K. Arai, "Magneto-optical properties of one-dimensional photonic crystals composed of magnetic and dielectric layers," *J. Appl. Phys.*, vol. 83, no. 11, pp. 6768–6770, Jun. 1998.

[51] R. E. Collin, *Foundations for Microwave Engineering*, Second Edition, John Wiley and Sons, Inc. 1992.

[52] T. H. Hubing, "Printed circuit board EMI source mechanisms," in *Proc. IEEE Int. Symp. Electromagnetic Compatibility*, Boston, MA, Aug. 2003, pp. 1–3.

[53] M. Leone, "The radiation of a rectangular power bus structure at multiple cavity-mode resonances," *IEEE Transactions on Electromagnetic Compatibility,* vol. 45, no. 3, pp. 486–492, Aug. 2003.

[54] N. Na, J. Choi, S. Chun, M. Swaminathan, and J. Srinivasan, “Modeling and transient simulation of planes in electronic packages,” *IEEE Trans. Advanced Packaging*, vol. 23, no. 3, pp. 340–352, Aug. 2000.

[55] G. T. Lei, R. W. Techentin, and B. K. Gilbert, “High-frequency characterization of power/ground-plane structures,” *IEEE Trans. Microwave Theory Tech.*, vol. 47, pp. 562–569, May 1999.

[56] R. P. Mays, "A Summary of the Transmitting and Receiving Properties of Antennas," *IEEE Antennas and Propagation Magazine*, vol. 42, no. 3, June 2000.

[57] C. A. Balanis, *Antenna Theory Analysis and Design*, Second Edition, John Wiley & Sons, Inc., New York, 1997.

[58] J. Buchanan, *Signal and Power Integrity in Digital Systems: TTL, CMOS, and BiCMOS,* McGraw Hill, New York, 1995.

[59] H. W. Johnson, and M Graham, *High-Speed Digital Design, a Handbook of Black Magic*, PTR Prentice Hall, Englewood Cliffs, NJ, 1993.

[60] H. Shi, F. Sha, J.L. Drewniak, T.P. Van Doren, and J.H. Hubing, “An Experimental Procedure for Characterizing Interconnects to the DC Power Bus on a Multilayer Printed Circuit Board,” *IEEE Transactions on Electromagnetic Compatibility,* vol. 39, pp. 279-285, Nov. 1997.

[61] J. Rainal, “Computing inductive noise of CMOS drivers,” *IEEE Transactions on Components, Packaging, Manufacturing Technology–Part B*, vol. 19, pp. 789–802, Nov. 1996

[62] L. D. Smith, R. E. Anderson, D.W. Forehand, T. J. Pelc, T Roy, “Power Distribution System Design Methodology and Capacitor Selection for Modern CMOS Technology,” *IEEE. Trans. on Advanced Packaging,* vol. 22, no. 3, pp. 284-291, Aug. 1999.